WEAR RATE AND MECHANISM MAPS FOR STAINLESS STEEL AT HIGH TEMPERATURE

A Dissertation
Presented to
The Academic Faculty

by

Chuchu Zhang

In Partial Fulfillment
of the Requirements for the Degree
Doctor of Philosophy in the
School of Materials Science and Engineering

Georgia Institute of Technology
December 2020

COPYRIGHT © 2020 BY CHUCHU ZHANG

WEAR RATE AND MECHANISM MAPS FOR STAINLESS STEEL AT HIGH TEMPERATURE

Approved by:

Dr. Richard W. Neu, Advisor
School of Mechanical Engineering
School of Materials Science and Engineering
Georgia Institute of Technology

Dr. Jeffrey Streator
School of Mechanical Engineering
Georgia Institute of Technology

Dr. Preet Singh
School of Materials Science and Engineering
Georgia Institute of Technology

Dr. Shreyes Melkote
School of Mechanical Engineering
Georgia Institute of Technology

Dr. Joshua Kacher
School of Materials Science and Engineering
Georgia Institute of Technology

Date Approved: [Nov 20, 2020]

To my family

ACKNOWLEDGEMENTS

Graduate school is challenging, and Covid-19 has made it worse. I'm sincerely grateful to be helped and supported by many great people during my PhD study in Tech, which are essential to the completion of the journey.

Firstly, I would like to thank my advisor: Dr. Richard W Neu for giving me the opportunity to join MPRL group as well as all the guidance and support he provided to me over the past four years. His warm and consistent encouragement has enabled me to achieve more than I thought I possibly could, and the freedom he gave me in exploring my interested research topics has shaped me to a capable researcher and problem-solver.

I'd like to also thank my committee members: Dr. Preet Singh, Dr. Jefferey Streator, Dr. Shreyes Melkote, and Dr. Joshua Kacher for their time and valuable feedback on my proposal and dissertation. I'm honored to have all of you in my committee!

It has been a been a delightful experience work with many brilliant colleagues in MPRL: Dr. Ashley Goulding, Dr. Kyle Brindley, Dr. Ernesto Estrada, Dr. Morris Satin, Dr. Sanam Gorgan-Nejad, Anirudh Bhat, Jonathan Leung, Benjamin Seitz, Shiyu Suzuki and Zack Towner. Thank you all for exchanging research reflections, graduate school life consulting as well as career advices! I'm also honored to be bonded with the tribology community in ME department: I would like to thank Dr. Michael Varenberg for the insightful discussions about tribology topics and the valuable opportunity to teach ME4853 labs together. I would like to thank Dr. Huaidong Yang, Dr. Vinh Nguyen, Dr. Jaekang Kim, Dr. Yingdan Wu,

Ye Qi, and Yuan Gao for the research discussions as well as all the fun time in hot-pot parties. Your presence makes me feel that I'm not fighting alone in the field of tribology.

I would like to thank all the faculties and technicians that have supported my research projects. In particular, Dr. James Collins, JD Huggins from MPRL and Kyle French from ME Electronic Lab for equipment maintenance and troubleshooting, Nathan Mauldin and Scott Elliot from Montgomery Machining Mall of GT for machining numerous samples for my projects, Eric Woods (IEN), Yolande Berta (MSE) and professor Faisal Alamgir (MSE) for assistance and helpful discussion in material characterization. I would like to thank the administrative staffs of MSE and ME department: Dracy Blackwell, Teresa Nelson and Glenda Johnson for being there for me for every step of my graduate study.

I would like to thank all the professors that I have taken courses with in GT. Special thanks go to all the faculties that I have learnt Japanese from scratch in GT with: Kikuchi sensei, Suzuki sensei, Matsushima sensei and Weiss sensei. Language learning has been very fun and rewarding that helps me to overcome tresses. Thank you all for bringing me in the track of Japanese learning, and inspiring me to think and express from a new perspective.

I would like to thank Dr. Jeff Lane, Dr. Paul Prichard and Dr. Zhuqing Wang from Kennametal additive manufacturing group for offering me the internship opportunity and helping me to succeed in the project. Looking back at my graduate school life, this experience not only calibrates my imagination of industrial R&D, but also enables my rapid growth with enhanced confidence.

I would like to thank all my friends, both in US and China, who have transferred their love and positive energy to me during my PhD and COVID pandemic. The joy and honor of my accomplishment also belong to all of you.

Lastly, I would like to express my sincere gratitude to my family. I wouldn't have gone this far without the continuous support and encouragement from my beloved parents and grandparents. I'm grateful to be born and raised up in this caring and loving family. I would like to thank my husband and best friend Dr. Jing Dong for his unconditional love and belief in me, and being my closest companion to share every moment with. I'm looking forward to continuing the life journey with you and holding hands.

TABLE OF CONTENTS

ACKNOWLEDGEMENTS iv

LIST OF TABLES ix

LIST OF FIGURES x

LIST OF SYMBOLS AND ABBREVIATIONS xvi

SUMMARY xviii

CHAPTER 1. Introduction 1
1.1 Motivation 1
1.2 Thesis statement and thesis scope 5
1.3 Significant Contributions 6

CHAPTER 2. Literature review 8
2.1 Classification of wear mechanisms 8
2.2 Temperature-dependent severe-to-mild wear transition 10
2.3 Role of frequency in fretting wear 19
2.4 Wear maps 25
2.5 Austenitic stainless steel 29
2.6 Objective of the dissertation 31

CHAPTER 3. Material and experimental methods 33
3.1 High temperature fretting and reciprocating sliding test system 33
3.2 Material and Specimen 35
3.3 Calculation of Coefficient of friction 41
3.4 Wear characterizations 46

CHAPTER 4. Construction of wear mechanism maps 50
4.1 Design of Experiment 50
4.2 Univariable temperature-baseline test 53
4.3 Quantification of E-COF evolution with sigmoid fitting 59
4.4 Univariable frequency-baseline test 63
4.5 Temperature-frequency coupling effect in wear performance 69
4.6 N_{GL} model correlations 79
4.7 Strategy of constructing and utilizing a wear mechanism map 84
4.8 Conclusions 87

CHAPTER 5. Characterization of glaze layer using computer vision algorithms 89
5.1 Introduction 89
5.2 Background in computer vision 92
5.2.1 Homography transition 92
5.2.2 HSV colour space and its separation 94
5.3 Methodology 94

5.3.1 Dataset preparation 94
5.3.2 Image alignment workflow 97
5.4 Quantitative H-V criterion for glaze layer identification 100
5.4.1 Glaze layer identification with H-V criterion 100
5.4.2 Application and evaluation of H-V criterion 102
5.5 Distribution of glaze layer and its temperature dependence 106
5.5.1 Height distribution of glaze layer at different temperature 106
5.5.2 Temperature dependence on the coverage of glaze layer 110
5.6 Evaluation of wear characterization tools for glaze layer identification 114
5.7 Conclusions 118

CHAPTER 6. General conclusions and recommendations 121

REFERENCES 124

LIST OF TABLES

Table 3-1	Chemical composition(wt%) of 310S raw material	36
Table 3-2	Room temperature mechanical properties of annealed 310S (extracted from supplier documentation)	37
Table 4-1	Point EDX results showing chemical composition in weight percentage of spot 1, 2 and 3 and static oxide (oxide formed outside of the wear scar).	58
Table 4-2	Comparison of material and test conditions between Jin and Shipway [57] and current work	66
Table 4-3	Estimated fretting induced temperature rise at center of contact and at thermocouple location for frequency-baseline tests, comparing to the temperature rise measured by thermocouple.	68
Table 5-1	Point EDX analysis on major element in glaze layer, shiny spot and reference area, all results are in wt%.	105
Table 5-2	Mean value and hypothesis test results for height distribution of glaze and non-glaze layer at each temperature	109
Table 5-3	Summary of existing tools that could be used to characterize glaze layer, and the outcome of glaze layer and non-glaze layer feature under those characterization. Possible type II error source(s) for each tool column are highlighted.	117

LIST OF FIGURES

Figure 1-1 Normalized wear performance of several material couples at different environmental temperature. 3

Figure 2-1 Schematic image for the four wear mechanisms: a) Abrasive wear in cutting mode of ductile bulk surface; b) Adhesive wear by adhesive shear and transfer, c) Fatigue wear by subsurface crack initiation and propagation; d) Corrosive wear by shear fracture of ductile tribofilm. The arrow shows sliding direction.[15] 10

Figure 2-2 Worn surface SEM of Ni-based alloy at 250°C reciprocal sliding test : a) Zoom in image of wear surface after first 100 min, showing aggregated and as-compacted debris; b) apparent large compacted glaze layer and surrounded fine debris upon finish of the test. [20] 11

Figure 2-3 a) Example of severe-to-mild wear transition for wear volume loss and steady state coefficient of friction as a function of temperature. Tests were conducted with Co-Cr alloy on Alumina cross-cylinder tribo system (normal force P = 50N, sliding amplitude δ^*=± 20μm, frequency f=50Hz, cycle N = 200K). In this case no wear was detected on Alumina and the wear loss are only from Co-Cr counterpart. Typical temperature for domain I (100°C), II (250°C), and III (400°C) are cross-labeled in red; b) Comparison of the fretting scar morphology on Co-Cr (optical, SEM and EDX) at typical temperature for each domain [36] 13

Figure 2-4 Selected COF and volume loss as a function of ambient temperature reported in literature with their testing condition (normal force (P), displacement amplitude(Δ), frequency ($\boldsymbol{f}$) and total cycle(N). Data digitized from source: a)304 like-on-like line sliding [29]; b) low alloy like-on-like cylinder on flat fretting[30]; c) Ni-20Cr alloy like-on-like cylinder-on-flat reciprocating sliding[21]. Note how the characteristic temperature T1 and T2 and the wear behavior in domain I (T<T1) is different in each case and comparing to Figure 2-3. 15

Figure 2-5 A demonstration map of glaze layer formation when temperature varies based on $\boldsymbol{N_{GL}}$ model for Co-Cr/Alumina cross-cylinder tribo pairs. Map constructed with data shown in Fig 2.3 (P = 50N, f = 50Hz, δ* = ±20μm).[54] 18

Figure 2-6	Interaction diagram that links temperature and frequency with several main wear features to determine wear damage [35]	21
Figure 2-7	Temperature rise prediction for 304 like-on-like cylinder on flat fretting tests at 20Hz and 200Hz (P =450N, $\boldsymbol{\Delta = 50\mu m}$, μE = 0.6) a): Prediction of local surface temperature rise in contact after 100K fretting cycle as a function of distance from center; b)predicted origin (x = 0) temperature rise as a function of distance below the surface at 1000s for 200Hz test with inclusion of 5μm thick oxide layer with different thermal properties ; c-d) comparison of predicted temperature rise at the fixed origin with inclusion of a 5μm thick oxide layer with different thermal properties for 1000s.[57,68]	23
Figure 2-8	A combined Lim-Ashby wear map with base of wear transition between mild and severe wear[74], and color shad represent different wear mechanism (extracted from reference[72]). This wear map is for room temperature steel-on-steel pin-on-disk configuration. The gray shaded areas represent transition between mild & severe wear.	27
Figure 2-9	Temperature-sliding speed wear map of Nimonic 80A vs Stellite 6 (P = 7N, sliding distance = 5422m) with weight loss in contour and zones for major wear mechanisms are recolored. [33]	29
Figure 2-10	Composition and property linkage for 300 series austenitic stainless steel.[79]	30
Figure 3-1	a) Schematic diagram of DN55 testing rig and relative position between thermocouple and wear scar. b) A hysteresis loop generated with data recorded in HSD file, with δ*, Δ* and S geometrically defined in the loop.	34
Figure 3-2	Microstructure of 310S pin sample under microscope, etched by C13 reagent, 100X	36
Figure 3-3	Dimension design of a) flat tensile specimens; b) cylindrical tensile specimens. The dimensions came from ASTM E8-10 standard [93].	37
Figure 3-4	Effect of temperature on the a) tensile properties of 310S raw material, reference is data of annealed type 310 stainless steel from ref[92] and b)Young's modulus of 310S raw material and reference Young's modulus, shear modulus and Poisson's ratio of 310/310S stainless steel reported in [89–91]	38

Figure 3-5 a) Dimensions of pin (top) and plate (bottom) specimens; b) Notation for Hertzian line-contact calculations for line contact configuration with current sample dimensions. 39

Figure 3-6 a) Schematic of a hysteresis fretting loop with hook-like increase in tractional force during gross sliding, with $\boldsymbol{\delta^*, \Delta^*}$ **and S** geometrically defined in the loop; b) Comparison of fretting loops with grooves of different aspect ratio sharing the same Q along Q = **S**Δ line, the aspect ratio of the groove is defined as sub plot on upper left [95**]**; 42

Figure 3-7 Demonstration on numerical determination on GI_COF (tangential force determination for GI-COF in gold), max/min tangential force (in green), and sliding amplitude δ* (in purple). 44

Figure 3-8 Different COF calculation method using HSD data of a room temperature test. 45

Figure 3-9 a) Schematic of volume up ($\mathbf{V^{up}}$) and volume down ($\mathbf{V^{down}}$) to the reference (unworn surface) in dash. b) Example of surface profile processing with form removal on pin and plate. (Test condition: T = 100℃, $\boldsymbol{P = 150N, \Delta^* = 200\mu m, f = 10Hz}$) 48

Figure 4-1 Design of experiment generating wear mechanism map with hierarchical probing strategy: a) baseline tests; b) complete strategy. 52

Figure 4-2 a) Evolution of μ_E and net wear rate ($\dot{\boldsymbol{V}}$ net) with temperature using 310S/310S temperature-baseline results. $\dot{\boldsymbol{V}}$ net is plotted with inverse axes, b) Typical μ_E evolution with cycle plot for 250°C (N_{tot} = 66K cycles in blue N_{tot} = 100K cycles in red), 280°C and 300°C, the three temperature that falls in transition temperatures zone as labeled in a). 54

Figure 4-3 Volume up and down contributed by pin and plate for each temperature, results are averaged from 3 duplicates and their left/right channel 55

Figure 4-4 SEM of wear scars on plate sample from top view. (a) and (d): 250°C test with 66K cycle, where debris were compacted but not forming sufficient glaze layer; (b) and (e):250°C test with 100K cycle, where small island of glaze layer (in black) was formed, and the enlarged image (e) shows the sintered and flat feature of glaze layer and abrasive wear groove along the fretting direction; (c) and (f): 400°C test with 66K cycles, where large network of 56

glaze layer is formed, and the enlarged image (f) shows a large area of glaze layer with less abrasive grooves.

Figure 4-5 SEM picture of top view within wear scar on plate specimen of 700◦C test. Spot 1: glaze layer center, Spot 2: glaze layer edge, spot 3: Outside of glaze layer 57

Figure 4-6 Cross-section view of plate sample after 600C 10Hz tests showing the glaze layer structure, the reciprocating direction is noted by double headed arrows: a) OM, BS-SEM and EDX element mapping of glaze cross-section, scale bar = 25μm; b) EDX line scan of major elements' distribution along the depth of wear scar 59

Figure 4-7 Schematic of sigmoid function and the fitting parameters' determination on the shape and location of the curve: (a): simplified sigmoid curve, (b) demonstration of sigmoid fitting with 250°C_100K test result and illustration of the tribological meaning of the fitting parameters 61

Figure 4-8 Influence of frequency of cycling at room temperature: a) $\boldsymbol{\mu_E}$ evaluation with cycle at each frequency, sub figure in a) shows the hysteresis loops near the end of the test. b)Frequency-E-COF-wear rate plot overlapped with temperature rise captured by the thermocouple 64

Figure 4-9 Fretting induced temperature rise as a function of frequency: a) Evolution of temperature measured at thermocouple location over the cycles of the test for each frequency. b) The temperature rise rate at each frequency and the second order polynomial fitting result. 66

Figure 4-10 NWR and steady-state E-COF of 310S/310S at various environmental temperature and frequency 71

Figure 4-11 a) Zygo height map of pin and plate after tested at 50Hz, 400°C; b) OM image of the area selected in white block of Zygo height map for pin and plate in a) 72

Figure 4-12 Steady-state E-COF map of 310S/310S cylinder-on-flat fretting system: a) complete map; b) map focused on the 200°C to 400°C temperature regime with $\overline{\boldsymbol{\mu}}_{\boldsymbol{E}} < 0.5$ and $\overline{\boldsymbol{\mu}}_{\boldsymbol{E}} > 0.7$ used to define the boundaries between A, B, C and D zone, respectively 73

Figure 4-13 a) Environmental temperature-dependence of NWR at various frequency; b) average thermocouple temperature dependence of NWR at various temperature. 74

Figure 4-14 Frequency-dependence of NWR at various environmental temperature. 76

Figure 4-15 Wear map of 310S/310S at cylinder-on-flat configuration: a) complete map; b) details of the map near the transition zone: 200°C-300°C that show different mode of synergic effect between environmental temperature and frequency 78

Figure 4-16 a) Correlation of the N_{GL} model using environmental temperature; b) Correlation of N_{GL} model considering temperature rise at the interface 81

Figure 4-17 Overlapping of severe-to-mild wear transition boundaries predicted by N_{GL} model with the obtained wear map 83

Figure 5-1 A pair of corridor floor image with different perspective from reference[105]: a) view perspective is about parallel to the floor tile; b) view perspective is perpendicular to the floor tile. The two images are related via homography transformation, and the four highlighted corners of a floor tile set can be used to compute the homography 93

Figure 5-2 Example of conducting HSV color space separation for a photograph of flowers: a) Original image; b) H channel; c) S channel; d) V channel. H channel are colored to better illustrate the color(S=V=1). 94

Figure 5-3 Schematic of different lighting mode and their resulting OM image at the same view of wear scar after 500°C test: a) with ring lighting (RL) mode, 60% intensity; b) with coaxial illumination (CXI) mode, 20% intensity; c) with combined CXI (20% intensity) and RL lighting mode(10% intensity). The three OM images share the same scale bar 96

Figure 5-4 Outcome images of image alignment workflow demonstrated with images of 280C plate: (a) Original height map; (b) Original OM; (c) magnified and recolored marker area in height map; d) magnified marker area in OM; (e) aligned OM image; (f) final height map; (g) final aligned OM . (a) and (e)-(g) share the same scale bar. The region selected by white frame in (g) is used for validation of glaze layer identification criteria in 5.4.2 99

Figure 5-5 Glaze layer identification workflow for an OM image acquired from a plate that experienced fretting at 280°C. All images share the same scale bar 102

Figure 5-6 Demonstration of identifying glaze layer with OM image with reference of SEM, OM is pre-aligned to SE SEM: a) OM image; 104

b) Value channel of OM; c) Hue channel of OM; d) BSE SEM image; f) SE SEM image; g) SE SEM overlaid with glaze layer mask(shadowed in red) identified from OM. All images share the same scale bar.

Figure 5-7 Hue range (Lower end =H_{min}, upper end = H_{max}) and V_{min} parameter used to identify glaze layer at each testing temperature, overlapped with average Hue value of glaze layer area(H_{avg}) 106

Figure 5-8 Histogram of height for glaze layer and non-glaze layer area and their fitted Gaussian distribution curve at 280°C, 300°C, 500°C and 700°C. The overlayed square in height map and OM represented the sampling location of the data subsets for each sample. Typical build-ups at the edge of wear scar are circled in dashed line. All OM images and height maps share the same scale bar. 107

Figure 5-9 Effect of temperature on net wear rate wear, average $\overline{\boldsymbol{\mu}}_{\boldsymbol{E}}$ and glaze layer coverage on pin and plate 111

LIST OF SYMBOLS AND ABBREVIATIONS

Δ^*	Displacement amplitude(commanded amplitude)
Δ	Displacement
δ^*	Sliding amplitude
f	Frequency
Q	Tangential force
P	Normal Force
E_d	Dissipated energy
N	Cycle count
N_{GL}	Critical cycle for glaze layer formation
HSD	High-speed Data
LSD	Low-speed Data
COF, μ	Coefficient of friction
E-COF, μ_E	Energetic coefficient of friction
$\bar{\mu}_E$	Steady state energetic coefficient of friction
GI-CoF	Geometric coefficient of friction
b	Semi Hertzian contact length
l	Line contact length
P'	Normal force per unit length
p_0	Maximum Hertz pressure
R^*	Equivalent radius
E	Youngs modulus
E^*	Equivalent elastic modulus

ν	Poisson's ratio
τ_1	Maximum principal shear stress
τ_Y	Yield shear strength
σ_Y	Yield normal strength
V^{sum}	Total volume transferred between two bodies
V^{net}	Net volume loss of the two bodies
$V^{up}, V_{pin}^{up}, V_{plate}^{up}$	Volume of build-up material for all, pin, or plate
$V^{down}, V_{pin}^{down}, V_{plate}^{down}$	Volume of material removed or transferred for all, pin, or plate
$NWR, \dot{V}^{net}$	Net wear rate
OM	Optical microscope
SEM	Scanning electronic microscope
BSE	Back-scattered electrons
SE	Secondary electrons
EDX	Energy-dispersive X-ray spectroscopy
H	Hue channel in HSV color space
S	Saturation channel after HSV color space
V	Value channel in HSV color space
H_t	Homography transformation matrix
H_{max}, H_{min}	Maximum and minimum H value in H-V criterion
V_{min}	Minimum V Value in H-V criterion
C_p ,C_r	Projective(2D) and real(3D) glaze layer coverage
n_{glaze}, $n_{non\text{-}glaze}$	Number of pixels that are labeled as glaze layer and non-glaze layer
n_{tot}	Total number of pixels in selected area
$n_{glaze\_c}, n_{non-glaze\_c}$	Number of glaze layer and non-glaze layer pixels that was in contact

SUMMARY

Contacting interfaces moving in a back and forth way relative to each other at high temperature is found in mechanical systems like internal combustion engine, aerospace propulsion system, energy generation system and metalworking equipment. The working temperature for components in such mechanical systems, for example, pivot-vanes/ring in variable geometry turbocharger (VGT, also called variable-nozzle turbine, VNT) for diesel engines can vary from ambient temperature to 700℃, and even higher for gasoline engine. Materials selection for low friction, low wear in high temperature applications is a complex problem because of the many influence factors and coupling effects especially when friction and wear control methods like lubricating cannot be used.

It was found that a compacted and sintered wear protective layer, namely "glaze layer" can be formed in many Co, Ni and Fe alloys under certain circumstances, and it is possible to take advantage of glaze layer formation to reduce friction and wear at high temperature. The dissertation is aimed for better understanding of glaze layer and its role in severe-to-mild wear transition, and utilize this knowledge to push forward development of practical methodologies to build a robust high temperature wear map that benefits high-temperature tribo-pair design. 310S austenitic stainless steel is chosen as a sample system to generate temperature-frequency wear mechanism map. This map covers considerably large temperature and frequency in its working condition than has previous been considered. It has been found that the environmental temperature plays the overall dominant role in determination of the wear mechanism, although in the transition zone, a coupling effect between temperature and frequency has been observed. The experimental data was also

used to validate the applicability of a newly proposed critical cycle (N_{GL}) model for glaze layer formation.

In addition, we propose a novel way to understand the role of glaze layer using computer vision algorithms. Two workflows, one for quantitative glaze layer identification and the other for image alignment, have been developed. For glaze layer identification, we used computer vision concepts that considers the color and reflectiveness of glaze layer under optical microscope (OM). For image alignment, we developed a strategy to conduct pixel-to-pixel alignment of images acquired by multiple techniques (e.g., OM, scanning electron microscopy, 3D optical profilers) with sub-pixel error. As such, the correlation between the height map and locations of the glaze layer within the wear scar can be readily determined. The proposed methodology is applied to analysis the worn surface of 310S after high temperature fretting test, and the glaze layer is found to always occupy relatively high locations within wear scar. With temperature rise, the projected coverage of glaze layer follows the same increasing trend with three distinguishable stages, and the threshold temperature of the three stages matched with severe-to-mild wear transition. These results provide evidence that severe-to-mild wear transition resulted from spreading of glaze layer coverage, and glaze layer may reduce friction and wear by reducing real contact area.

CHAPTER 1. INTRODUCTION

1.1 Motivation

Contacting interfaces moving in a back and forth way relative to each other in mechanical systems operating at high temperature are challenging to design because the friction and wear mechanisms depend on several parameters[1]. Besides the two material couples and their elemental composition, other parameters include temperature, amplitude and frequency of the sliding displacement, normal pressure, contact configuration, gaseous environment (e.g., oxygen partial pressure), number of cycles, and the path dependence of the cycling can also play a role[2]. For example, the reactivity of the interfaces increases with temperature resulting in formation of oxides and other compounds, depending on the gaseous environment, that change the behavior of the surfaces. The normal force and frequency of sliding amplitude influences the rate of these changes. In addition, the mechanical strength of the material decreases with increasing temperature lowering the threshold for inelastic deformation in the surface layers. These changes in properties are coupled with an increased propensity for asperities of the interface to temporarily weld (i.e., friction welding) and then break from plastic shear deformation. It is necessary to understand which mechanism will likely be operating under a set of conditions to correctly predict the behavior of the interface when designing it.

These interfaces are found in internal combustion engines, aerospace propulsion system, energy generation systems, metalworking equipment, as well as many other mechanical machineries used in manufacturing processes[3–5]. Examples of components include inlet valve and seat insert, heat exchange tubes and their supports, turbine blades in their fitting

to the discs, and pivot-vanes/ring in variable geometry turbocharger (VGT, also called variable-nozzle turbine, VNT). For pivot-vanes/ring system specifically, because it is a moving part exposed to the exhaust gas flow, its working temperature for diesel engines varies from ambient temperatures (initial start of vehicle) to 200°C (no load, coasting) to 700°C (100% load – high RPM)[6], and even higher for gasoline engines. In such high temperature environment, traditional friction and wear control methods used at low temperature, such as lubricating, is often inapplicable due to degradation or difficulties in replenishment. Therefore, it is critical to understand the high temperature performance of the contact interface in unlubricated condition, referred to as dry sliding.

Figure 1-1 presents the normalized wear performance data for various metallic material couples that we collected for industrial sponsors for material screening purpose. All material candidates presented were tested at two temperatures: a moderate temperature(200-400°C) and a high temperature (600-800°C). The choice of the two temperature were the same and pre-defined, and the rest of the testing parameters were kept the same. The top candidates that show low friction low wear in the screening will be further examined in component tests. Such procedure is a normal practice for material selection in industry. However, the top ranked material candidate in the material screening database does not always perform well in component tests, suggesting that the two pre-defined testing temperatures may not be representative for wear performance at the working condition for all materials, and the results collected may not be sufficient enough to make good material selection decisions. Without fundamental understanding in wear mechanisms at elevated temperature, the knowledge learnt through collecting material screening database will be case specific and poorly transferable.

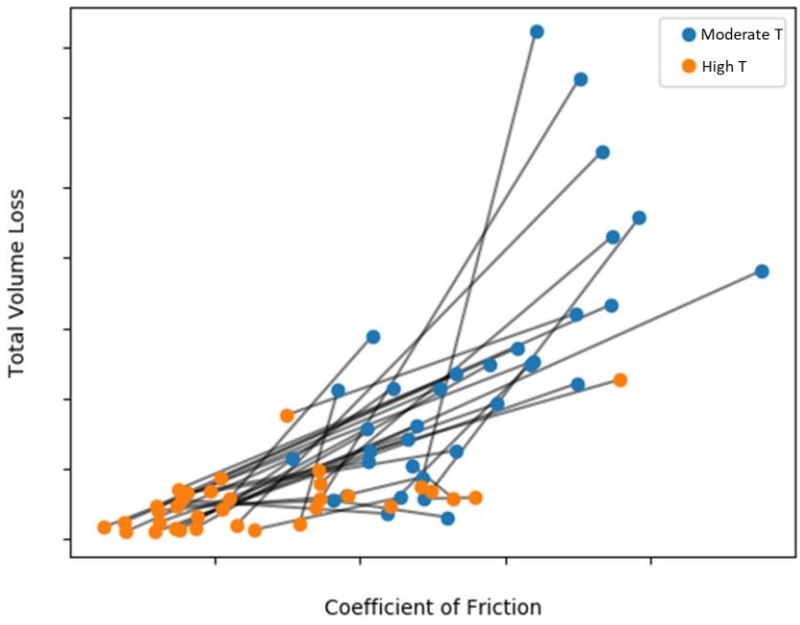

Figure 1-1 Normalized wear performance of several material couples at different environmental temperature. The testing results of the same material couple are connected by line.

Material selection is severely restricted to fulfill the complete performance requirements such as low friction, oxidation resistance for long term use, creep resistance and high strength to maintain shape, while maintaining reasonable cost. Materials that readily form passivation layers when exposed to oxygen, e.g., stainless steels and aluminum alloys, are a form of seal-healing materials. However, under contacting loads, it is not always clear how these layers behave since the layers may either degrade or become more robust (i.e., thicker). It is possible to take advantage of the oxidation process occurring at high temperature under some material combinations and environmental conditions where a smooth, compacted wear-resistant layer, termed ‘glaze layer,’ can be formed. A distinct severe-to-mild wear transition with increasing temperature is observed in many Co, Ni,

and Fe-based alloy. The glaze layer formation at contact interface turns out to be the major reason for this wear mode transition.

Wear mechanism maps are the one of the best approaches to visualize and understand the complexities of the coupling effects among all of these parameters. The functional relationships with physical parameters representing the boundaries between mechanisms can be used to determine how different material couples, test conditions, and contact configurations can be unified and compared. A series of wear mechanism maps provide a multi-dimensional graphical presentation of wear data showing where wear mechanisms are operating to help support engineering of these moving interfaces in mechanical systems.

This work focuses on interfaces under low amplitude back and forth motion. If the amplitude is sufficiently large that contact area at two extremes of the cycles do not overlap, it's called "reciprocating sliding". Otherwise, if there is overlap in the contact area, the term "fretting" is used[7]. The study is carried out with a unique high temperature fretting and reciprocating sliding test system (DN55) with unlubricated like-on-like cylinder on flat configuration. The work will explore the behavior of austenitic stainless steels which are commonly selected for high temperature applications. In particular, grade 310/ 310S, designed for high temperature applications due to its greater amounts of Cr and Ni (25 and 20 wt. %, respectively) than other austenitic stainless steels is chosen to be the major material system in this work.

Austenitic stainless steels are a widely used metallic material group for its high strength, ductility and excellent corrosion resistance. Grades like 309, 310/310s, and 314 which are

rich in chromium are typically selected for high temperature applications. They are relative low cost compared to special alloys containing even more Ni, Cr or Co, and the possibility of recycle make it preferable in many industrial applications under severe work conditions, such as rotor blades, shafts and nozzles in internal combustion engines. Of these grades, Type 310/310S is the most commonly used and therefore is a great candidate for clearly establishing fretting wear maps.

This dissertation is aimed for better understanding on kinetics of glaze layer formation and retention, and shed light on practical methodologies for the materials selection and contact surface design for unlubricated high temperature fretting and reciprocating sliding contacts with the help of wear mechanism map.

1.2 Thesis statement and thesis scope

The research outcome of this thesis is to support the following thesis statement:

Improved understanding of glaze layer and its role in severe-to-mild wear transition is a key contributor towards an engineering methodology of building a robust high temperature wear map that benefits high-temperature tribo-pair design.

The thesis scope is as follows:

Chapter 2 presents a literature review to describe the current understanding on high temperature wear mechanisms and the severe-to-mild wear transition that can occur at higher temperatures.

Chapter 3 gives introduction of the experimental set-up as well as materials used in this work.

Chapter 4 presents the best practice towards generating a temperature-frequency wear mechanism map for 310S stainless steel with available experimental resources.

Chapter 6 presents an improved understanding of glaze layer properties utilizing computer vision concepts. A novel quantitative and robust glaze layer identification criterion has been developed and tested, and pipelines has been developed to align multi-spectrum information that reveals the preferable location of glaze layer within wear scar.

Chapter 7 concludes the work by summarizing all the findings from the thesis and suggested possible directions of future work for studying glaze layer and constructing wear mechanism maps.

1.3 Significant Contributions

This research provides a complete methodology for wear map generation, interpretation and improvement that can benefit material wear couple screening, selection, and design. A demonstration of applying this methodology to construct a temperature-frequency wear map for 310S/310S cylinder-on-flat fretting system is presented. Presently, a high temperature fretting wear map does not exist for this tribological couple. A high quality tribological data set with good repeatability has been collected to systematically study the effect of environmental temperature and frequency on the wear performance for 310S, and provide direct experimental evidence for the temperature-frequency coupling effect associated with a severe-to-mild wear transition.

A notable contribution of this work is developing quantitative descriptors that promote standardization and automation of wear and tribological data analysis. In this work, we proposed a quantitative glaze layer identification criterion that enables fast, accurate, and automatic glaze layer identification from an optical image. In addition, the evolution of the coefficient of friction (COF) is represented with a sigmoid function using four fitting parameters. Those efforts provide fundamental solutions to improve the efficiency and repeatability of wear data analysis that has been heavily been heavily qualitative in the past, and enhance the transferability between wear and friction databases.

Lastly, a novel, open-source workflow that fuses characterization results from multiple tools has been developed using computer vision concepts and algorithms. Together with the glaze layer identification criterion, this tool reveals new knowledge of the glaze layer regarding its preferable location within the wear scar. It is a powerful tool that enables multi-spectrum analysis without upgrading existing characterization tools, which is not only beneficial for the tribology community, but also is easily transferable to all other applications in academia and industry.

CHAPTER 2. LITERATURE REVIEW

2.1 Classification of wear mechanisms

The simplest way to classify wear is probably by the level of friction force and wear volume. **Severe wear** (high friction, high wear volume loss) and **Mild wear** (low friction, low wear volume loss) can be identified experimentally[8]. Intuitive and simple as it is, this classification of wear type doesn't tell much about the mechanism that leads to the level of friction and wear volume loss.

Considering the wear rate (material loss per sliding distance), coefficient of friction, worn surface morphology and the nature of wear debris, four general type of wear mechanism (schematic in Figure 2-1) can be identified as below[9]:

1) **Abrasive wear** – in which material is removed by hard asperities on the counterface (termed two-body abrasive), or hard particle, often large granular wear debris, on the contact interface (termed three-body abrasive). Large hardness difference and irregular shape of the asperities or particles accelerate the material removal rate. Abrasive wear can take place via plastic deformation and brittle fracture, and it is characterized by groove marks on the worn surface[10].

2) **Adhesive wear** – in which material is removed by broken of local welds or plucking of materials between contact surfaces. Material couples that have higher mutual solubility or compatibility (e.g., like materials) are more likely to undergo adhesive wear[11]. High temperature and high pressure promote local welding and thus is favorable for adhesive wear [12]. Adhesive wear is also more likely to take

place in inert environment since oxide layer or particles will interfere with local welding by separating the surfaces and increasing the energy bar required for welding.

3) **Fatigue wear or delamination wear** – in which damage is done by cyclic stressing. According to Suh's delamination theory [13], dislocations are rapidly built up in the surface and subsurface layers undergoing deformation and plastic flow during wearing process. While dislocations close to the surface are able to move and be released, the dislocations beneath wear surface/track are less movable and build up in highly deformed layers. This leads to subsurface cracks that run parallel to the surface. With the propagation of the cracks, the thin surface layer become unstable and is pulled off as plate-like wear debris.

4) Corrosive wear – in which corrosion product (rust or film) are assumed to form though a tribo-chemical reaction between the contact surface and corrosive surrounding media, such as air or acid gas. Depending on the nature of corrosion produce and the fretting condition, a cycle of "fresh surface exposure and corrosion — corrosion product removal" may occur. **Oxidational wear** falls in this category where the "corrosion product" is an oxide tribofilm or oxidized debris. Under some circumstances these oxidized third bodies (oxidized debris or broken pieced of tribofilm) may be retained at the contact interface and form a wear-resistant "**glaze layer**" that leads to a markedly reduced wear rate, but in some other circumstances the oxidized third body may act as abrasive particles and lead to severe wear[14]. The duo effect of oxidational wear will be discussed in the following chapters.

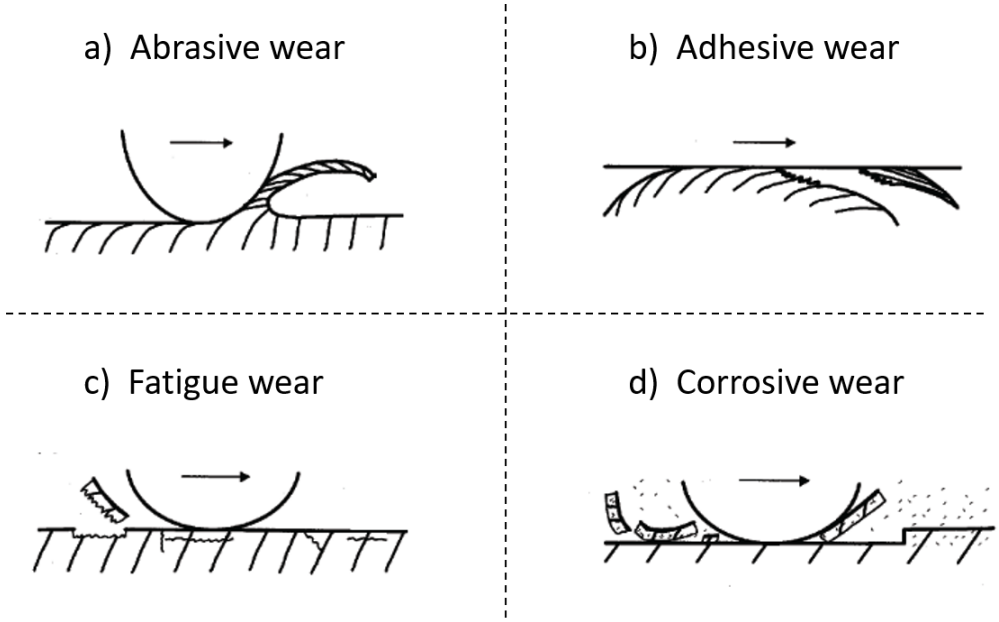

Figure 2-1 Schematic image for the four wear mechanisms: a) Abrasive wear in cutting mode of ductile bulk surface; b) Adhesive wear by adhesive shear and transfer, c) Fatigue wear by subsurface crack initiation and propagation; d) Corrosive wear by shear fracture of ductile tribofilm. The arrow shows sliding direction.[15]

Besides the four general types of wear mechanisms listed above, there are many other wear mechanisms proposed for even more extreme conditions. One such example is "melt wear", where a melting zone is formed due to high frictional heating or the extreme working environment, and spherical wear particles and unique surface morphology are expected. However, this type of wear is less common in general tribo-elements in most high temperature industrial applications and not considered as a dominant steady wear mode [16].

2.2 Temperature-dependent severe-to-mild wear transition

The surface alternation and wear between unlubricated metallic contact interfaces in fretting and reciprocating sliding has been studied and described with different theories. At

room temperature, a near-surface plastically deformed and recrystallized layer with ultrafine microstructure can be observed and was named as Tribologically Transformed Structure (TTS) , or sometimes called white etched area[17]. If the deformed structure is crushed into particles and mixed with counterparts debris, a Mechanically Mixed Layer (MML) is formed[18]. In general, MML is observed at lower temperatures. With increasing of ambient temperature, oxidation reaction of debris become more favorable in oxygen-containing atmosphere, and oxidational wear starts to dominant. Under certain fretting conditions, a wear-resistant third body called "glaze layer" can be formed[19], which leads to a severe-to-mild wear transition.

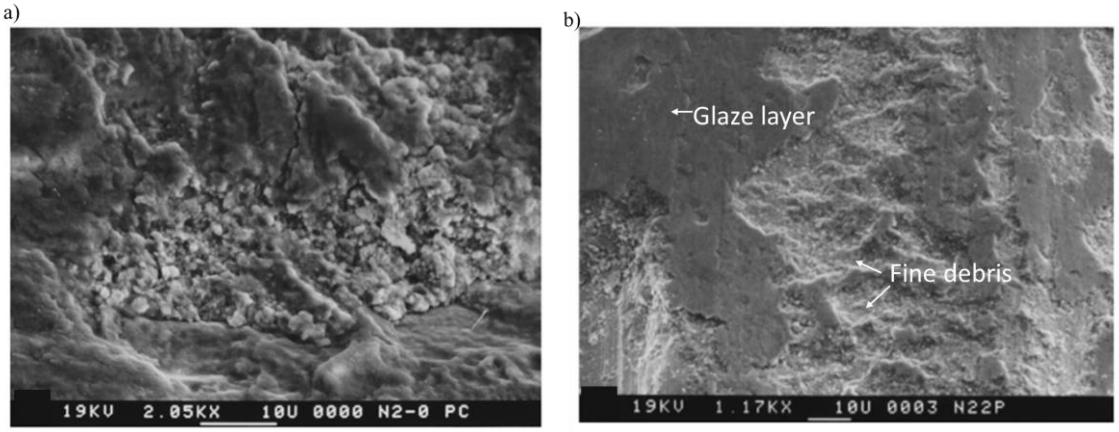

Figure 2-2 Worn surface SEM of Ni-based alloy at 250°C reciprocal sliding test : a) Zoom in image of wear surface after first 100 min, showing aggregated and as-compacted debris; b) apparent large compacted glaze layer and surrounded fine debris upon finish of the test. [20]

In 1970s, Stott et al. studied the effect of elevated ambient temperature on friction and wear behavior of some steels and Ni based alloys[21–24], where a severe-to-mild wear transition was observed with increasing temperature. The term "glaze layer" was then introduced to describe the smooth wear-protective tribolayer formed and adhered on contact area that

reduced friction and wear. A typical morphology of glaze layer can be found in Figure 2-2. Since glaze layer has superior mechanical properties compared to the bulk substrate (higher hardness[25], better ductility[26]), stabilized glaze layer can protect the substrate from further wear. Surface characterization before (Figure 2-2) and after (Figure 2-2) glaze layer formation indicated that glaze layer may result from compacted and sintered oxidized wear debris, and such process is also referred to as "tribo-sintering"[20,27].

The temperature dependent severe-to-mild wear mode changes are widely reported and discovered in many tribo-interfaces interfaces (metal-metal and metal-ceramic) and contact configurations, and the formation of 'glaze layer' is often shown to be the major reason of the friction and wear drop with increase of temperature [22,28–36]. One general pattern of this severe-to-meld wear transition can is shown in Figure 2-3, where the coefficient of friction (COF) and wear volume versus temperature (T) curve can be divided into three domains separated by two characteristic temperature: T1 (the temperature for maximum wear volume loss), and T2 (the temperature beyond which wear loss is negligible)[36].

Domain I (T< T1): Severe wear domain. This domain is characterized by high COF as well as wear volume loss. In this temperature range, the wear debris tends to be ejected from contact surface and leads to severe wear. While the glaze layer is not yet activated in this temperature range, the debris may be oxidized and leave typical abrasive grooves upon ejection since oxide typically has higher hardness then the bulk (see top row of Figure 2-3 (b)). The duo mechanisms in this zone are grouped as **oxido-abrasive wear**[36].

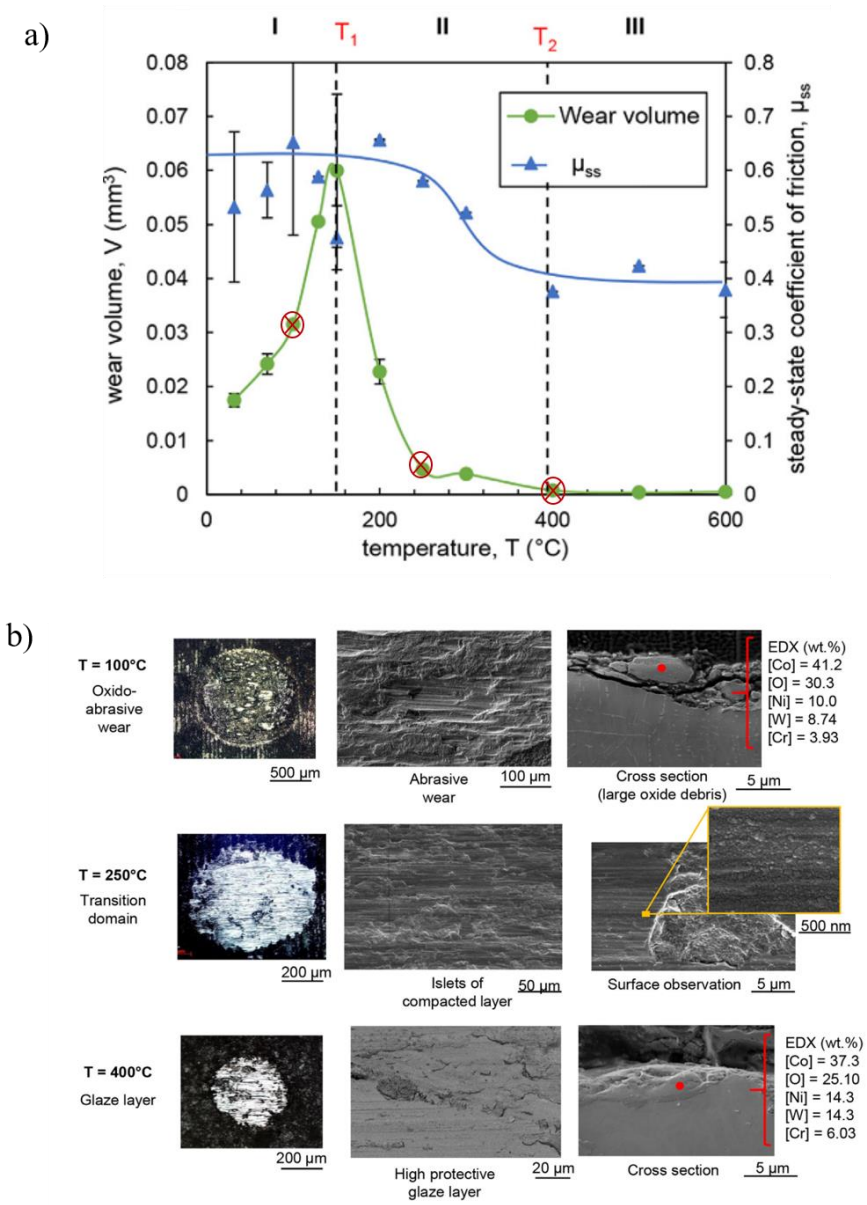

Figure 2-3 a) Example of severe-to-mild wear transition for wear volume loss and steady state coefficient of friction as a function of temperature. Tests were conducted with Co-Cr alloy on Alumina cross-cylinder tribo system (normal force *P* = 50N, sliding amplitude δ^*=± 20μm, frequency *f*=50Hz, cycle *N* = 200K). In this case no wear was detected on Alumina and the wear loss are only from Co-Cr counterpart. Typical temperature for domain I (100°C), II (250°C), and III (400°C) are cross-labeled in red; b) Comparison of the fretting scar morphology on Co-Cr (optical, SEM and EDX) at typical temperature for each domain [36]

Domain II (T1 < T <T2): intermediate domain, i.e. severe-to-mild transition domain, where a sharp decrease in COF and wear volume is observed. In this temperature range,

the debris become more cohesive due to metal diffusion, and thus stays longer at the contact surface to be crushed into nanoscale particles (see middle row of Figure 2-3). Those small debris particles are compacted but not sintered (at least not sintered until later cycles), thus the wear loss in this domain consists of a large contribution of the running-in abrasive wear in the early cycles (similar to domain I). This abrasive wear cycle portion in total cycle decreases with increase of temperature, thus a decrease in wear loss with temperature is observed in this zone. With the progression of glaze layer formation, the real time COF is also observed to gradually decrease and then stabilize at a low level.

Domain III (T > T2): mild wear domain, where both wear volume and COF remain low. The high temperature in this range promotes a quasi-instantaneous formation of glaze layer in less than 5K cycles, and wear volume is almost negligible. Wear scars of tests in this domain are bright and smooth, and the compacted layer shows no distinguishable debris, which indicate completion of sintering (see bottom row of Figure 2-3).

It is important to note that the phenomenon of decreasing friction and wear lost at higher temperatures occurs across many different material couples, although the magnitude of friction/wear and their reduction, characteristic temperature T1 and T2, and specific trend of COF and wear versus temperature in domain I can vary depending on the material couples, test conditions and contact configuration [21,29,31,35,37]. See examples in Figure 2-4. Regarding the compositional influence, glaze layers are found to form with oxides that exhibit higher oxygen diffusivity [27,38,39]. As an example, under same fretting conditions at 600°C, a glaze layer formed at a Co/Co interface, but the oxides in either Cr/Cr or Ni/Ni interfaces were poorly adhered and did not sinter to form glaze layer[39].

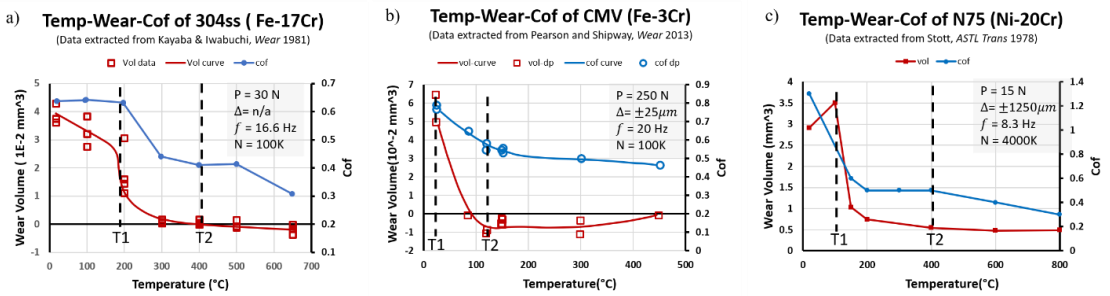

Figure 2-4 Selected COF and volume loss as a function of ambient temperature reported in literature with their testing condition (normal force (P), displacement amplitude(Δ), frequency (f) and total cycle(N). Data digitized from source: a)304 like-on-like line sliding [29]; b) low alloy like-on-like cylinder on flat fretting[30]; c) Ni-20Cr alloy like-on-like cylinder-on-flat reciprocating sliding[21]. Note how the characteristic temperature T1 and T2 and the wear behavior in domain I (T<T1) is different in each case and comparing to Figure 2-3.

Many theories have been proposed to describe the severe-to-mild wear transition with temperature [14,27,40,41].To summarize, the temperature dependence of the severe-to-mild wear transition may be explained by the following three aspects:

1) Changing the oxidation/diffusion rate. Based on the tribo-sintering theory[36,42], the formation of glaze layer is a sintering process of oxide or oxidized debris to a certain thickness. The temperature-dependence of diffusion-controlled oxide scale thickening process follows the Arrhenius equation:

$$k = k_0 exp(\frac{-E_a}{RT}) \quad (2\text{-}1)$$

where k is the oxidational rate, k_0 is the Arrhenius constant, E_a the activation energy, R the ideal gas constant, and T the ambient temperature. Comparing to static oxidation, oxidation during wear (i.e., tribo-oxidation) is found to have similar E_a

but significantly different k_0 [43,44]. The strong dependence of k_0 is associated with the condition of the contact surface and subsurface voids/dislocations that are altered and progressed during the wear process.

2) Altering the mechanical property of the bodies undergoing fretting and reciprocating sliding, and furthermore determines whether the third-body debris are retained (reduce wear) or ejected (increase wear). With increasing of temperature, the adhesion energy between fine debris are increased, and the bonded debris are more likely to be retained to develop a protective glaze layer[20,45]. The softer metal two-body at high temperature also promote retention of the debris[46]. On the other hand, the perfect ductile behavior of glaze layer at high temperature also enable it to protect the substrate[26].

3) Determining the stoichiometric oxide that one metal may produce. For example, the element Fe, the main chemical component of steel, the dominant oxide formed at temperature lower than 200°C is α-Fe_2O_3. At 200°C-500°C, Fe_3O_4 becomes the main type of oxide. Above 500°C, additional FeO can be formed[35]. Given that T1 temperature for many steel system is close 200°C, which happens to be the transition temperature between α-Fe_2O_3 and Fe_3O_4, many researchers have attribute the severe-to-mild wear transition to the increasing amount of Fe_3O_4 observed at the interface[29,47–49], and explained that Fe_3O_4 can form a more protective oxide layer because of its lower hardness (thus less abrasive wear) and better adhesion to construct a stable compacted debris bed[50,51]. However, it has been observed in other works that a stable glaze layer can be formed with artificially fed α-Fe_2O_3 particles[27,52], and 400°C tribo-test produced Fe_3O_4 did not generate protective

oxide layer successfully at higher load because the bulk body (tempered sorbite) was too soft[53]. It may then be concluded the role of the specific type of oxide relies on the testing condition as well as the properties of the two bodies, and thus the temperature's role in severe-to-mild transition through oxide type determination remains ambiguous and not conclusive yet.

While the studies mentioned above dived deep in why temperature can play an important role in severe-to-mild wear transition, few of them reached to a quantitative wear law to predict wear transition and its associated critical temperature for glaze layer initiation and stabilization, T1 and T2. Besides, the test condition dependence (normal force, amplitude, frequency) on T1 and T2 is not clear.

Very recently, a critical cycle (N_{GL}) model was proposed based on a series of cross-cylinder fretting experimental results of Co-Cr alloy/Alumina tribo pair. The apparent criteria for glaze layer formation is sufficient number of fretting cycles, i.e. $N > N_{GL}$. The critical cycle, N_{GL} is a function of both fretting parameters (frequency *f*, sliding amplitude δ^*), environmental parameters (ambient temperature *T*), and intrinsic material properties (sinter parameter S_{GL} and oxidation activation energy E_a). This model also assumes parabolic oxidation rate for Co-Cr alloy[54]:

$$N_{GL} = \frac{S_{GL}}{\delta^{*2} exp(\frac{-E_a}{RT})} f \tag{2-2}$$

Since cycle is equivalent to time for a fixed frequency, knowing that glaze layer is a tribo-sintering process, this equation is essentially equivalent to a sintering rate (S_{GL}) critera.

According to this model, increasing temperature, increasing sliding amplitude, or decreasing frequency will lead to decrease in N_{GL}, and thus faster glaze layer formation. The wear mechanism boundary between oxido-abrasive wear and glaze layer response wear determined by the N_{GL} model is demonstrated in Figure 2-5.

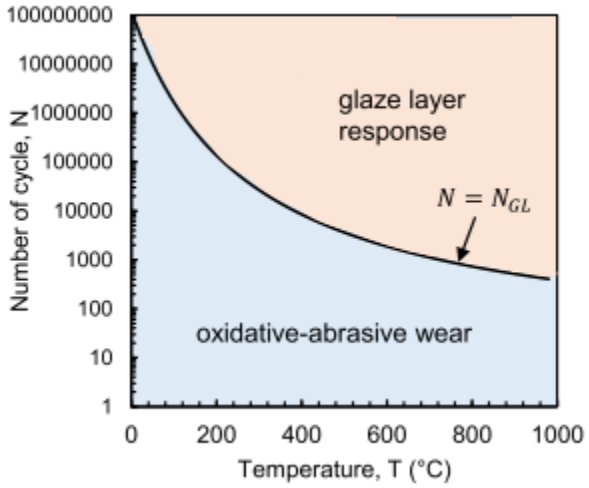

Figure 2-5 A demonstration map of glaze layer formation when temperature varies based on N_{GL} model for Co-Cr/Alumina cross-cylinder tribo pairs. Map constructed with data shown in Fig 2.3 (P = 50N, f = 50Hz, δ* = ±20μm).[54]

This model also brings in deeper understanding on the severe-to-mild transition with increasing temperature shown in Fig 2.3 (a), and the essence of the two characteristic temperatures -- T1 and T2. That is: N_{GL} decreases with increasing of temperature, and the total wear volume loss is mostly contributed by abrasive wear of the cycles *before* N_{GL} is achieved. In domain I, $N_{tot} < N_{GL}$, no glaze layer will be formed and oxido-abrasive wear, which leads to severe wear loss, will happen though out the complete process. For domain II, $N_{tot} > N_{GL}$, glaze layer activation will happen before the end of the test, and thus the oxido-abrasive wear will only take place for N_{GL} cycles, and minimal increment in wear beyond that cycle due to glaze layer production. In this domain, the higher the

temperature, the smaller the N_{GL}, and thus the less the wear volume. In domain III, T > T2, N_{GL} is sufficiently small compared to N_{tot}, hence, the glaze layer will start functionalized at early stage of wear, and the wear behavior is controlled by the performance of the glaze layer. In summary, the two characteristic temperatures, T1, and T2, are the critical temperatures at which $N_{GL} \approx N_{tot}$, and $N_{GL} \ll N_{tot}$, respectively. Here we define T2 as the temperature when $\frac{N_{GL}}{N_{tot}} = 0.1$ to have a precise value of T2.

It is worth noting that the "temperature" discussed here and the cited works is mostly environmental or ambient temperature since it's easier to measure. However, rigorously speaking it is the temperature at contact interface that brings in "temperature-dependence" on wear. In fact, the fretting process itself can induce local temperature rise at the contact as a result of the dissipation of the friction power[55,56]. Dissipated energy is a function of many parameters. Unlike parameters like load and sliding amplitude whose variation influences dissipative is complicated and hard to quantify, frequency's influence in dissipative energy is simply linear[57], and thus studying the frequency as the other major parameter is convenient to segment fretting induced temperature rise. The fretting-induced (or dissipative energy induced) temperature rise at contact as a function of frequency will be discussed more in detail in 2.3.

2.3 Role of frequency in fretting wear

The cyclic frequency in fretting and reciprocating sliding has been found to be another important parameter that influences the wear rate and mechanism of wear. Generally, increasing frequency has been found to reduce wear rate, especially at lower temperature [58–60]. The role of frequency is closely related to the kinetics of oxide debris formation.

One direct evidence is provided by Uhlig and co-workers[58]. In their work, a 58% reduction in wear rate was observed in steel/steel tribo-pair's contact by increasing frequency from 1Hz to 50Hz, yet this effect disappeared when conducting the same test at inert atmosphere, providing evidence that the frequency effect is associated with the formation of oxides or other corrosion/reaction products [59]. The role of frequency in friction and wear can be addressed both in terms of time and its influence on increasing temperature from Coulomb heating:

(1) Frequency directly determines the interaction time between bodies and asperities in contact. The time of diffusion and oxidation of two bodies in contact and the third-body debris will influence formation and stability of glaze layer, which eventually influence friction and wear. For fretting or reciprocating test, the time to finish one cycle, t is inversely related to frequency:

$$t = \frac{1}{f} \tag{2-3}$$

The higher the frequency, the shorter the time for each cycle, and for a fixed number of cycles, a shorter period of wear. A short interpass time per cycle brought by high frequency may be beneficial or detrimental, depending on the dominant wear mechanism happening at the interface, which is furthermore temperature-dependent as discussed in 2.2. An interactive diagram shown in Figure 2-6 [57] illustrates the influence chain (from right to left) of temperature and frequency to surface damage. In this diagram, the plus (+) and minus (-) sign before each item

in the diagram represent increasing (or enhancement) and decreasing (or diminution) effect respectively. At low temperature the severe wear domain (Domain I) where the dominant wear mechanism is abrasive wear, increasing frequency can suppress the formation of abrasive oxides and thus reduce surface damage. At higher temperature (Domains II and III) when glaze layer starts to form from stable debris bed, increasing of frequency reduces the time for oxidation between interactions of asperities in the contact, and thus does not encourage the formation of a protective glaze layer [2,54]. The role of frequency in N_{GL} model addresses this time characteristic, and predicts a positive proportional relationship between frequency and critical cycle for glaze layer formation. From (2-2, the N_{GL} model predited the number of cycles necessary to initiate glaze layer formation increases with frequency [36], although this judgement needs to be varified.

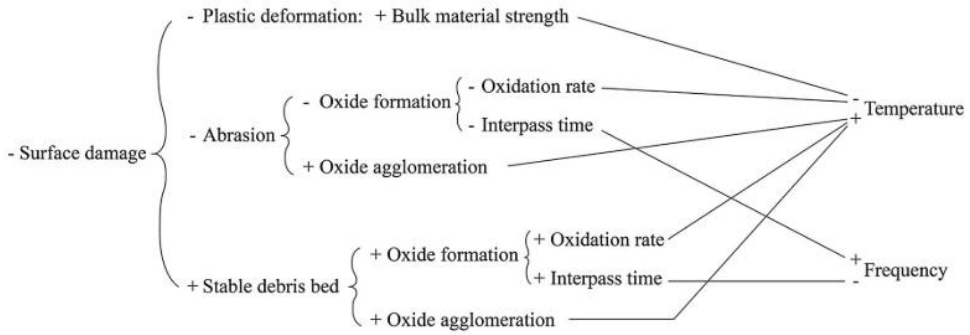

Figure 2-6 Interaction diagram that links temperature and frequency with several main wear features to determine wear damage [35].

(2) Increasing frequency can also increase the temperature in the contact, which is beneficial for glaze layer formation. The fretting induced temperature rise, associated with the “flash temperature” and its conduction away from the

interaction [61], is a result of energy dissipated during fretting, and the dissipated energy is proportional to the oscillation frequency. If dissipative energy induces a temperature rise (as a function of frequency) is known, this part of influence from frequency may be converted equivalently to the influence of temperature.

Since in-situ measurement of temperature at the contact is very challenging [49,62], analytical and numerical models are typically used to predict the flash temperature[61,63–66]. Recently, Jin and Shipway conducted a finite element analysis to study the frequency dependence on the average temperature rise considering contact area change as well as the thermal property change at the interface of like metal due to the composed oxide [57]. This model provides a steady state solution, assuming a constant dissipated energy E_d during fretting as the only power input, and Carslaw and Jaeger's solution of temperature rise on a semi-infinite space was applied [67]. If taking the center of contact in a cylinder on flat configuration as the coordinate origin, the temperature rises ΔT at point (x', y') can be calculated as follows:

$$\Delta T = \int_{-b}^{b} \frac{p(x) 4\delta \mu_E f}{4\pi\kappa} \left\{ \ln \frac{4\kappa t}{[(x-x')^2 + y^2]\rho C} - \gamma \right\} dx \tag{2-4}$$

where $p(x)$ is Hertzian contact pressure, b the half-width of the contact, δ the sliding amplitude, μ_E, the dissipative energy coefficient (E-COF, defined as energy dissipated per sliding distance and load , more details in Section 3.3), f is the oscillation frequency, κ the thermal conductivity, t the time, ρ the density, C the specific heat, and $\gamma = 0.5772$ the Euler constant. The far end of the temperature rise predicted by Eq. (2-4) was further

confirmed experimentally by comparing it to measured temperature captured via a fine sheathed thermocouple attached in a hole parallelly underneath the fretting contact.

The key simulation results for 304 stainless steel in like-on-like cylinder-on-flat fretting condition at 20Hz and 200Hz is presented in Figure 2-7. While simulating flash temperature and local temperature rise is beyond the scope of this project, there are some interesting takeaways relevant to this work:

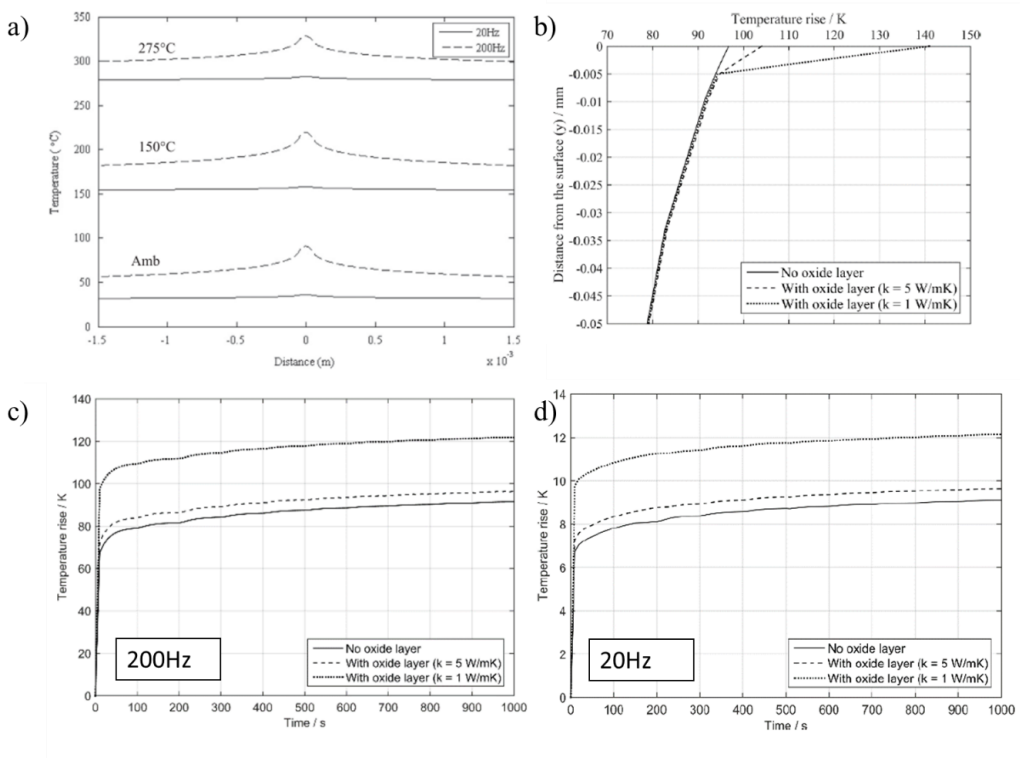

Figure 2-7 Temperature rise prediction for 304 like-on-like cylinder on flat fretting tests at 20Hz and 200Hz (P =450N, $\Delta = 50\mu m$, μ_E = 0.6) a): Prediction of local surface temperature rise in contact after 100K fretting cycle as a function of distance from center; b)predicted origin (x = 0) temperature rise as a function of distance below the surface at 1000s for 200Hz test with inclusion of 5µm thick oxide layer with different thermal properties ; c-d) comparison of predicted temperature rise at the fixed origin with inclusion of a 5µm thick oxide layer with different thermal properties for 1000s.[57,68]

- As shown in Figure 2.7 (a), the centerline (x=0) is the highest temperature rise. For f = 200Hz, ΔT is predicted to be 70℃. ΔT drops with increasing of distance from the centerline. The rate of this drop is high near the centerline, but when distance is beyond 1.5mm, ΔT is less sensitive to the distance. Based on the trend presented in Figure 2-7(a), the ΔT at 5mm away from the center of the contact is about 50℃, which is about 71% of the temperature rise at the contact center.
- As shown in Figure 2-7(c) and (d), the majority of the temperature rise is achieved at the very beginning of the test. With progress of the test, the contact geometry evolves and the contact pressure is reduced, which brings down the dissipated energy per cycle and thus provides a lower heating power slowing down the increasing rate of ΔT.
- ΔT is propotional to dissipated energy. Considering the same duration (i.e., constant total time t) and same μ_E, the temperature rise is proportional to frequency f (as indicated in Eq.(2-4) and Figure 2-6(c-d)). It is thus possible to estimate temperature rise for a similar fretting system using this simulation result by simply scaling the dissipative energy, μ_E, and frequency difference.
- As shown in Figure 2-7(b), the existence of Oxide layer will further increase ΔT at contact, because the low thermal conductivity prevents dissipation of frictional energy. The smaller the thermal conductivity of the oxide layer, the higher the ΔT. In experiment, however, a lower μ_E is expected after formation of glaze layer, which violate the original assumption that μ_E is constant, so this prediction may not be accurate.

2.4 Wear maps

Wear maps are one of the best approaches to visualize wear mechanisms and their transitions at a range of given operating conditions (amplitude, frequency, normal force, etc.). Since the 1980s when they were introduced, this these maps have been widely adapted in tribology research for many material couples and test configurations[69–72], to support engineering of moving interfaces in mechanical systems, and to inspire wear modeling.

A typical wear map consists of a two-dimensional space with different combinations of two independent parameters that can influence wear behavior, and a third-dimension (sometimes by color-coded[73], contour plot[72], or by different marks[52]) showing the level of *steady-state* wear performance (i.e., COF, wear rate, or volume or weight loss), whose transitional changes can imply a change in wear mechanism or wear mode. By changing the two independent parameters used, a series of wear maps can be generated, and provide a multi-dimensional graphical presentation of wear data.

The functional relationships with physical parameters representing the boundaries between mechanisms can be used to determine how different material couples, test conditions, and contact configurations can be unified and compared.

One of the most classic and well-known mechanism maps was developed by Lim and Ashby from 1980s to 1990s[72]. An example of one of their wear maps is shown in Figure 2-8. The two axes are dimensionless with normalized velocity ($\tilde{v}$ = velocity*contact radius/thermal diffusivity) on one and normalized pressure ($\tilde{F}$, normal contact pressure/surface hardness) on the other. The wear performance indicator is the normalized

wear rate ($\widetilde{W}$, volume loss per unit area slid). By using many references of reported work for steel-on-steel tribo-pairs tested with pin-on-disk configuration, all of the data was consolidated into a map [72]. The base mono-color wear map was classified by severe wear, mild wear or a transition zone, with the transition zone shown shaded, while the colors classify the wear mechanism. Combining the two map shows that severe wear and mild wear can be associated with different wear mechanisms, while the same wear mechanism (oxidational wear, for example) can result in either severe wear or mild wear, which again shows the complexity nature of wear. The curved boundaries between wear mechanisms indicate a correlated contribution and the impact of $\tilde{v}$ and $\tilde{F}$ on the wear mechanism determination. This work is also capable to unify the normal force-dependent, distance-dependent and velocity-dependent wear behavior discovered separately in most tribocouples where only a couple of the variables are changed. In other words, each test result represents one slice on a 2D wear map, what we will term as univariable tests. The fact that the severe-to-mild wear transition is highly sensitive to normalized velocity change, implies a more complex velocity dependence compared to pressure, especially at lower values of $\tilde{F}$.

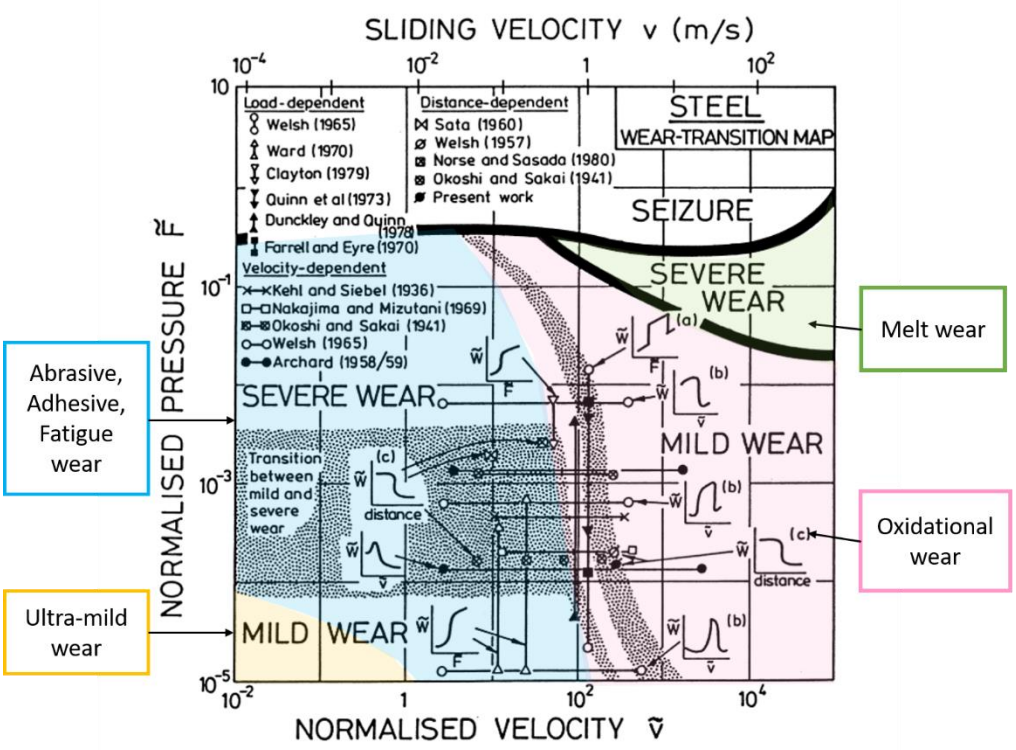

Figure 2-8 A combined Lim-Ashby wear map with base of wear transition between mild and severe wear[74], and color shad represent different wear mechanism (extracted from reference[72]). This wear map is for room temperature steel-on-steel pin-on-disk configuration. The gray shaded areas represent transition between mild & severe wear.

While many of the fretting conditions (such as sliding speed, normal force, etc.) have been chosen as independent variables in many past works including Lim and Ashby's, it is less common to have environmental conditions (such as ambient temperature, oxygen level, etc.) in a wear map. While temperature has been the most studied environmental parameter as a univariable, it was not until the last two decades that it has been put in wear maps to study its coupling effect with other parameters, typically the normal force. Nevertheless, the temperature range is usually limited by equipment capability, and only some special high temperature Ni, Co, and Si alloys [32,75,76] or special coatings [77] in the pin-on-disc configuration have been studied and reported. It is even rarer to find a wear map in

literature that chose both temperature and frequency as the two independent variables, after all, the duo role of frequency and its coupling effect with environmental temperature on glaze layer formation has not been systematically studied until recently [35,57,60]. One close substitution of a temperature-frequency wear map is the map concerning temperature and sliding speed in a continuous and non-reciprocating motion. Figure 2-9 presents one of such map reported by Inman et al. [33]. This map summarizes a series of test results for a Ni alloy (Nimonic 80A, 76Ni-19Cr) versus a Co alloy (Stellite 6, 60Co-27Cr) in reciprocating-block-on-rotational-cylinder motion. In this map, as the sliding speed increased, the boundary between low-temperature mild wear zone and other zones shifted to lower temperature end, which reflected the frictional heating influence brought by increasing of sliding speed. Glaze layer protection was only achieved at low sliding speed, whereas the oxidized debris occurred at high-temperature high-sliding speed end did not sinter as a glaze layer. While this wear map hinted at possible boundary shift resulting from temperature rise and critical parameter window for glaze layer formation, the unconventional contact configuration as well as considerable error brought by using weight change as the wear performance indicator limited the application of this map.

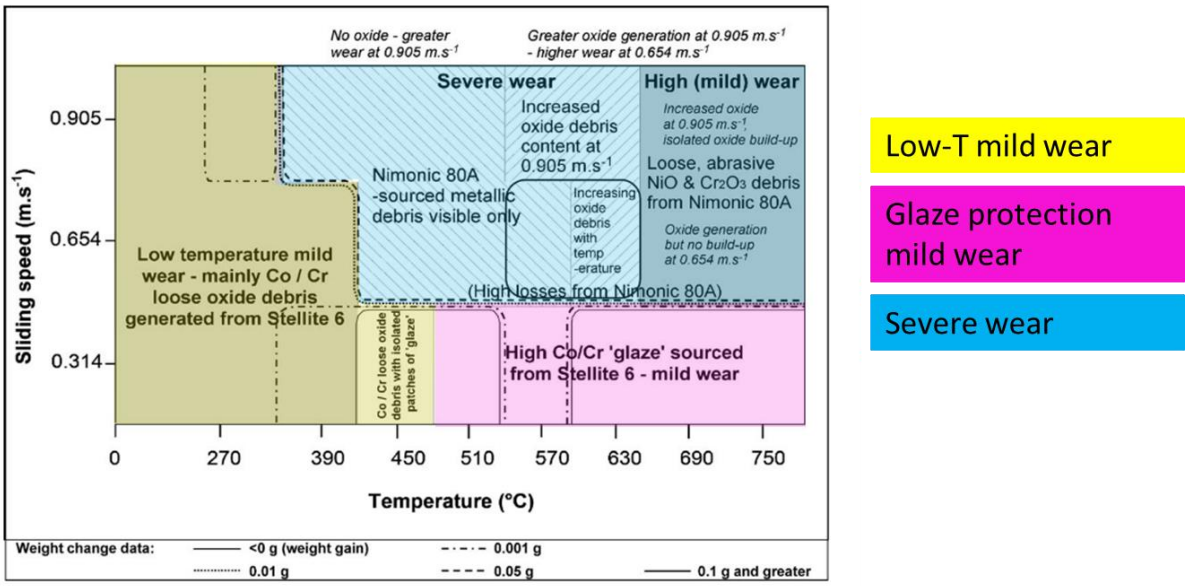

Figure 2-9 Temperature-sliding speed wear map of Nimonic 80A vs Stellite 6 (P = 7N, sliding distance = 5422m) with weight loss in contour and zones for major wear mechanisms are recolored. [33]

2.5 Austenitic stainless steel

Austenitic stainless steel is a large family of stainless steel with austenite (face-centered-cubic) as their primary crystalline structure[78]. In general, austenitic stainless steel is a nonmagnetic, material with excellent ductility, formability and toughness. It can be further hardened by cold working but not heat treatment.

An intuitive composition and property relationship between 300 grades austenitic stainless steels can be found in Figure 2-10[79]. The nickel (Ni) or nitrogen (N) are the most commonly used elements in austenitic stainless steel to stabilize the austenite, while chromium (Cr) or molybdenum (Mo) are added to achieve better corrosion resistance for high temperature applications or chloride environments[80]. High Ni content can help to

decrease the strain-hardening rate, (e.g. Type 305[81]). Low carbon grades (designated as AISI L or S) are developed to prevent intergranular corrosion[78] and improve weldability properties. Austenitic stainless steel may go through martensitic transition with deformation and/or reduction in temperature. Increasing the level of alloying or increasing temperature can increase the stability of austenitic stainless steel from martensitic transition[82]. For example, at room temperature, type 310 (25Cr-20Ni) is stable, while type 304 (18Cr-8Ni) is metastable and can undergo a strain-induced transformation to martensite in the layers adjacent to the interface undergoing wear[83].

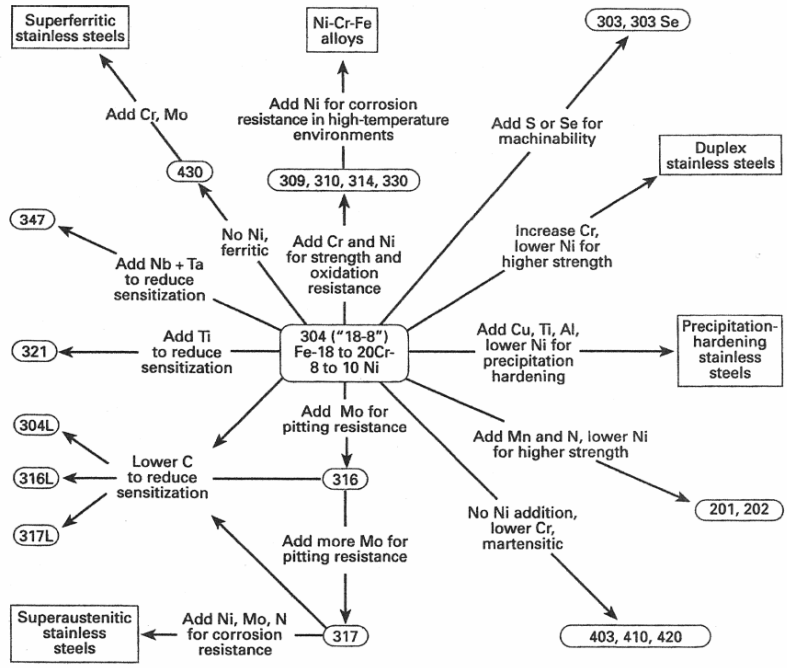

Figure 2-10 Composition and property linkage for 300 series austenitic stainless steel.[79]

The good high temperature resistance and relative low cost 310/310S austenitic stainless steel, compared to Ni-base alloys, makes it a great candidate for many cost-sensitive high temperature applications like internal component in combustion engines, furnace parts,

heat-treatment baskets, aerospace propulsion system and metalworking system [78,84]. However, due to the limitation of testing and characterization equipment, most existing research on wear performance of type 310/310S does not cover its working temperature range, nor has accurate wear volume data been recorded[83,85], and therefore, a wear map for 310 cannot be readily generated. Comparing to type 310, 304 has lower Cr and Ni and thus is not the best austenitic stainless steel for extremely high temperature use. However, its easy accessibility and wide-use makes it a favorite baseline material for many tribological tests on austenitic stainless steels [35,83,86–88].

2.6 Objective of the dissertation

The ultimate goal is to develop a complete methodology to construct an informatic and applicable wear mechanism map, targeting the influence of temperature and frequency on wear mechanisms determination. It is accomplished by conducting wear experiments under various combination of temperature and frequency. While a wear map can be experimentally obtained by summarize tribological test results at these various testing conditions, the coupling of different parameters often make it challenging to understand with a purely empirical approach. Therefore, modeling correlations and characterization of wear behavior are necessary to identify the operating wear mechanisms needed to gain deeper insights of wear mechanisms and better understand the underlying reasons for the trends observed in experimentally-based wear map. Ultimately, the goal is to conceive and derive wear models that predict the boundaries separating different mechanisms on a wear map using a minimal number of tests to calibrate or assess these models. Though a literature review in previous sections of this chapter, it is clear that the glaze layer plays an important

role in severe-to-mild wear transition in high temperature wear, and thus is a key structure to determine wear performance under high temperature wear.

The austenitic stainless steel 310S is chosen as a sample system to generate temperature-frequency wear map that covers considerably large temperature and frequency in its working condition than that have previous been considered. This stainless steel is commonly used in high temperature applications due to its good high temperature and hot corrosion resistance compared to more common austenitic stainless steels such as 304 and is used in components undergoing fretting or reciprocating sliding. A baseline wear map (or equivalently sufficient amount of data to generate a wear map) for 310S/310S does not exist. Such wear map is needed to eventually explore the behavior of 310S with other processing methods that alters the wear behavior such as gas nitriding and borizing. Before these advanced surface treatment methods can be systematically studied, a baseline wear mechanism map for 310S needs to be established.

While glaze layer is the key structure formed to promote severe-to-mild wear transition, the identification of glaze layer has been mostly relying on eyeballing, as its characteristics reported, including bright, reflective, flat, etc. are all qualitative. A quantitative descriptor of glaze layer is desired as the foundation of more advanced characterization and analysis of glaze layer's role in wear protection.

CHAPTER 3. MATERIAL AND EXPERIMENTAL METHODS

3.1 High temperature fretting and reciprocating sliding test system

Tribological tests were conducted using a unique Phoenix Tribology DN55 High Temperature Fretting and Reciprocating Sliding test system (Newbury, UK). A schematic of this test system is shown in Figure 3-1(a). It consists of a servohydraulic actuator to which a moving specimen is clamped. The moving specimen, often referred to as the pin, can be a sphere for point contacts, a cylinder for line contacts, or a flat-ended geometry for area contacts. On both sides of the moving specimen are arms that secure a flat stationary specimen. This setup allows the simultaneous collection of two sets of wear data in one test, one from the left channel("1") and the other from the right channel ("2").

The displacement amplitude Δ^* and frequency f are the control variables to the servohydraulic actuator. The normal force P is applied by a pneumatic actuator with feed-back control from an inline load cell. The tangential force Q induced by friction is recorded by a piezoelectric sensor and real time displacement of the moving specimen Δ is measured by a capacitance gage, which is used for feedback control in the fretting mode.

Heating of the system is performed using a clamshell furnace surrounding the contact region as shown in Figure 3-1(a). The furnace temperature is monitored and controlled with a thermocouple build in the furnace, and the furnace temperature variation is less than ±1°C during the test, and additional 30°C is added when commanding furnace temperature to compensate temperature offset that we observed in calibration procedure. A Type-K thermocouple is spot welded on the right plate specimen near contact area for monitoring

the sample temperature. Depending on the desired furnace temperature, one to two hours of temporary hold was programmed before starting the test to stabilize the heat flux in chamber and the tests samples. The sample temperature captured by the thermocouple at the end of the temperature hold is defined as the environmental temperature (T^E) for the test. The real time temperature at thermocouple location, T^{TC}, is recorded in LSD during the test to estimate the temperature at contact surface. The furnace chamber has access to lab air atmosphere but can be sealed with positive pressure of inert gas flowing to reduce oxygen supply if desired.

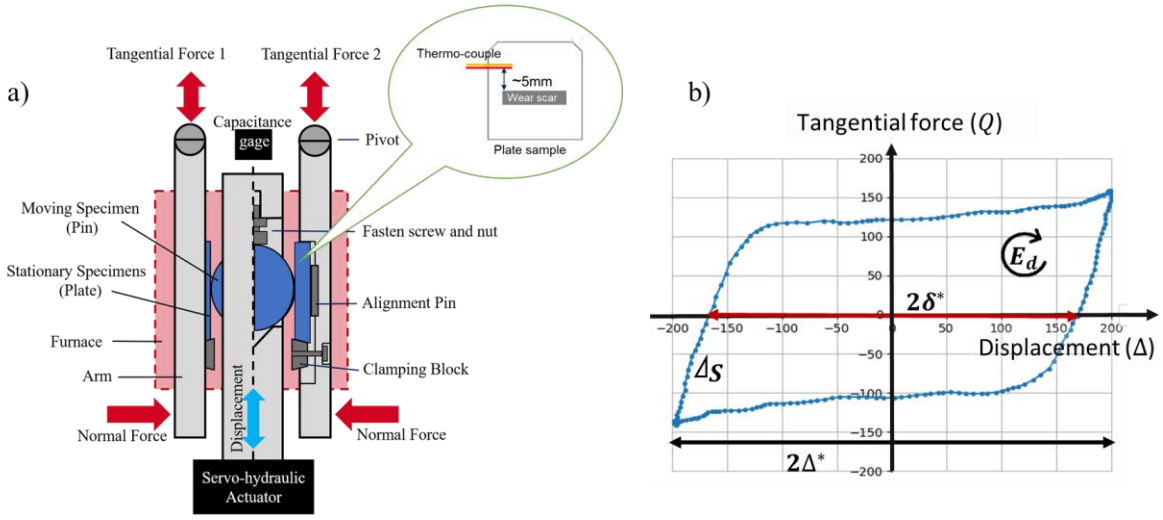

Figure 3-1 a) Schematic diagram of DN55 testing rig and relative position between thermocouple and wear scar. b) A hysteresis loop generated with data recorded in HSD file, with δ*, Δ* and S geometrically defined in the loop.

The test sequence and data acquisition mode vary to best accommodate each testing condition combinations. As a general rule, depending on the test frequency f, the high-speed data (HSD) acquisition system stores the real time tangential force Q and displacement Δ in the host computer at a rate of $200f(Hz)$ for $f \leq 10$Hz, which means 1000 data points for five neighbor full fretting cycles are sampled. At frequency higher

than 10Hz, the data acquisition rate is limited by the system responding rate, and thus for 50Hz and 100Hz test, 300 data points for five neighbor full fretting cycles are sampled. Noise with frequency higher than $10f$ in tangential force signal is removed by low pass filter build in the system. Additional HDS files are generated in the early 10K cycles to promote amplitude ramping. For example, for 10Hz tests, one HSD file is generated every 3 seconds for the first 10K cycles and every 10 seconds for the rest of the cycles. An example of the hysteresis response of tangential force Q and displacement (Δ) that can be reproduced with HSD data can be found in Figure 3-1 (b), and from this data, a COF can be calculated (see Section 3.3 for more details).

After the completion of fretting tests and system cooling down, the pin and plate specimens are removed from test frame and ultrasonically cleaned in pure ethanol for 10 minutes to remove loose debris attached to the worn surface and surfaces are protected for further characterization.

3.2 Material and Specimen

The fretting tests were conducted with 310S stainless steel. 310S is a low carbon version of 310 stainless steel, its maximum carbon content is 0.08%wt. The raw material was purchased from Penn Stainless Product, Inc., as a hot rolled and annealed plate of 9.5mm (0.375 in.) thickness and round bar of 25.4mm (1.0 in.) diameter. Optical image of the microstructure of 310S pin material is shown in Figure 3-2) after etch by C13 reagent. The averaged grain size is about 120μm. The chemical composition of the 310S material measured by EDS is very closed to the that is provided by vendor (listed in Table 3-1).

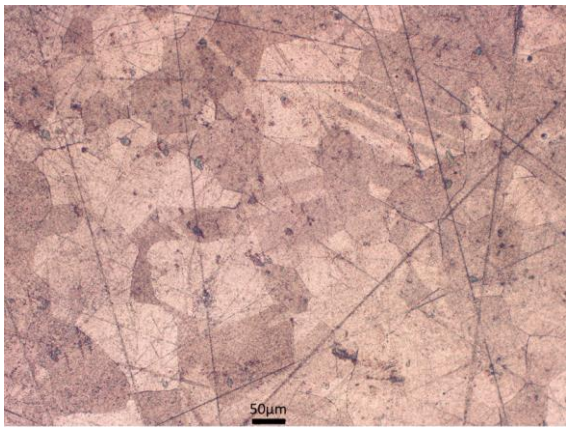

Figure 3-2 Microstructure of 310S pin sample under microscope, etched by C13 reagent, 100X

Table 3-1 Chemical composition(wt%) of 310S raw material

	C%	Si%	P%	S%	Cr%	Ni%	Mn%	Mo%	Cu%	Fe%
Datasheet	0.03	0.46	0.028	0.00	24.49	19.54	1.49	0.16	0.41	balance
Measured	-	0.4	-	-	24.6	18.8	1.5	-	-	53.7

To evaluate the mechanical property difference between plate and round bar raw materials and the temperature influence in the mechanical properties, uniaxial tensile tests were conducted using flat and cylindrical dog-bone specimens that are machined from the plate and round bar, respectively. The dimension of the specimens can be found in Figure 3-3 following ASTM E8-16 standard. The cross-section gage area for flat and cylindrical specimens were kept the same to make the result comparable. The uniaxial tensile tests were conducted at room temperature(18°C), 200°C, 400°C, 600°C and 800°C with MTS servohydraulic test system for both the cylindrical and flat specimens in strain rate control mode (0.015mm/mm/min). All high temperature tensile tests were conducted in lab atmosphere with induction coil heating system. The test results are summarized in Figure 3-4, overlapped with 310/310S data reported in literature[89–92] as references. For both

plate and round bar material, the room temperature tensile properties meet the minimum requirements that is provided by the vendor (Table 3-2). The mechanical property differences between flat and cylindrical specimens, hence the plate and round bar material, are less than 10%.

Table 3-2 Room temperature mechanical properties of annealed 310S (extracted from supplier documentation)

UNS designation	Type	Tensile Strength (min)	Yield Strength (min)	Poisson's ratio	Vickers Hardness	Modulus of Elasticity	
S31008	310S	>515 MPa	>205 MPa	0.3	>150	in tension(E) >200GPa	in shear (G) >77.2GPa

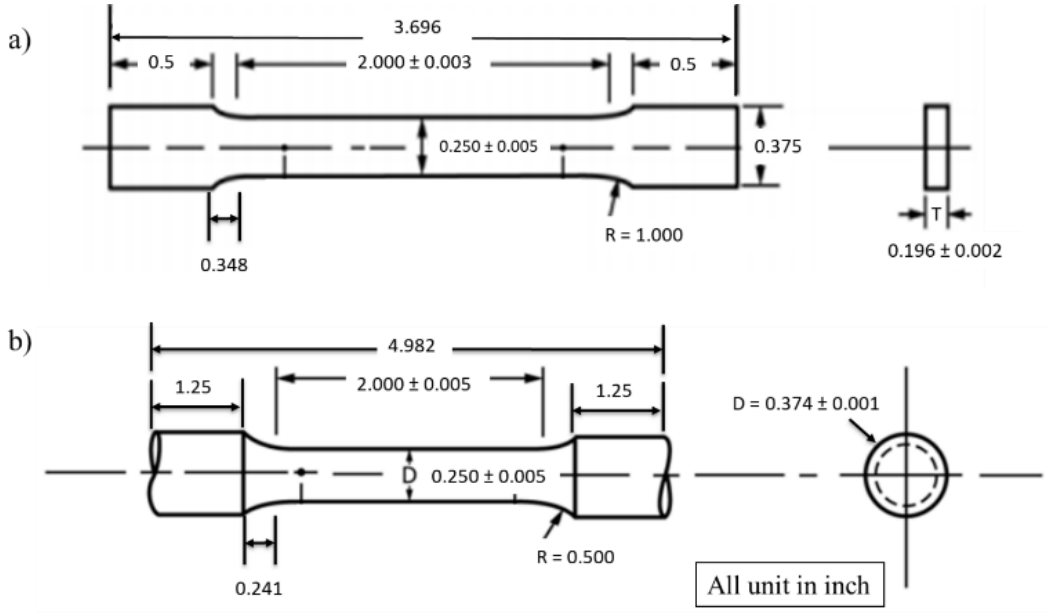

Figure 3-3 Dimension design of a) flat tensile specimens; b) cylindrical tensile specimens. The dimensions came from ASTM E8-10 standard [93].

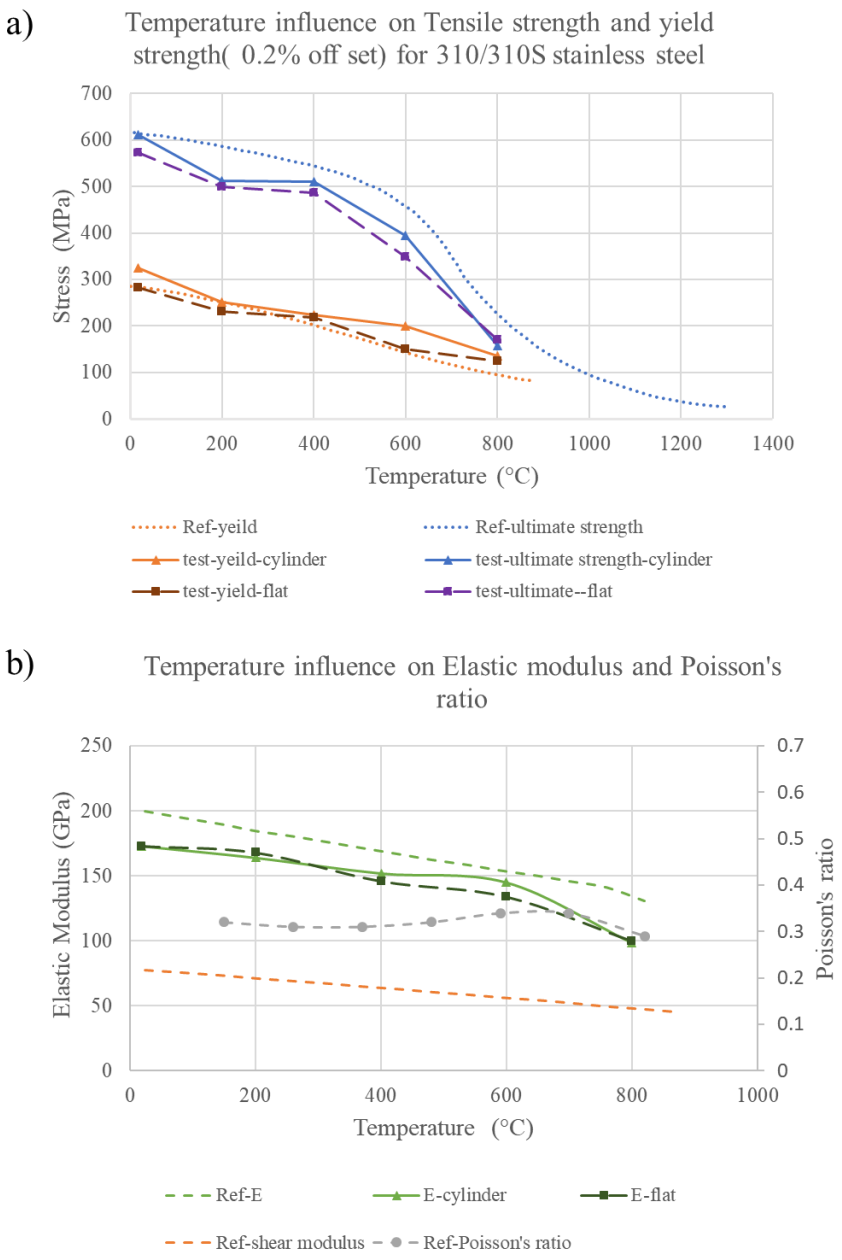

Figure 3-4 Effect of temperature on the a) tensile properties of 310S raw material, reference is data of annealed type 310 stainless steel from ref[92] and b)Young's modulus of 310S raw material and reference Young's modulus, shear modulus and Poisson's ratio of 310/310S stainless steel reported in [89–91]

The raw material was machined to the desired dimensions as shown in Figure 3-5 (a) for the plate and pin specimens for tribological tests. The work hardening layer on flat samples

(plate) was removed by polishing up to 4000 grit SiC paper, and the cylindrical samples (pin) were used as lathed. The average Vickers hardness for pin is about 250 HV0.5, and plate about 230 HV0.5. This result is between cold rolling hardness (275 HV) and annealed hardness (150HV) for 310/310S stainless steel[92].

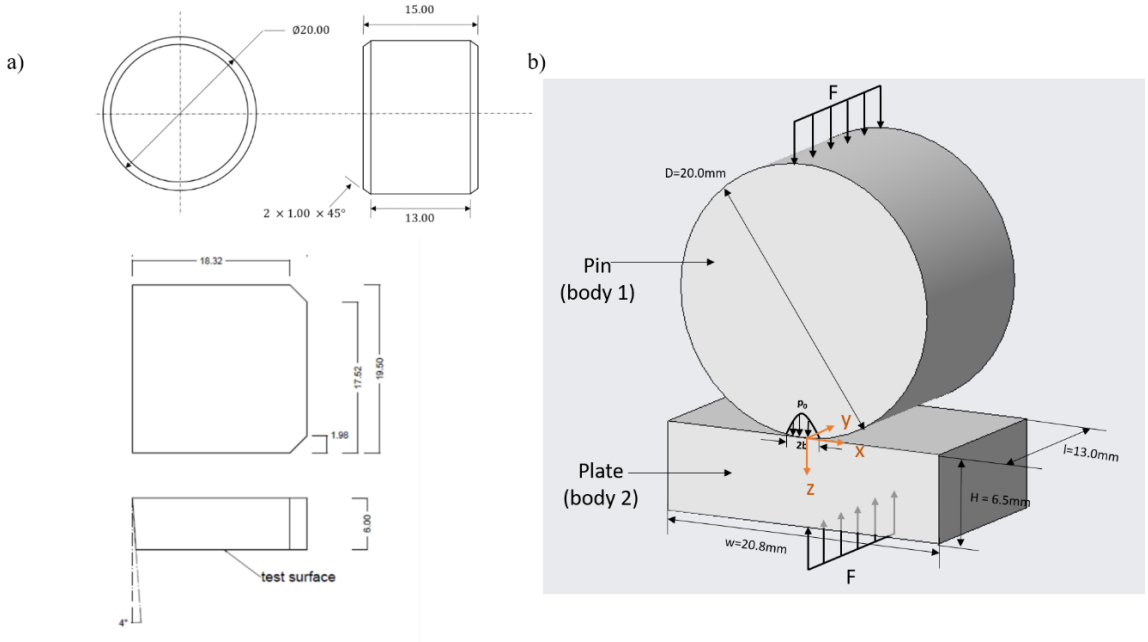

Figure 3-5 a) Dimensions of pin (top) and plate (bottom) specimens; b) Notation for Hertzian line-contact calculations for line contact configuration with current sample dimensions.

The radius and length of the moving specimen (pin) was designed to represent the contact configuration of pivot-vanes/ring configuration in variable geometry turbocharger (VGT, also called variable-nozzle turbine, VNT), a typical application of 310S stainless steel and one of the industrial applications that have been evaluated with our system. Our DN55 is designed to operate best with normal force between 100 N and 2500 N. To maintain nominal Hertzian contact pressures below the yield strength upon initial application of the normal force using the sample dimensions and considering the mechanical properties of

310S, a normal force of 150N is chosen. At room temperature, with a Hertzian line-contact condition, the contact area is a long narrow rectangular with width of 2*b* and length of *l*. The configuration and notation can be found in Figure 3-5. Data in Table 3-2 is used to calculate the maximum contact pressure (Hertz pressure) and the semi-width, *b*, of the contact. The equations are simplified for the same material of two bodies[94]:

For a line contact, the normal force per unit length $P = F/l$ = 150N/13mm = 11.54N/mm. The maximum Hertz pressure p_0 is located at the center of contact, and can be calculated by:

$$p_0 = \frac{2P}{\pi b} = \sqrt{\frac{PE^*}{\pi R^*}} \tag{3-1}$$

where equivalent radius R^* is calculated by:

$$R^* = \left(\frac{1}{R_1} + \frac{1}{R_2}\right)^{-1} = R_1 = 10mm \tag{3-2}$$

equivalent elastic modulus E^* is:

$$E^* = \left(\frac{1-v_1^2}{E_1} + \frac{1-v_2^2}{E_2}\right)^{-1} = \frac{E_1}{2(1-v_1^2)} \approx 109.89\ GPa \tag{3-3}$$

and the semi-contact length b is calculated by:

$$b = \sqrt{\frac{4PR^*}{\pi E^*}} \approx 36.6\ \mu m \tag{3-4}$$

With Eq. (3-1) to Eq (3-4) the maximum contact pressure is calculated to be 201MPa, and thus the maximum principal shear stress is [94]:

$$\tau_1 = 0.30p_0 \approx 60.3MPa,\ at\ x = 0,\ z = 0.78b \approx 28.5\mu m \tag{3-5}$$

Using the Tresca criterion, the yield strength in shear $\tau_Y = \frac{\sigma_Y}{2} = 102.5$ MPa, which is above the τ_1 ensuring nominally elastic conditions upon initial application of the normal force. Using Eq. (3), the maximum normal force for onset of inelastic deformation at room temperature is as 434 N, well above the normal force of 150 N that will be used. It can also be calculated using the tensile test results reported in Figure 3-4, that the reference normal force 150N will ensure nominally elastic condition at initial stage of the test at all tested temperature.

3.3 Calculation of Coefficient of friction

The coefficient of friction (COF) is one of the most important wear performance indicators of a material. COF is mostly obtained experimentally. In general, COF is defined by Eq. (3-5):

$$\mu = \frac{Q}{P} \tag{3-5}$$

where P is applied normal force and Q is the tangential force measured. The testing rig used in this work, DN55, tracks the real time tangential force and normal force, which can be used to calculate COF for each reciprocating cycle. In fretting test, the tangential force displacement response for gross slip is shown in Figure 3-6 (a). The tangential force Q

does not always remain constant in the sliding region as shown. Depending on the method used to average Q in such case, slightly different values of COF can be obtained:

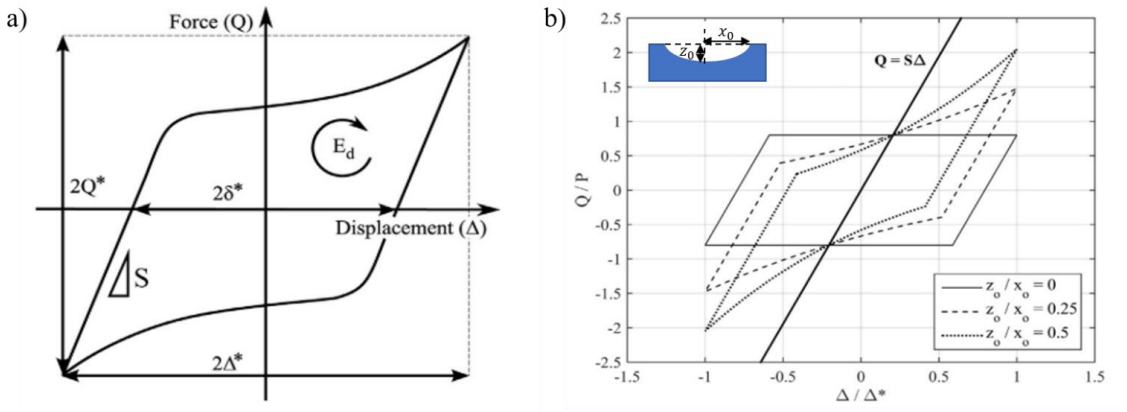

Figure 3-6 a) Schematic of a hysteresis fretting loop with hook-like increase in tractional force during gross sliding, with δ^*, Δ^* and S geometrically defined in the loop; b) Comparison of fretting loops with grooves of different aspect ratio sharing the same Q along Q = SΔ line, the aspect ratio of the groove is defined as sub plot on upper left [95]**;**

Energy Coefficient of Friction (E-COF, or μ_E) considers the energy dissipated in one fretting loop, E_d, which represented by the area within a hysteresis loop. A representative COF of the cycle with total sliding stroke of 4 δ^* is therefore defined as [56]:

$$\mu_E = \frac{E_d}{4P\delta^*} \tag{3-6}$$

E_d is the energy dissipated in one fretting cycle, represented by area within a hysteresis loop; P the normal force and δ^* the sliding amplitude defined as the displacement when tangential force is zero. In most cases due to non-negligible system stiffness, S, represented by the slope for direction change portion in hysteresis loop, δ^* will be smaller then displacement amplitude, Δ^*. See Figure 3-6 (a) for δ^*, Δ^* *and* S identified from hysteresis

loop, and their corresponding representation in hysteresis loop obtained in our tests in Figure 3-1(b).

Geometric-independent COF (GI-COF) considers that the tangential force lying on the line of:

$$Q^* = S\Delta \tag{3-7}$$

to be the average tangential force, where S is the system stiffness and Δ is the instantaneous displacement amplitude. Since this Q remains unchanged with cornerwise stretching of the hysteresis loop due to groove shape change as wear propagates [95], illustrated in Figure 3-6 (b). A similar approach (μ_H) is to use the averaged tangential force near the center of the sliding region in each direction [96] as defined Q in Eq. (3-5). Considering the symmetry of a friction hysteresis loop, this method would result in a COF that is very close to GI-COF.

$$\mu_H = \frac{\bar{Q}_{center\ of\ sliding}}{P} \tag{3-8}$$

To understand and compare different COF calculation methods, a practice on calculating different type of COF numerically from HSD file is demonstrated in Figure 3-7. Here the dissipated energy in one fretting cycle is calculated by:

$$E_d = \sum_{i=1}^{n} \frac{(F_i + F_{i+1})}{2} * (d_{i+1} - d_i) \tag{3-9}$$

where F_i and d_i are the tangential force and displacement of the i-th data point and n is the total data point in one fretting cycle (n = 200 in this case). The sliding amplitude δ^* is determined by the displacement at zero tangential force (averaged by both directions, labeled in purple). The geometry independent tangential force Q^* is found by the data point that's closest to the line Q*=SΔ, where S is the slope of linear fitted elastic slope in hysteresis loop (labeled in gold)

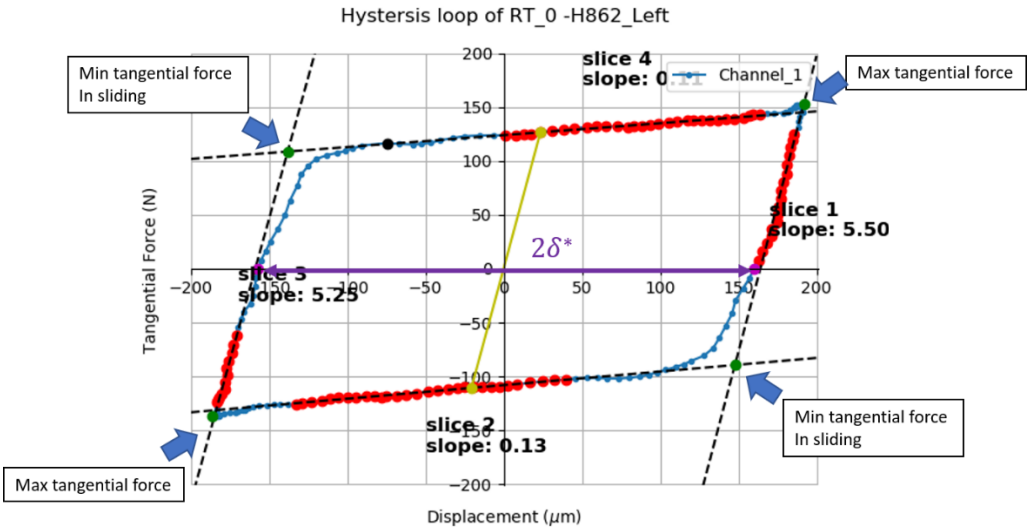

Figure 3-7 Demonstration on numerical determination on GI_COF (tangential force determination for GI-COF in gold), max/min tangential force (in green), and sliding amplitude δ* (in purple).

In addition to E-COF and GI-COF as introduced above, **Max-COF** and **Min-COF** are also calculated as a reference of upper and lower COF boundary:

$$max\text{-}COF = \frac{\bar{Q}_{max\ disp}}{P} \tag{3-10}$$

$$min\text{-}COF = \frac{\bar{Q}_{min\ in\ sliding}}{P} \tag{3-11}$$

where $\bar{Q}_{\max in\ sliding}$ and $\bar{Q}_{\min in\ sliding}$ are the averaged maximum and minimum tangential force achieved at two extrema displacement position of a cycle. $Q_{\max in\ sliding}$ is defined as the maximum tangential force in each sliding direction, and $Q_{\min in\ sliding}$ is numerically calculated as the interception of two linear fitted neighbor edge in hysteresis loop (linear fitted line in dash, $Q_{\max in\ sliding}$ and $Q_{\max in\ sliding}$ in green) as shown in Figure 3-7. The DN55 system also records the root mean square (RMS) of tangential force signal through its RMS/DC chip (AD536AJD) every one second. This RMS averaged tangential force is used as friction force (Q) in Eq. (3-5), and the COF calculated this way is denoted as **DN55-COF** in this work. Since DN55-COF considers RMS of tangential force in complete cycles, its calculated Q is expected to be smaller than that of E-COF and GI-COF and be closer to min-COF. To avoid underestimation on friction, DN55-COF is only presented as a reference value and not used for wear performance evaluations.

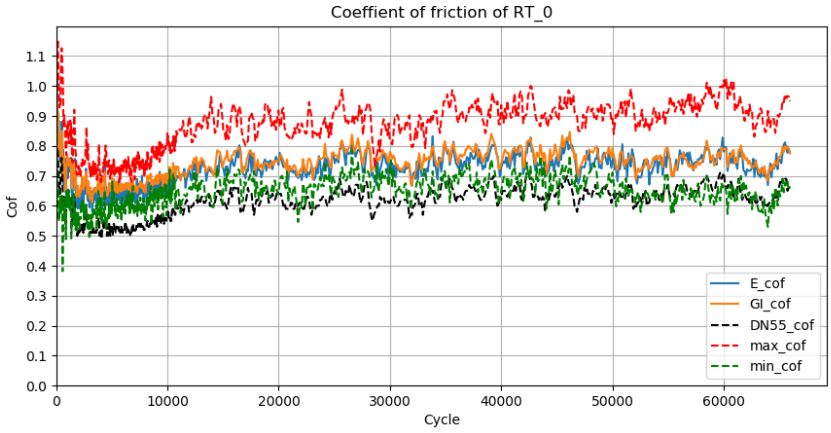

Figure 3-8 Different COF calculation method using HSD data of a room temperature test.

Different types of coefficient of friction versus cycle count for a room temperature test are shown in Figure 3-8. As expected, both E-COF and GI-COF falls between max-COF and

min-COF, which demonstrates that both of them are a good method for providing the representative COF for an ideal shaped hysteresis loop. E-COF and GI-COF are very close to each other in all tests conducted so far, with GI-COF being slightly smaller for some low temperature cases (the steady state COF difference is less than 3%). The reason for the small difference between the two COF is due to the small stiffness over load ratio(i.e. S/P) for the testing rig[95]. In the following presented work, E-COF will be used unless noted otherwise. Real time E-COF (μ_E) in the last 20K cycle of a test is averaged and reported as the stabilized or steady state COF ($\bar{\mu}_E$) for each test condition.

3.4 Wear characterizations

The morphologies of the wear scar are measured by optical microscope (Leica DVM6 Wetzlar, Germany) in normal mode and Z-stack mode with combined Coaxial illumination (CXI) and Ring lighting (RL) lightning mode at full aperture. Specific setting of optical microscope for glaze layer identification purpose are introduced in Section 5.3.1.1.

The morphology as well as chemical composition of structures formed at worn surface have been examined with the Hitachi SU-8230 SEM (Tokyo, Japan) using both secondary electron (SE) and backscattered electron (BSE) modes, and FEI Quanta 250 (Oregon, USA) with InLens detector that collect SE and BSE signals at the same time. Specifically, the SE images are used to identify the glaze layer or other features in the near surface layers by its unique surface topography compared to the unworn surfaces, and BSE images are used to distinguish and locate the metal oxides, since BSE image is highly sensitive to differences in atomic number, and low atomic number element like oxygen will appear darker in the image. The identification of oxygen element oxide is confirmed by the Oxford EDS

detector (Massachusetts, US) equipped with Hitachi 8230 SEM. Some samples were also cross-sectioned and hot-press mounting with conductive resin, polished with SiC grit paper and diamond suspension to examine the thickness of the glaze layer formed.

The topography of both the pin and plate sample are 3D reconstructed by an optical profilometer (Zygo Zegage, Middlefield, CT, USA) using a 10X lens. As shown in Figure 3-9 (a), by defining unworn surface as reference, volume up (V^{up}, material build up) and volume down (V^{down}, material removal, or transferred volume as defined in other work[60]) with respect to reference (unworn area) can be calculated. These calculations are readily performed using the Zygo Mx software (version 7.5.0.1).

There are two major ways to report total volume loss in literature with different emphasis:

$$V^{sum} = V^{up} + V^{down} \tag{3-12}$$

$$V^{net} = V^{up} - V^{down} \tag{3-13}$$

In both case V^{up} and V^{down} are positive values, and they represent a summed contribution from both pin and plate, i.e.,

$$V^{up} = V_{pin}^{up} + V_{plate}^{up} \tag{3-14}$$

$$V^{down} = V_{pin}^{down} + V_{plate}^{down} \tag{3-15}$$

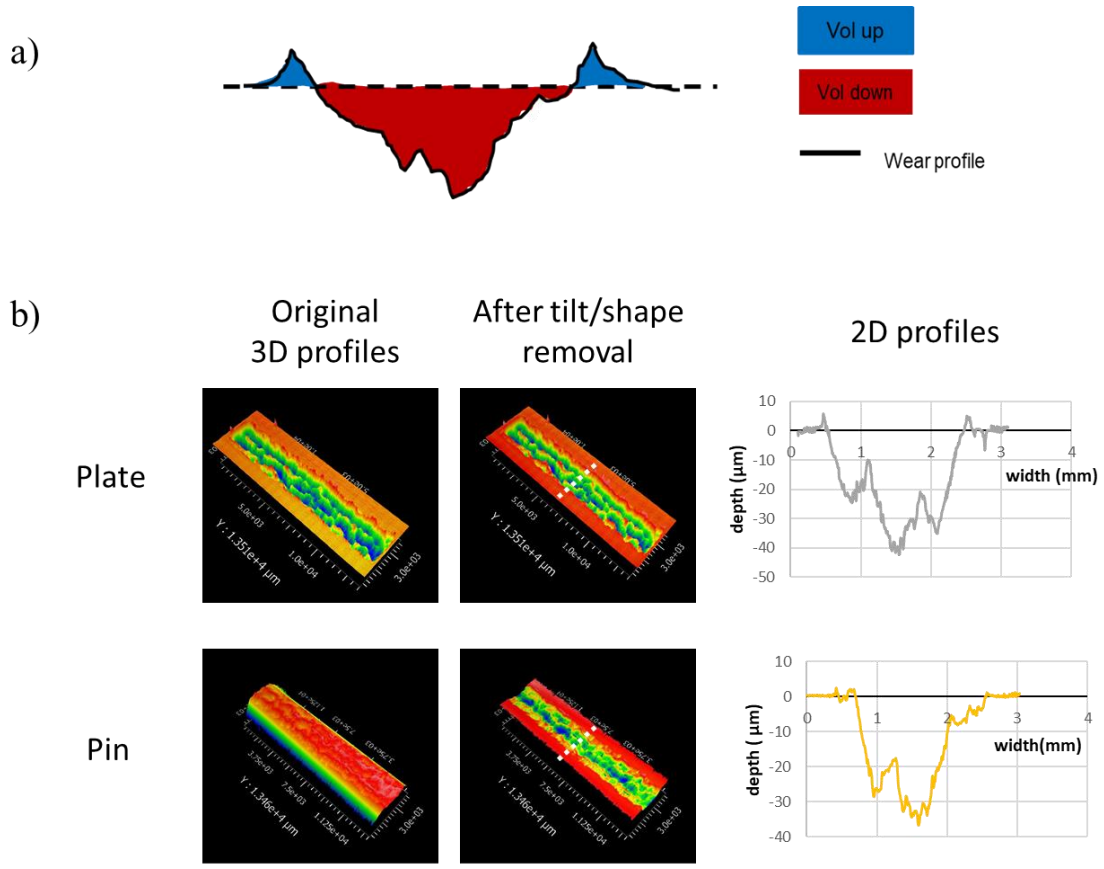

Figure 3-9 a) Schematic of volume up (V^{up}) and volume down (V^{down}) to the reference (unworn surface) in dash. b) Example of surface profile processing with form removal on pin and plate. (Test condition: T = 100℃, $P = 150$N, $\Delta^* = 200$μm, $f = 10$Hz)

The value of V^{sum} accentuates the transition of material between the two bodies, while V^{net} puts emphasis on the net material loss. Since V^{up} in the current test set up is usually very small comparing to V^{down} (especially in lower temperature where plastic deformation is not as severe), we are expecting V^{net} to be almost always negative, and both V^{sum} and $-V^{net}$ showing very similar trend. At higher temperatures (>500°C), more debris is believed to be welded at the edge of wear scar, which makes V^{up} increase and therefore a

there is a larger deviation between V^{sum} and $-V^{net}$. In the future discussions, $-V^{net}$ will be used as wear volume loss for consistency unless specified.

Some of the tests were conducted at different normal force(P), sliding amplitude(δ*) and cycle(N), which will significantly influence wear volume as suggested by Archard law[8]. To make those results comparable, the volume loss/gain are normalized to the rate of the wear/transfer using the following equations[57], and the net wear rate (NWR) will be used for related discussions:

Wear rate:
$$\dot{V}^{down} = \frac{V^{down}}{4\delta^* PN} \tag{3-16}$$

Transfer rate:
$$\dot{V}^{up} = \frac{V^{up}}{4\delta^* PN} \tag{3-17}$$

Net wear rate (NWR):
$$\dot{V}^{net} = \frac{V^{net}}{4\delta^* PN} = \frac{V^{up} - V^{down}}{4\delta^* PN} \tag{3-18}$$

CHAPTER 4. CONSTRUCTION OF WEAR MECHANISM MAPS

This chapter presents experiments and methods used to construct a Temperature-Frequency wear mechanism map for 310S on 310S stainless steel tribological couple. Most of the existing wear maps commonly focused on load (normal force), displacement amplitude and moving velocity, and no temperature-frequency wear map for 310S has been reported in literature. The wear map is constructed based on results of a series of cylinder-on-flat fretting test conducted at various testing conditions with the coupling effect between the environmental temperature and oscillation frequency being the target of this work. The planning of experiments is designed to reduce number of tests necessary but still maintain a reasonable resolution of the boundaries between wear regions. The N_{GL} model, which was proposed based on fretting wear of Co-Cr alloy on alumina cross-cylinder to predict the critical cycles for glaze layer formation, is applied to the 310S/310S cylinder-on-flat couple. In the experiments, a cycle-dependent μ_E drop in the transition zone of severe-to-mild wear transition has been observed, and the cycle numbers upon finishing 99% of the drop is defined as N_{GL} though sigmoid fitting of the μ_E data with temperature. The resulting analysis shows that the N_{GL} model can be used for wear map boundary prediction particularly if the temperature rise at the contact surface due to Coulomb heating is accounted for. The general principles of constructing and utilizing an informatic wear map is also provided.

4.1 Design of Experiment

To experimentally obtain a temperature-frequency wear mechanism map requires an abundance of tests conducted at various temperatures and frequencies. Certainly, the

greater number of tests conducted at various combinations of temperature and frequency, the better the resolution the map can achieve. Since it is impossible to run infinite tests, a sophisticated design of experiment is needed to reduce the number of tests yet still achieve a reasonable resolution of the wear map.

In a traditional test matrix that involves one or more variables, testing conditions are often evenly distributed throughout the covered range for each parameter. Convenient and straightforward as this strategy is, it is not effective for tasks like generating a wear mechanism map, as the total number of tests can easily scale up quickly to improve the boundary resolution. Knowing the boundary resolution is controlled by the sampling density near the boundary, we proposed a hierarchical probing strategy with a biased sampling density in the wear map that adaptively determines the choice of test condition for new experiments based on knowledge learnt in finished experiments.

Figure 4-1 illustrates the proposed sampling strategy, presenting the actual sampling locations, i.e., the temperature-frequency combinations in each fretting test, for the final wear map generated for 310S/310S cylinder-on-flat tribo system. This strategy involves four levels: baseline, course grid, fine grid, and extra probing. Firstly, in the baseline level (Figure 4-1(a)), a series of univariable tests, namely temperature-baseline and frequency-baseline tests are conducted, where temperature and frequency are the only variable in their own baseline. Extra data points may be added in the transition zone discovered at this level. The results of the two baselines reveal the separate influence of environmental temperature and frequency on wear performance. The possible coupling effects between temperature and frequency are then assessed in later levels as illustrated in Figure 4-1(b): a screening

at course grid level that covers the complete range of temperature and frequency to recognize the major wear mechanism and their transition zone, a fine grid level around the transition zone to identify the transition boundaries, and finally the extra probing points to confirm wear mechanism zones and further improve the boundary resolution. The grid density for each level is determined based on the result from the earlier level, and will be discussed in detail in the following sections. After finishing those steps, a temperature-frequency wear mechanism map at a constant cycle, amplitude and normal force is constructed. The following sections introduce results collected at each level and demonstrate generating a wear map following this strategy. All probing points represented in Figure 4-1(b) represent tests conducted for the same number of cycles (66K), displacement amplitude (±200μm), and normal force (150N). Several extended cycling tests (100K) have also been conducted to further address the cycle influence on wear.

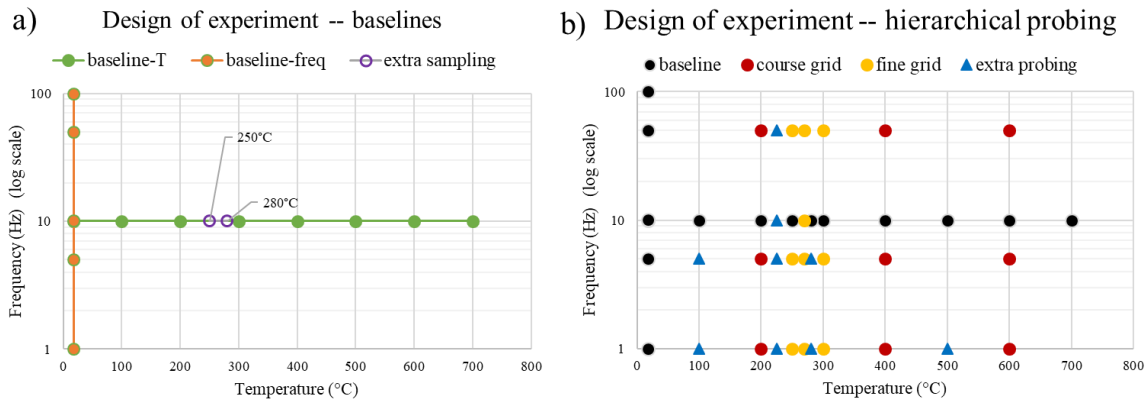

Figure 4-1 Design of experiment generating wear mechanism map with hierarchical probing strategy: a) baseline tests; b) complete strategy.

4.2 Univariable temperature-baseline test

The temperature-baseline tests cover the complete temperature range that 310S may be exposed to in applications from room temperature (18°C) to 700°C with 100°C increment in between. A moderate frequency (10Hz) is chosen and fixed for the baseline tests at all temperatures. At least three tests per condition were conducted to verify the repeatability of the test result.

The correlation of the μ_E and net wear volume rate (NWR) is shown in Figure 4-2 (a). The error bars indicate the standard deviation from the three duplicate tests. The results demonstrate great repeatability especially at higher temperatures, where the error bars are too small to be visible in the plot. The severe-to-mild wear transition was observed in 200-300°C range and thus two additional tests at intermediate temperatures within this temperature range (250°C and 280°C) were conducted to capture more details in the transition zone. The μ_E versus cycle plot for the tests in transition temperature zone ($250℃, 280℃, 300℃$) are shown in Figure 4-2(b). The sharp drop in steady-state μ_E between $250℃$ and $300℃$ is clearly observed. The running-in COF for all three temperature were high and close to 0.7, but as the cycle count increased, μ_E for $300℃$ and $280℃$ dropped one after another and stabilized at a lower level, while μ_E for $250℃$ remained high for the entire test duration of 66K cycle. With additional cycling at 250°C, the μ_E drop was observed (red curve in Figure 4-2 (b)). The magnitude of the μ_E for all temperatures after the μ_E drop at the transition is very close to each other (about 0.42)

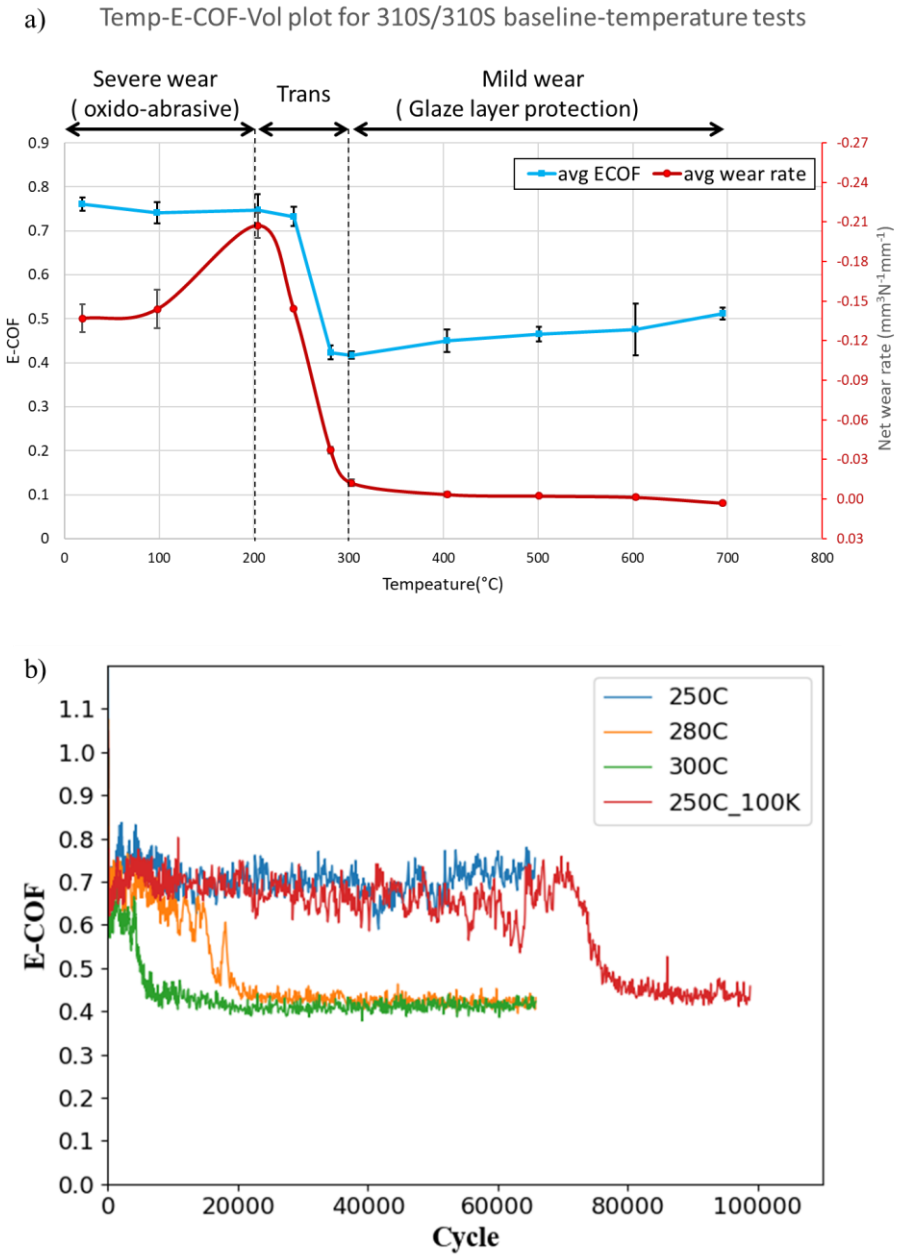

Figure 4-2 a) Evolution of μ_E and net wear rate ($\dot{V}$ net) with temperature using 310S/310S temperature-baseline results. $\dot{V}$ net is plotted with inverse axes, b) Typical μ_E evolution with cycle plot for 250°C (N_{tot} = 66K cycles in blue N_{tot} = 100K cycles in red), 280°C and 300°C, the three temperature that falls in transition temperatures zone as labeled in a).

The amount of wear as quantified by V^{up} and V^{down} contributed by pin and plate at each temperature is shown Figure 4-3. In general, the trend of volume loss with environmental

temperature for the pin and plate are very similar due to their identical chemical and mechanical properties. For both the pin and plate, V^{up} gradually increases with increase in temperature, whereas V^{down} first increases then decreases with temperature, which is a similar trend comparing to evolution of μ_E. At the same time, V^{up} and V^{down} for pin are larger than plate since pin has less confined surface which promotes debris removal. Similarly, V_{pin}^{up} is less than V_{plate}^{up}, as fast extraction of debris inhibits debris welding at the edge of the wear scar.

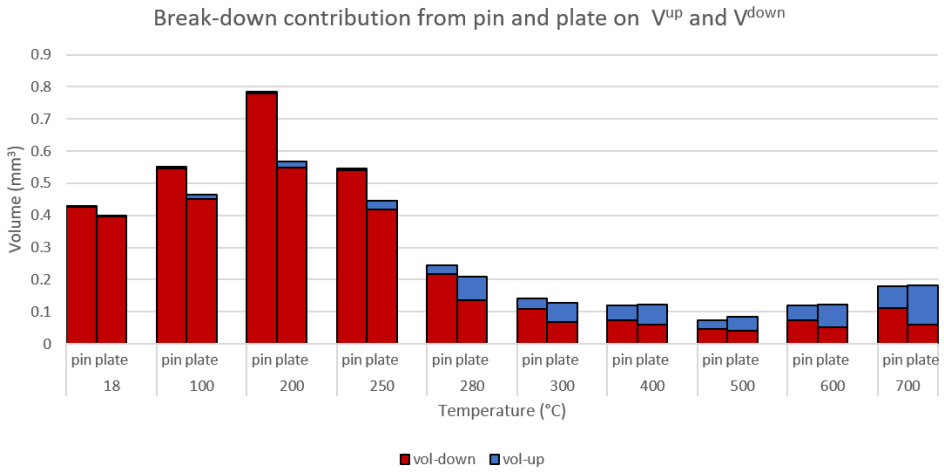

Figure 4-3 Volume up and down contributed by pin and plate for each temperature, results are averaged from 3 duplicates and their left/right channels.

SEM observations of the wear scar further confirmed that the severe-to-mild wear transition occurs due to the glaze layer formation. The top view of the worn surfaces of the plates after tested at 250°C for N_{tot} =66K and 100K, and 400°C for N_{tot} =66K are shown in Figure 4-4. Lighter elements like oxygen show darker color in SEM with BSE signal, which helps to identify the glaze layer. While compacted oxide debris was observed at the worn surface for 250℃ after 66K cycle, it did not form a sufficient glaze layer, and thus

the μ_E did not drop at this condition. When the number of cycles is increased to 100K cycle at 250°C, the μ_E drops between 70K and 80K cycles, and small islands of glaze layer are observed. As shown in Figure 4-4(e), abrasive grooves along fretting directions are found on the glaze layer islands. For tests conducted at 400°C, where the μ_E drop happened at an early stage of the test (less than 1K cycle), large patches of glaze layer are formed. An enlarged area of the glaze layer formed at 400°C (Figure 4-4(f)) shows shallower abrasive grooves, which may be due to the higher strength of the glaze layer or softer oxide debris at elevated temperature.

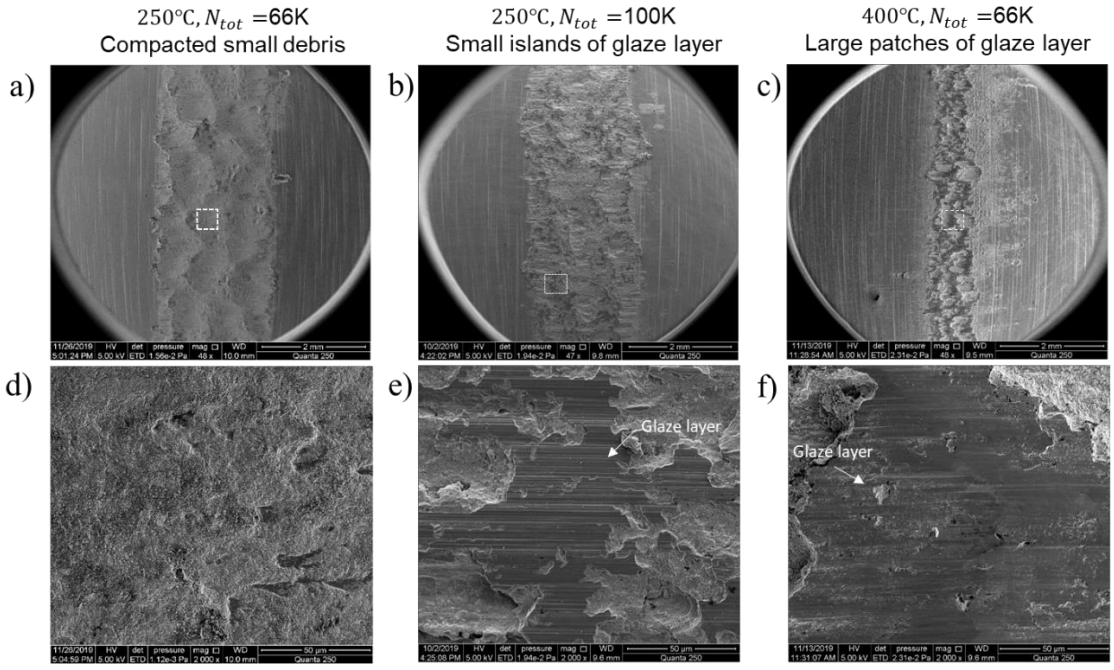

Figure 4-4 SEM of wear scars on plate sample from top view. (a) and (d): 250°C test with 66K cycle, where debris were compacted but not forming sufficient glaze layer; (b) and (e):250°C test with 100K cycle, where small island of glaze layer (in black) was formed, and the enlarged image (e) shows the sintered and flat feature of glaze layer and abrasive wear groove along the fretting direction; (c) and (f): 400°C test

with 66K cycles, where large network of glaze layer is formed, and the enlarged image (f) shows a large area of glaze layer with less abrasive grooves.

The chemical composition at three different locations, (1) center of glaze layer, (2) edge of glaze layer, and (3) outside of glaze layer but still within the wear scar, and static oxide that formed outside of wear scar are given in Table 4-1, with specific locations shown in Figure 4-5, for wear scar on the plate tested at 700℃. The oxygen weight percentage is significantly higher in the glaze layer area compared to spot 3 as well as static oxide formed outside the wear scar. These results confirmed that the glaze layer is oxide rich.

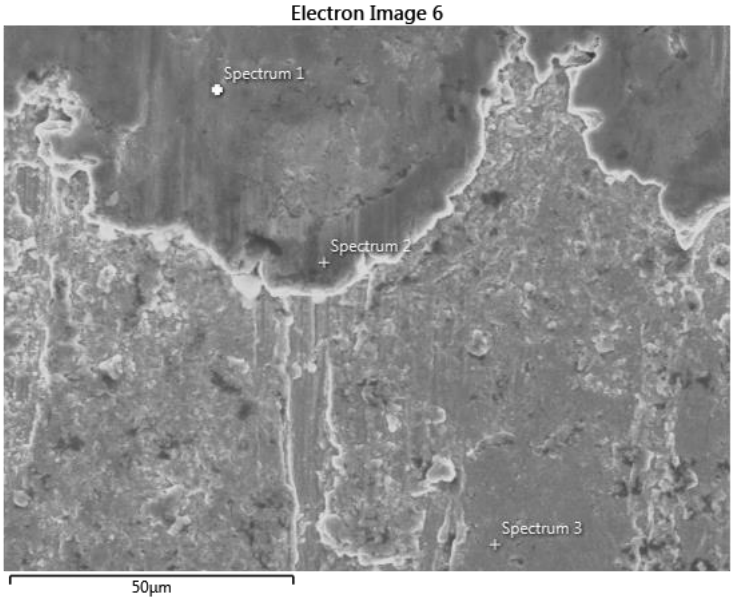

Figure 4-5 SEM picture of top view within wear scar on plate specimen of 700◦C test. Spot 1: glaze layer center, Spot 2: glaze layer edge, spot 3: Outside of glaze layer.

Table 4-1 Point EDX results showing chemical composition in weight percentage of spot 1, 2 and 3 and static oxide (oxide formed outside of the wear scar).

location	Fe wt%	Cr wt%	Ni wt%	O wt%	Si wt%	Mn wt %
spot1	44.9 ± 0.3	13.4 ± 0.2	8.4 ± 0.2	30.2 ± 0.3	0.2 ± 0.1	2.8 ± 0.2
spot2	42.5 ± 0.3	20.5 ± 0.2	6.3 ± 0.2	30.4 ± 0.3	0.3 ± 0.1	/
spot3	48.9 ± 0.3	21.9 ± 0.2	17 ± 0.3	10.7 ± 0.2	1.5 ± 0.1	/
Static oxide	40.2 ± 0.1	19.5 ± 0.1	14.0 ± 0.1	25.1 ± 0.1	0.5 ± 0.1	0.8± 0.1

A plate sample tested at 600°C was cross-sectioned to investigate the chemical composition and thickness of the glaze layer formed. The results are presented in Figure 4-6. As shown in Figure 4-6 (a) and (b), an oxygen-rich layer was observed on top of the wear scar with variable thickness ranging from 6 to 20 μm. The line scan from the surface into the depth in Figure 4-6(b) shows the peaks in count per second (cps) for Fe is associated with O, but the peak of Cr is associated with a valley in O, suggesting that iron oxide may be a more preferable type of oxide for glaze layer comparing to chromium oxide, which is consistent with reported observations [39]. Overall this characterization further confirms that glaze layer is oxygen rich.

To summarize, in the temperature-baseline test series conducted at 10Hz, the severe-to-mild wear transition has been observed in the 310S/310S cylinder-on-flat test configuration. The friction and wear results show high repeatability. The temperature influence on wear loss for pin and plate are similar. The severe-to-mild transition took place between 200°C to 300°C, and the tests conducted in the transition temperature also show a drop in μ_E at some point with increasing cycle count. The characterization of worn surfaces suggest that the development glaze layer is the reason of the severe-to-mild wear

transition. Similar to the glaze layer found in other material system, the glaze layer formed in the 310S/310S interface contains sufficiently high oxygen composition compared to other locations either within the wear scar or outside of the wear scar which is statically oxidized during the test.

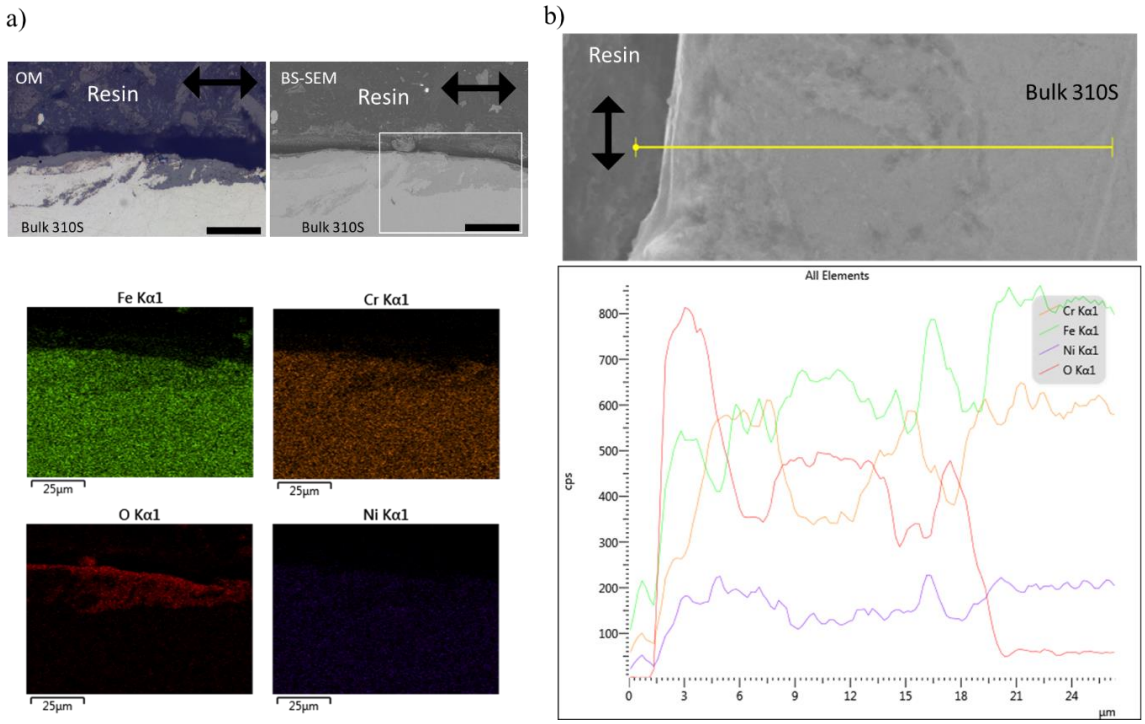

Figure 4-6 Cross-section view of plate sample after 600C 10Hz tests showing the glaze layer structure, the reciprocating direction is noted by double headed arrows: a) OM, BS-SEM and EDX element mapping of glaze cross-section, scale bar = 25μm; b) EDX line scan of major elements' distribution along the depth of wear scar

4.3 Quantification of E-COF evolution with sigmoid fitting

As discussed in the previous section, the formation of the glaze layer is associated with the μ_E drop that occurs during cycling, and the minimum test duration to observe this drop is temperature dependent. This result is consistent with the critical cycle N_{GL} theory that

suggests a critical number of cycle is needed to activate the glaze layer formation [36]. According to this theory, no further wear will accrue after the fretting cycle reaches N_{GL}, and N_{GL} is depends on both testing condition and the material properties (chemical composition, diffusivity, etc.).

To build the linkage between the μ_E drop and N_{GL} model, it is essential to describe the μ_E drop in a robust and quantitative way. Here we propose to fit the cycle count (N) vs. μ_E to a sigmoid function. Such function has been used to describe the running-in coefficient of friction evolution [97], but not the entire coefficient of friction evolution.

A sigmoid function is commonly used to describe a symmetric and bounded S-shape curve (or so called sigmoid curve). The formula of a general sigmoid function is given as:

$$\frac{y-d}{c} = \frac{1}{1+exp(\frac{x-b}{a})} \tag{4-1}$$

where a, b, c and d are four fitting parameters that control the shape and location of the curve: a and c denote the scaling along x and y axis, while b and d represent the translation of the curve along x and y axis. A special case of sigmoid curve when a=-1, c =1, b = d =0 is called logistic function and is shown in Figure 4-7 (a).

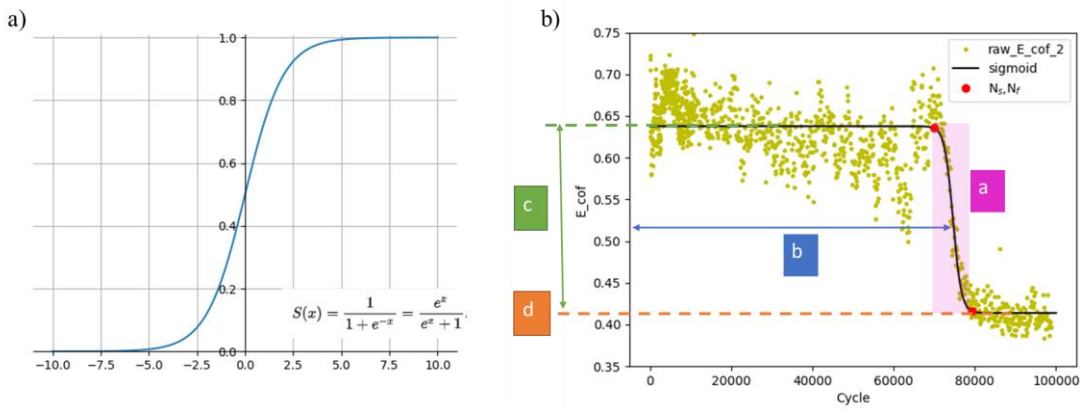

Figure 4-7 Schematic of sigmoid function and the fitting parameters' determination on the shape and location of the curve: (a): simplified sigmoid curve, (b) demonstration of sigmoid fitting with 250°C_100K test result and illustration of the tribological meaning of the fitting parameters.

An example of using Eq. (4-1)to represent the evolution of μ_E is illustrated in Figure 4-7(b). By taking the limit of Eq. (4-1), one can get:

$$\mu_{E\,max} \approx \lim_{x\to-\infty} y = c + d \tag{4-2}$$

$$\mu_{E\,min} \approx \lim_{x\to+\infty} y = d \tag{4-3}$$

The μ_E value before and after the drop does not appear to depend on temperature, but instead depends only the number of cycles that needs to be applied before the drop occurs. It is clear that μ_{Emax} represents the high-level value of μ_E that is the typical steady-state μ_E for severe-wear mechanism domain, $\bar{\mu}_{E\_non-glaze}$, while μ_{Emin} represents the low-level value of μ_E that is associated with glaze layer protection in the mild-wear domain, $\bar{\mu}_{E\_glaze}$. Therefore, c represents the total amount of μ_E drop due to glaze layer formation, and d as the steady-state value of μ_E when the glaze layer is fully developed, i.e.,

$$c = \bar{\mu}_{E\_non-glaze} - \bar{\mu}_{E\_glaze} \quad (4\text{-}4)$$

$$d = \bar{\mu}_{E\_glaze} \quad (4\text{-}5)$$

The rate of μ_E drop is described by *a* and *b*. The symbol *a* represent the "stair width", with a smaller the value of *a* indicating a more rapid transition. The symbol *b* represents the cycle of the inflection point of the curve.

If the starting turning point of the μ_E drop (N_s) is defined by the cycle when 1% of the μ_E drop is reached (i.e., y = d + 0.99 c), and the finishing drop (N_f) as the cycle when 99% of the drop is finished (i.e., y = d + 0.01 c), one can easily estimate N_s and N_f

$$N_s = b - a * \ln(99) \approx b - 4.595a \quad (4\text{-}6)$$

$$N_f = b + a * \ln(99) \approx b + 4.595a \quad (4\text{-}7)$$

As such, the duration of μ_E drop, N_d can be quantified as:

$$N_d = N_f - N_s \approx 9.2a \quad (4\text{-}8)$$

The sigmoid fitting of the μ_E data is automated with Python 3 and Scipy library using non-linear least square fitting method. As demonstrated in Figure 4-7(b), this method fits the result very well, and can provide consistent and robust N_f identification compared to eyeballing using the data only. Compared to other potential fitting methods such as fitting the μ_E data with three straight lines, sigmoid fitting has many advantages: (1) the sigmoid function is continuous, differentiable, script friendly (thus, the result is robust and

repeatable), (2) the rate change of μ_E with the reduction in friction is captured, and most importantly, (3) the fitting parameters have tribological meanings that provide insights for in depth research in parametric studies of wear performance.

Since N_{GL} has been defined as the critical cycle for glaze layer formation, it can be experimentally defined as the cycle at which drop of μ_E is complete [98]. To this end, the obtained N_f is treated as N_{GL} equivalent in this work.

4.4 Univariable frequency-baseline test

The frequency-baseline tests were conducted at 1Hz, 5Hz, 10Hz, 50Hz and 100Hz at room temperature. Since there is no power input from the furnace for those tests, any temperature rise captured by the thermocouple attached on the plate will be fretting-induced only. In such way, the temperature rise as a function of frequency can be estimated.

Figure 4-8(a) presents the μ_E evolution with cycles for the frequency baseline, with the sub plot on the lower right showing that the final hysteresis loop for each test overlaps. The averaged μ_E beyond 40K cycles is defined as the steady-state E-COF ($\bar{\mu}_E$) shown in Figure 4-8(b) together with the net wear volume rate. For all frequencies except 100Hz, the μ_E evolution curves are well aligned with a mild trend to progress to a slightly higher μ_E in the later stage of the test. No significant μ_E drop was observed within the given cycle (66K), and all the $\bar{\mu}_E$ falls in the range of 0.77±0.05. This relatively high μ_E suggests that all tests at this condition are located in the severe wear mechanism zone on the wear map. The steady-state hysteresis loops for all test frequencies have similar shape and sliding amplitude, δ^*, which suggests that the power of dissipative energy is nearly the same for

all tests. The unstable μ_E observed for the 100Hz test was mostly caused by its large noise in hysteresis loop, as discussed in Section 3.3. For this specific test, the DN55 testing rig also failed to maintain a stable control and stopped automatically at around 50K cycles before the test sequence was finished. To make the 100Hz wear data comparable to the rest of the tests with 66K cycles, all wear results in this section were normalized by total cycle. Even though the stability of that test was not good, the net wear rate, average friction, and increase in temperature tended to follow the trends observed at lower frequencies.

The net wear volume loss $\dot{V}^{net}$, shown in Figure 4-8(b), slightly decreases from 1Hz to 10Hz, and then slightly increases with further increasing of frequency. This $\dot{V}^{net}$ variation, however, is less than the standard deviation of $\dot{V}^{net}$ for 10Hz room temperature tests in temperature-baseline($\pm 0.011 mm^3 N^{-1} mm^{-1}$, as shown in Figure 4-2(a)), and thus considered as not significant.

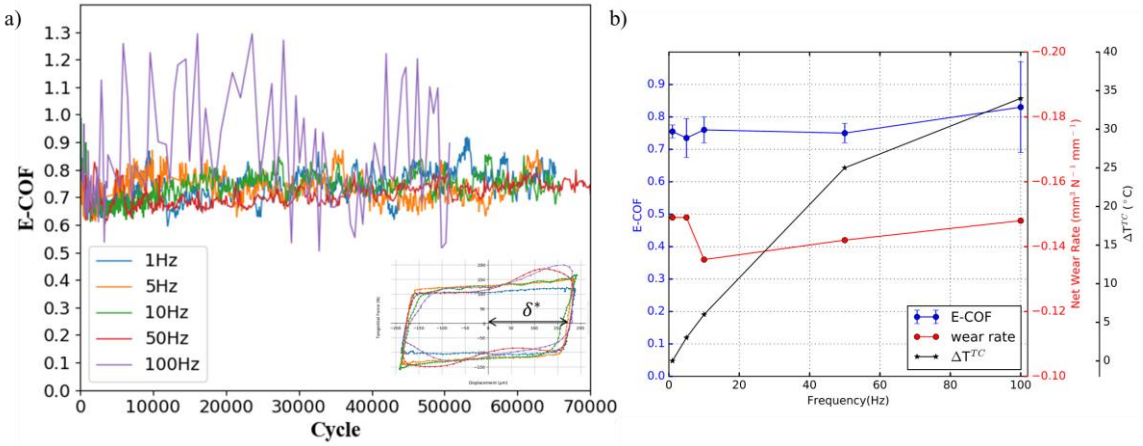

Figure 4-8 Influence of frequency of cycling at room temperature: a) μ_E evaluation with cycle at each frequency, sub figure in a) shows the hysteresis loops near the end of the test. b)Frequency-E-COF-wear rate plot overlapped with temperature rise captured by the thermocouple.

During the wear test, the sample surface temperature was captured by a type-K thermocouple (TC) that was spot welded about 4-5mm away from the central line of the wear scar as shown in Figure 3-1 (a). The real time sample temperature at the thermocouple location, T^{TC}, for each testing frequency is shown in Figure 4-9 (a). While T^{TC} for the 1Hz test was almost unchanged during the entire wear test, a noticeable temperature rise is detected for tests conducted at higher frequencies, particularly, 50Hz and 100Hz. The total temperature rise throughout a complete test, ΔT^{TC}, is given by

$$\Delta T^{TC} = T_f^{TC} - T_i^{TC} \tag{4-9}$$

where T_i^{TC} is the T^{TC} captured at beginning of the test, and T_f^{TC} is the T^{TC} captured upon finishing the test. Demonstration of calculating ΔT^{TC} for 50Hz is illustrated in Figure 4-9(a), and ΔT^{TC} for each frequency at room temperature is summarized in Figure 4-8(b). In general, ΔT^{TC} linear correlates to frequency, noting that ΔT_{100Hz}^{TC} deviated from linearity likely due to its reduced number of cycles (50K) compared to the other tests (66K cycles). To estimate ΔT_{100Hz}^{TC} for 66K cycles, the temperature rise rate, which is defined as the temperature rise per second, is calculated by:

$$\Delta \dot{T}^{TC} = \frac{\Delta T^{TC}}{\frac{N_{tot}}{f}} = \frac{\Delta T^{TC} * f}{N_{tot}} \tag{4-10}$$

where N_{tot} is the total number of cycle and f the test frequency. $\Delta \dot{T}^{TC}$ for each frequency is shown in Figure 4-9(b), which correlates well with a second order polynomial. This result suggests that if all tests were conducted for the same number of cycles, a linear relationship between ΔT^{TC} and frequency is expected, and ΔT_{100Hz}^{TC} for 100Hz is calculated

to be 50°C if the test was conducted to 66K cycles. This observation agrees with the temperature rise model in Eq (2-4) that Jin and Shipway proposed and validated for the 304/304 austenitic stainless steel cylinder-on-flat fretting system [57]. A more detailed comparison between their test conditions and ours is given in Table 4-2.

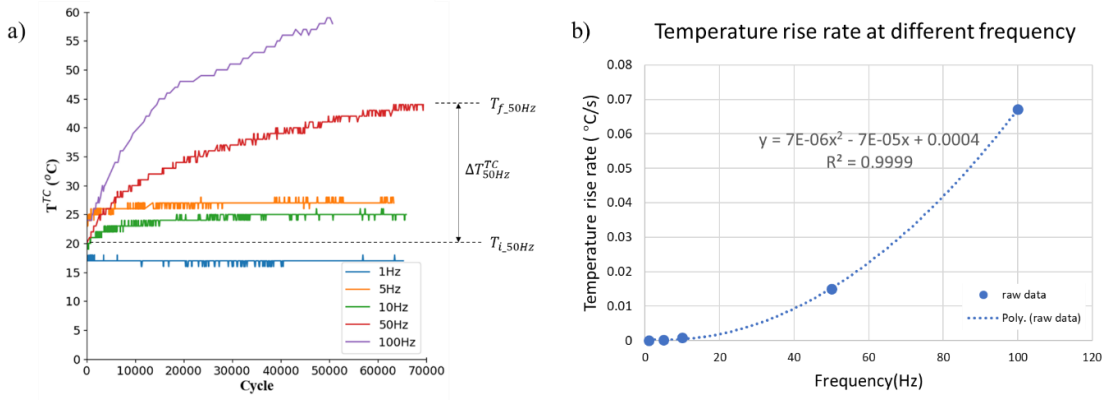

Figure 4-9 Fretting induced temperature rise as a function of frequency: a) Evolution of temperature measured at thermocouple location over the cycles of the test for each frequency. b) The temperature rise rate at each frequency and the second order polynomial fitting result.

Table 4-2 Comparison of material and test conditions between Jin and Shipway [57] and current work

Data source	Jin and Shipway	Our test (baseline)
Material	304 stainless steel (like on like)	310S stainless steel (like-on-like)
Contact mode and configuration	Cylinder on flat	Cylinder on flat
Normal force (N)	450	150
Contact length (mm)	10	13
RT Hertzian contact pressure p0	0.51GPa	0.20GPa

RT Hertzian contact size b	56.0 um	36.6 um
Displacement amplitude (um)	(+/-)50	(+/-)200
RT yield strength	0.215 GPa	0.205 GPa
Frequency(Hz)	20 and 200	1,5,10,50,100
Steady state E-COF	0.61	0.77(RT)
Thermal conductivity(W/mK)	14	11
Total cycle	100K	66K

To estimate the temperature rise at the middle line of contact interface (x' = 0), Eq. (2-4) is simplified as below:

$$\Delta T(0,0) \sim \frac{b p_0 \delta \mu_E f}{\kappa} \tag{19}$$

where b is the half-width of Hertzian line contact, p_0 the maximum Hertzian contact pressure, δ the displacement amplitude, μ_E the E-COF that was assumed constant, f the frequency, κ the thermal conductivity. As the simulation result shown in Figure 2-7 suggests, the majority of temperature rise in the contact itself happens within 10 s of the start of the test, and the rising rate gradually decays and becomes much less sensitive to the testing time and cycle. By substitution of the parameters listed in Table 4-2, a scale factor of 1.65 can be calculated, i.e. the temperature rise at contact line is our case is 1.65 times higher than that of Jin and Shipway's test at the same frequency. Based on Jin and Shipway's result, the increase in temperature rise due to dissipation of frictional power for 200Hz is about 90°C. With this information as well as the fact that the frequency-baseline

tests share very similar μ_E, it is then inferred that the fretting induced (or dissipation-energy induced) temperature rise for the 100Hz test at the center of the contact in the current work is about 74°C, and the temperature rise for the rest of the frequencies are proportionally smaller. The estimated ΔT at the center of the contact of all frequencies involved in frequency baseline tests are summarized in Table 4-3. The estimated temperature rise at the thermocouple location (approximately 5mm away from the center of the contact) was calculated assuming 71% of the temperature rise was maintained. As shown in Table 4-3, the temperature estimation was very close to the real measurement data, suggesting the calculated temperature rise at the center of the contact is a reasonable estimation. Thus, in the future tests, the temperature rise at the contact can be estimated by $\Delta T^{TC}/71\%$ (i.e. $1.41* \Delta T^{TC}$)

Table 4-3 Estimated fretting induced temperature rise at center of contact and at thermocouple location for frequency-baseline tests, comparing to the temperature rise measured by thermocouple.

Frequency (Hz)	Estimated ΔT at x' = 0 (°C)	Estimated ΔT at x' = 5mm (°C)	measured ΔT^{TC} (°C)
1	1.9E-03	1.3E-03	0
5	0.2	0.1	3
10	4	3	6
50	37	26	25
100	74	53	50*

The results in Table 4-3 also bring insights on the design of experiments for later tests. Since 50Hz is the highest stable working frequency for the DN55 at the current load and amplitude, tests conducted at 50Hz will experience most significant temperature rise influence. If we assume the temperature rise induced at 50 Hz oscillation frequency shifts the temperature-dependent severe-to-mild wear transition by simply adding the temperature rise to the environmental temperature, a temperature grid finer than 37°C

around the transition zone is necessary to observe this shift. It should be noted that the estimation in Table 4-3 assumes a constant μ_E for the entire testing period. While this assumption is valid for the frequency baseline tests, a lower μ_E and thus lower dissipative energy is expected at high environmental temperature as indicated in temperature-baseline test series. The oxide third bodies that have much lower thermal conductivity will prevent heat transformation at the interface and lead to higher ΔT at the interface[57] under constant μ_E assumption.

To summarize, for the frequency-baseline test series conducted at room temperature, μ_E and net wear loss rate did not vary much with increasing of frequency. For wear at room temperature, the wear mechanism is severe-wear mechanism and the test frequency, within the range of frequencies tested, does not change the wear mechanism. The surface temperature rise at 4-5mm away from the center of the contact is measured by thermocouple, and this temperature rise is linearly correlated to frequency, and has been used to validate the temperature rise estimation. Based on those results, frequencies of 1Hz and 50Hz are selected as the minimum and maximum frequencies for future tests and the wear map for best performance of the testing rig. A 37°C temperature rise is expected in 50Hz test before oxide formation as well as μ_E drop at higher temperature. Temperature grids finer than 37°C are needed around the transition zone to investigate temperature rise induced shift in wear mechanism that may affect a boundary on a wear mechanism map.

4.5 Temperature-frequency coupling effect in wear performance

With the knowledge learnt in initial probing of the wear map with two baseline tests, a systematic parametric study on the synergic effect between environmental temperature (T^E)

and frequency (*f*) on the wear performance was conducted following the DOE described in Figure 4-1(b). Firstly, a course grid test matrix was implemented consisting of the intersection of T^E = 200/400/600°C and f = 1/5/10/50Hz. The test results indicate that severe-to-mild wear transition occurs in the temperature range of 200 to 400℃ for all the four frequencies. A finer grid was then applied to this temperature range to further identify the transition boundary between 200 and 300℃. The $\bar{\mu}_E$ results of all the tests as well as their NWR are summarized in Figure 4-10. Similar to the temperature-baseline test results, the $\bar{\mu}_E$ transitions happened at slightly higher temperatures compared to the NWR transitions. One explanation is that NWR considers the volume worn in the complete testing process while $\bar{\mu}_E$ considers average value over the last 20K cycles.

For all frequencies, when T^E<200°C, the $\bar{\mu}_E$ is high while when T^E>300°C, the $\bar{\mu}_E$ is low with a transition occurring in between. While 1Hz, 5Hz and 10Hz tests share a similar high-level and low-level $\bar{\mu}_E$, the 50Hz tests showed a higher $\bar{\mu}_E$ (and thus higher friction force) at all temperatures compared to other frequencies. Characterization of the worn surfaces suggests that the high steady-state friction may result from an adhesive wear mechanism that usually leads to more severe friction and wear. The height map as well as optical image of the wear scar for 50Hz, 400°C is shown in Figure 4-11, where a matched shape of peak-valley was observed at corresponding location of the plate-pin pair that was in contact. It is possible that an adhesive wear mechanism is prompted by the high temperature rise induced at this frequency and the high compatibility of the like-on-like materials in the tribo couple, resulting in a significant amount of material transfer between bodies. It should be noted that in the NWR calculation, such material transfer from pin to

plate is canceled out. Additional cross-sectional characterizations of the pin and plate samples are needed to confirm this hypothesis.

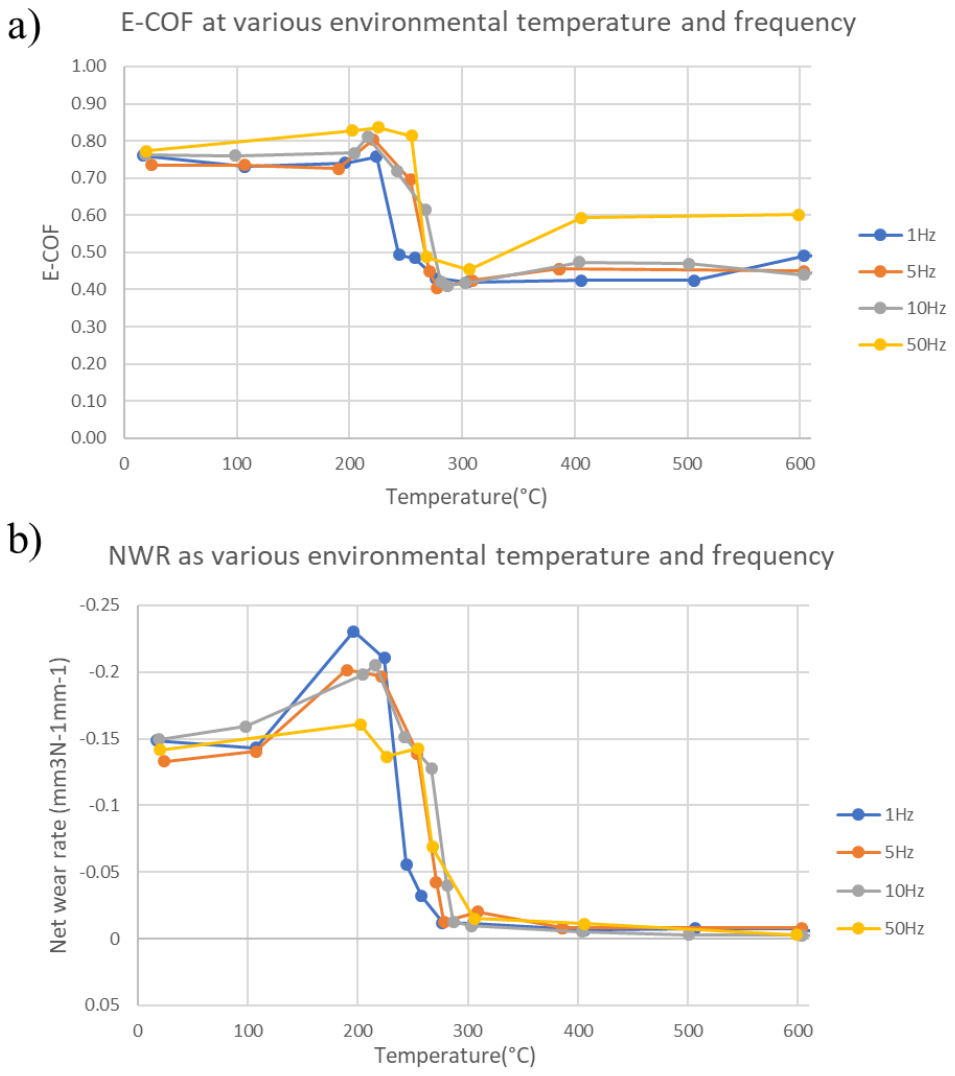

Figure 4-10 NWR and steady-state E-COF of 310S/310S at various environmental temperature and frequency

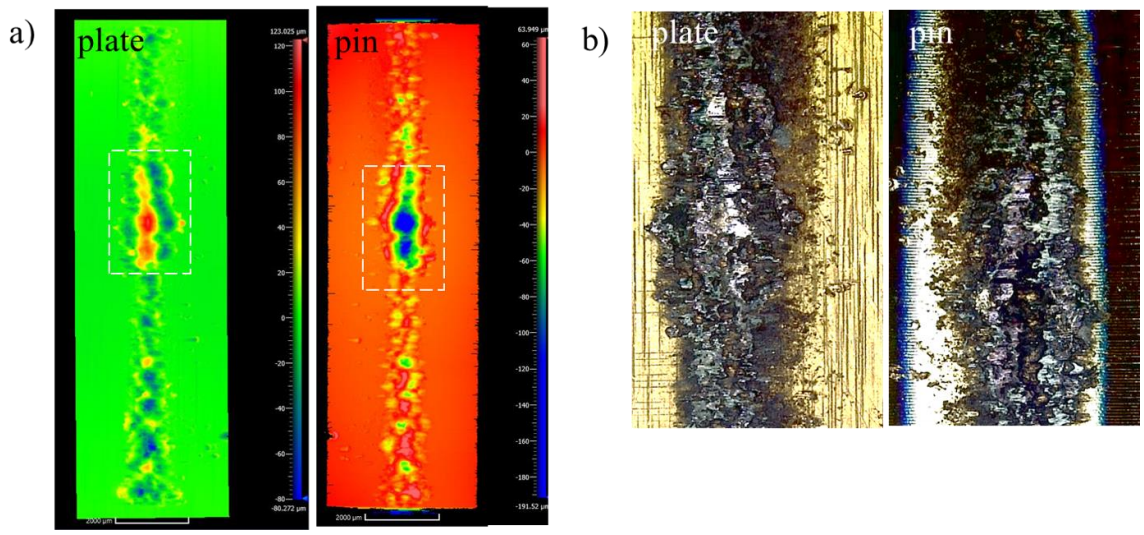

Figure 4-11 a) Zygo height map of pin and plate after tested at 50Hz, 400°C; b) OM image of the area selected in white block of Zygo height map for pin and plate in a)

The $\bar{\mu}_E$ results for various environmental temperatures and frequencies shown in Figure 4-10(a) are utilized to generate a temperature-frequency $\bar{\mu}_E$ map as shown in Figure 4-12(a). This map and later NWR map were generated by 2D data interpolation with OriginLab2019b. In this map, red represents a high $\bar{\mu}_E$ and blue represents a low $\bar{\mu}_E$. If we define severe wear as $\bar{\mu}_E$>0.7 and mild wear as $\bar{\mu}_E$ < 0.5, the wear map can be divided into 4 zones: A as high friction zone, C as low friction zone , and B,D the two moderate friction zone as transition. The boundaries are more clearly illustrated by expanding the map near transition region as shown in Figure 4-12 (b). As discussed before, the transition zone B is caused by formation of glaze layer during the test duration, and the transition zone D is likely to be resulted from enhanced adhesive wear at high frequency. This $\bar{\mu}_E$ map also suggests that with a further increase of frequency, high friction zone (or high μ_E) may re-occur at higher temperatures beyond 400°C.

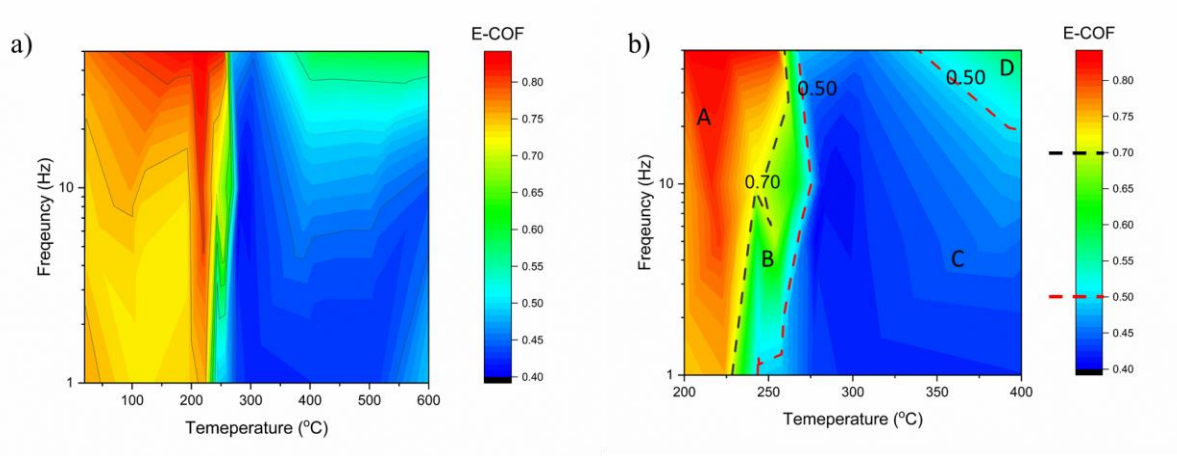

Figure 4-12 Steady-state E-COF map of 310S/310S cylinder-on-flat fretting system: a) complete map; b) map focused on the 200°C to 400°C temperature regime with $\bar{\mu}_E$ < 0.5 and $\bar{\mu}_E$ > 0.7 used to define the boundaries between A, B, C and D zone, respectively.

Similar to $\bar{\mu}_E$, the NWR decreases from 200°C to 300°C at all four frequencies tested. The portion of Figure 4-10 (a) that covers this temperature range is enlarged and presented in Figure 4-13(a). From 1Hz to 10Hz, the NWR shifts to right (i.e., higher temperatures). Since higher temperatures promote faster glaze layer formation kinetics, those shifts suggest that increasing the frequency may be detrimental for glaze layer formation or retention. This detrimental effect may come from the two aspect. Firstly, the interpass time between asperities at the interface per cycle is shorter, and thus increases the number of cycles needed to achieve a certain sintering time to form the glaze layer. Moreover, the higher frequency may inhibit the gathering and retention of oxides or oxidized debris that is essential for glaze layer formation. However, this negative effect gradually attenuates with increasing of frequency, and eventually reverses this trend at 50Hz. It is hypothesized that the detrimental effect of frequency has been gradually overcame by its beneficial effect, increasing the temperature rise at the contact interface. To estimate the temperature-rise effect, the same NWR data were re-plotted with the average temperature near the interface

measured by a thermocouple that was spot welded near the contact area, T^{TC}. The results are presented in Figure 4-13(b). While the T^{TC} is expected to be lower than the real contact temperature, it can be treated as a temperature rise indicator, as high temperature rise at contact surface can lead to high T^{TC}, assuming same thermal conductivity properties of the contact interfaces. In general, T^{TC} is higher than environmental temperature at various degrees, with larger temperature difference at higher frequency, which is expected from the temperature rise calculation in the frequency-baseline section. On the other hand, the shift of T^{TC} at each frequency to achieve the same NWR, ΔT^f , is roughly proportional to the reciprocal of the frequency, which supports the previous discussion that the detrimental effect of frequency in the severe-to-mild wear transition comes from its influence of time (either interpass time per cycle or total time).

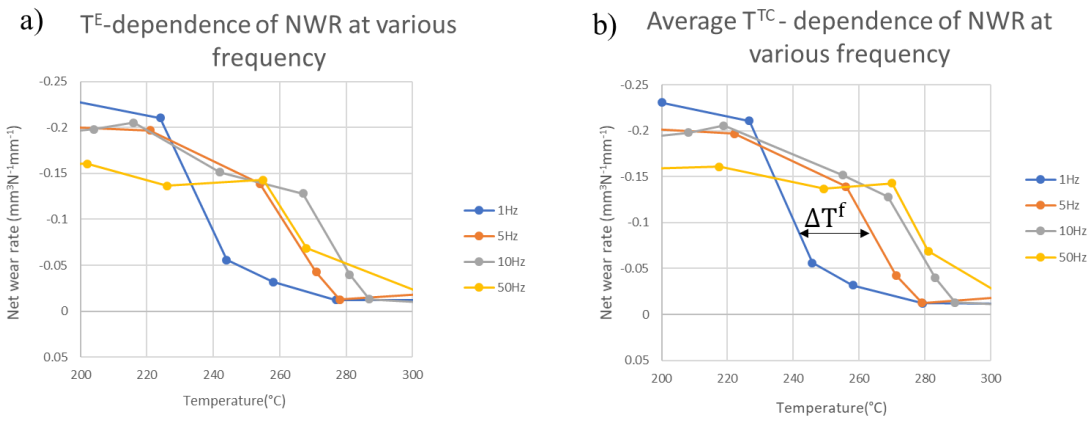

Figure 4-13 a) Environmental temperature-dependence of NWR at various frequency; b) average thermocouple temperature dependence of NWR at various temperature.

Moreover, the frequency-dependence of the NWR is also related to temperature. In Figure 4-14, the same transition zone data reported in Figure 4-13(a) are reorganized to show the frequency's influence on NWR at various temperature. The data points fall in the same

temperature category has ±5°C variance in the temperature due to the nature of the temperature control of our furnace. However, the environmental temperature variation during each test is very stable with variance less than ±1°C. In general, the NWR decreases with increase of temperature as a result of glaze layer formation. At 200°C and 225°C, increasing of frequency leads to a reduction in NWR. This temperature is considered close to the starting temperature of the transition zone in severe-to-mild wear transition for all frequencies. A similar trend has been reported in several other material system and test configurations at low temperatures where abrasive wear is the dominant wear mechanism [58–60]. It has been argued that increasing frequency will reduce the interpass time per cycle, which reduces the time that oxygen can interact with the wear debris and form oxidized debris that are usually harder than the substrate [60,99]. At 250°C, however, increasing test frequency from 1Hz to 10Hz increases NWR by three times, and then NWR slightly decreases with increase of frequency from 10Hz to 50Hz. The trend of increasing NWR with increasing of frequency from 1Hz to 10Hz is also observed at 270°C, but a more significant drop in NWR is achieved when increasing frequency from 10Hz to 50Hz. At 300°C, the influence of frequency to NWR is minimal and the NWRs for all frequencies are all close to zero, suggesting that they all fall in the mild wear glaze layer protection region on the wear map. Based on the previous discussion on the temperature rise at the contact during the test, fretting-induced temperature rise for frequencies lower than 10Hz for the current set-up is lower than 5°C, and thus the change of trend from 200°C to 300°C in the 1-10Hz frequency range is more likely to be associated to a change of glaze layer formation kinetics that is governed by temperature. This result suggests that the frequency-dependence of NWR is temperature dependent.

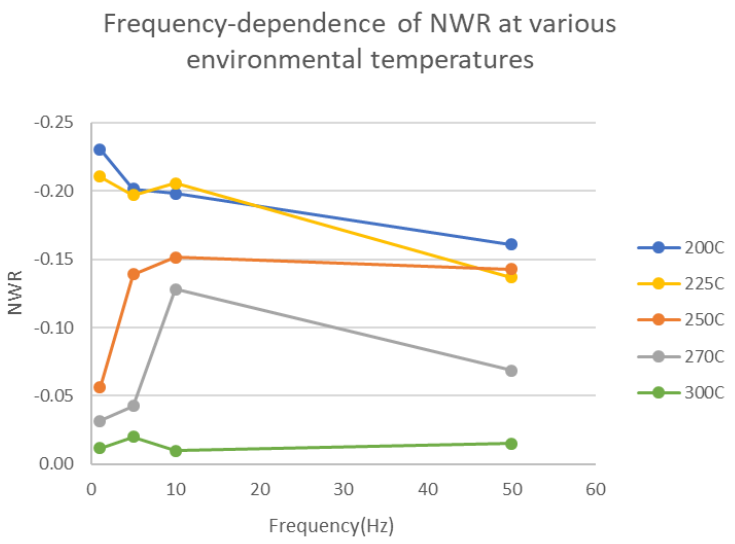

Figure 4-14 Frequency-dependence of NWR at various environmental temperature.

The net wear rate (NWR) is plotted in a wear map format in Figure 4-15(a), which presents the temperature-frequency wear map generated for 310S/310S cylinder-on-flat fretting system. In this map, the NWR is scaled from red to blue, where red represents the high wear rate that is associated with severe wear, and blue represents the low wear rate that is associated with mild wear. Contour lines representing 80% and 20% of the maximum NWR, specifically, $-0.17 mm^3N^{-1}mm^{-1}$ and $-0.02\ mm^3N^{-1}mm^{-1}$, respectively, are highlighted to denote the severe and mild wear regions on the map. It worth noting that those two highlighted contours are not equivalent to wear mechanism boundaries seen in Figure 4-2 (a). In the baseline-temperature tests (Figure 4-2 (a)) as well as other research work on severe-to-mild wear transition[36,98], the starting temperature of the transition zone is defined by the maximum NWR, and thus the boundary where wear mechanism changes from severe wear to transition zone should be a curve that connects conditions when the local maximum NWR is achieved. This definition is convenient because the relationship between the determinant factor (temperature, frequency, etc.) and NWR is

monotonic in each of the zones. In our case, the maximum NWR for all frequencies were captured at around 200°C, which makes the boundary that separates severe wear and severe-to-mild wear transition zone a straight line at T = 200°C. Resolution improvement for this boundary is needed; however, it will still lie in the 80% maximum NWR contour: NWR = $0.17 mm^3 N^{-1} mm^{-1}$.

Comparing to the data representation shown in Figure 4-13 and Figure 4-14, the contours in the wear map illustrate the conditions where the coupling effect between environmental temperature and frequency in correlating to the NWR occur. Any non-vertical and non-horizontal contour on the map suggests that NWR is determined by both factors, and the migration of the curvature change of the contours during migration from high NWR to low NWR can suggest different roles of temperature and frequency in severe wear and mild wear. To study the coupling effect between the environmental temperature (T^E) and frequency (*f*), special attention has been given to the transition zone that occurs between 200°C and 300°C where most of the curvature change in contour occurs and hence largest coupling effect. The enlarged wear map in this temperature range is presented in Figure 4-15(b).

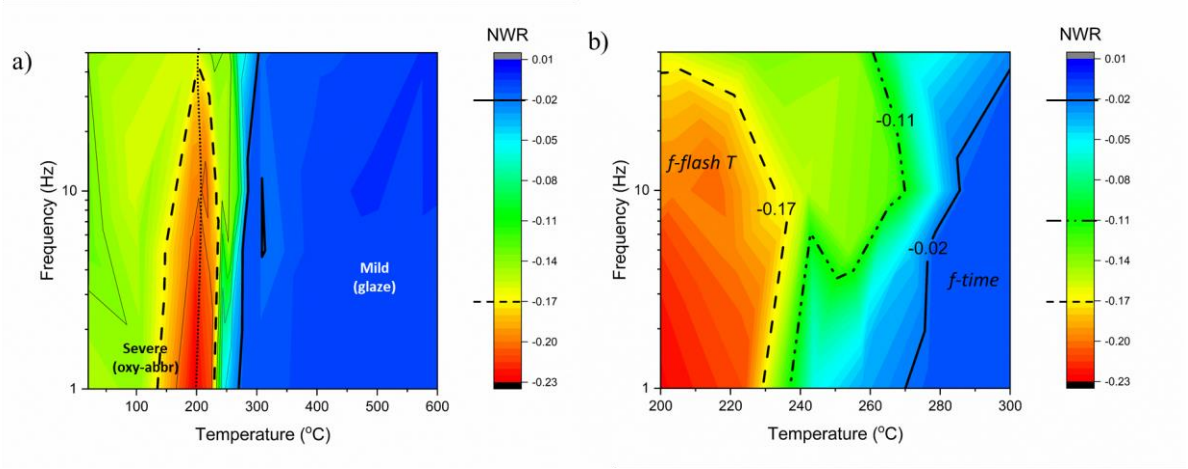

Figure 4-15 Wear map of 310S/310S at cylinder-on-flat configuration: a) complete map; b) details of the map near the transition zone: 200°C-300°C that show different mode of synergic effect between environmental temperature and frequency

In the transition zone presented in Figure 4-15(b), with increasing of frequency, the high NWR contour, NWR = -0.17$mm^3N^{-1}mm^{-1}$, curves to the left. This observation suggests that at the initial stage of the severe-to-mild wear transition (i.e., when NWR is still relatively high), the wear performance for high *f* and low T^E is equivalent to that of low *f* and high T^E. It makes sense because high *f* is associated with high fretting-induced temperature rise at the contact surface, which can compensate the low environmental temperature and make up a similar contact temperature comparing to the case for low *f*, high T^E. As such, this contour suggests that the initial stage of severe-to-mild wear transition, NWR is determined by the temperature at the contact surface.

On the contrary, the low NWR contour, NWR = -0.02$mm^3N^{-1}mm^{-1}$, that goes from (1Hz, 270°C) to (50Hz, 300°C) curves to the right. Since NWR further to the right of this contour is minimal due to rapid glaze layer formation in the early cycles, and the higher T^E in this temperature range promotes glaze layer formation, it can be inferred that increasing frequency is unfavorable in wear control and prevent the finishing of the severe-to-mild

wear transition. One possible explanation is that a certain period of time (either time per cycle or total fretting time) is necessary to fully sinter the oxide/oxidized debris to form the glaze layer. Increasing of frequency reduces the interpass time per cycle, which will be detrimental for the growth of the glaze layer. Another possible explanation is that high frequency may promote the motion of third body debris[35,60], which prevents the stability of embryonic glaze layer from further development. It could then be inferred that at the final stage of severe-to-mild wear transition (i.e., NWR has dropped to near its low value), NWR is governed by the development of glaze layer or its stability.

These observations and discussions also bring more insights in understanding the T^E-f coupling effect in wear performance determination. Clearly, the two effects that high frequency promotes: (1) high contact surface temperature and (2) short interpass time per cycle, can co-exist and compete with each other. However, their influence in wear can be amplified by T^E: when T^E is not sufficiently high, the additional temperature rise is critical for the system to overcome energy barrier to initiate glaze layer formation. At higher T^E, it is instead the stability of the glaze layer (or its embryonic structures) that determines the NWR. To this end, the coupling effect between T^E and f may essentially be the competition of the frequency's beneficial/detrimental effect in wear determination. Depending on the stage of the severe-to-mild wear transition, either the beneficial effect or detrimental effect of frequency will be more significant, and the stage of severe-to-mild wear transition is dominantly controlled by T^E.

4.6 N_{GL} model correlations

The test results that fall in the severe-to-mild wear transition zone on the wear map are further analyzed to calibrate the N_{GL} model. With sigmoid fitting method, the N_{GL} for each testing condition is defined as the cycle at which 99% of the μ_E drop is reached. The identified N_{GL} and its associated testing conditions, T^E and f, are used to determine the parameters of the N_{GL} model: the sintering parameter S_{GL} and oxidation activation energy E_a. To perform this analysis, the original N_{GL} model in Eq. (2-2) is rewritten as:

$$\ln(N_{GL}/f) = A + B * \left(\frac{1}{T}\right) \tag{4-9}$$

where $A = \exp\left(\frac{S_{GL}}{\delta^{*2}}\right) and\ B = \left(\frac{E_a}{R}\right)$, δ^* is the sliding amplitude and R is the Boltzmann constant. Both A and B are assumed to be constant, as the sliding amplitude δ^* measured from hysteresis loop of for the transition zone tests are very close to each other (less than 5% difference), and both S_{GL} and E_a are assumed to be invariant and only depend on the materials of the two bodies in contact.

Figure 4-16(a) presents the fit of Eq. (4-9) to the data with environmental temperature, T^E, used as T. While data for each frequency all appear to align linearly, there is clearly a shift between each frequency. The correlation to Eq. (4-9) is much improved by taking the temperature rise during the test into consideration with $T = T^E + 1.41*\Delta T^{TC}$ as shown in Figure 4-16(b). With this correction of the temperature, the R^2 value improved from 0.8042 to 0.9629, suggesting that the average contact temperature should be used in the N_{GL} model. The importance of considering the average contact temperature was not specified in the original N_{GL} model, though it is possible that for their testing conditions, the temperature rise was not large enough to bring in a quantifiable influence to the correlation of the model.

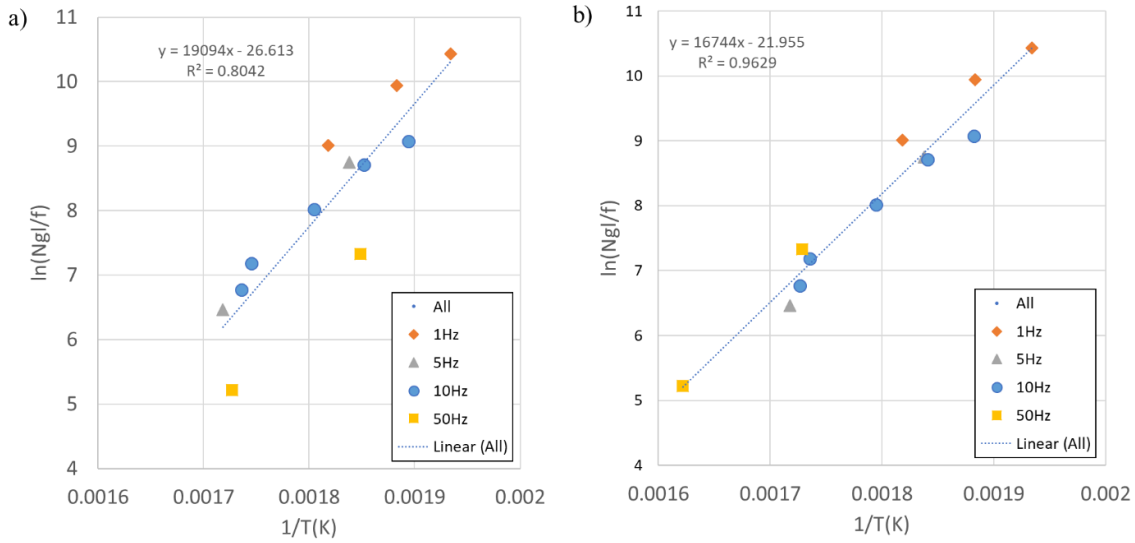

Figure 4-16 a) Correlation of the N_{GL} model using environmental temperature; b) Correlation of N_{GL} model considering temperature rise at the interface

The parameters *A* and *B* determined from the fit using T^E, Figure 4-16 (b), are used to determine S_{GL} and E_a for our system. The sintering parameter S_{GL} is calculated to be $1.05 \times 10^{-11} mm^2/s$, which is six magnitudes smaller than the S_{GL} for the Co-Cr alloy system ($9.5 \times 10^{-5} mm^2/s$) reported in reference [36]. While a lower S_{GL} is expected in our case because Fe is a more favorable element to form a glaze layer then Co and Cr [39], this huge difference needs further investigation. The activation energy E_a is calculated to be 139 kJ/mol. This result is consistent with the activation energy found in the literature for static oxidation of most metals which is generally higher than 100 kJ/mol[100]; however, it is higher than the Co-Cr alloy system reported in reference [36], which is 37 kJ/mol, and it is also reported elsewhere that the oxidation activation energy for stainless steel during sliding can decrease significantly compared to the static oxidation (19.1 vs 160

kJ/mol)[101]. The limited results reported in the literature make it difficult to form any clear conclusions at this time.

The N_{GL} model assumes that the wear only occurs before N_{GL} cycle is reached. To this end, it may be possible to estimate the boundaries of severe-to-mild wear transition using the N_{GL} model, shown in Figure 4-17:

- Boundary 1 (B1) is the temperature-frequency contour that represents $N_{GL} \geq N_{total} = 66K$. Locations to the left of this boundary will result in no μ_E drop and thus no sufficiently formed glaze layer by the end of the cycling. This boundary may represent the beginning of the severe-to-mild wear transition.
- Boundary 2 (B2) is the temperature-frequency contour that represents $N_{GL} \leq 0.1 * N_{tot} = 6.6K$. The temperature-frequency combination that locates to the right of this boundary will have a considerably small N_{GL} comparing to N_{tot}. At these conditions, μ_E will drop at a very early stage of the test, and the glaze layer will pseudo-instantaneously form at the contact interface which results in negligible material loss. This boundary may represent the completion of the severe-to-mild wear transition.

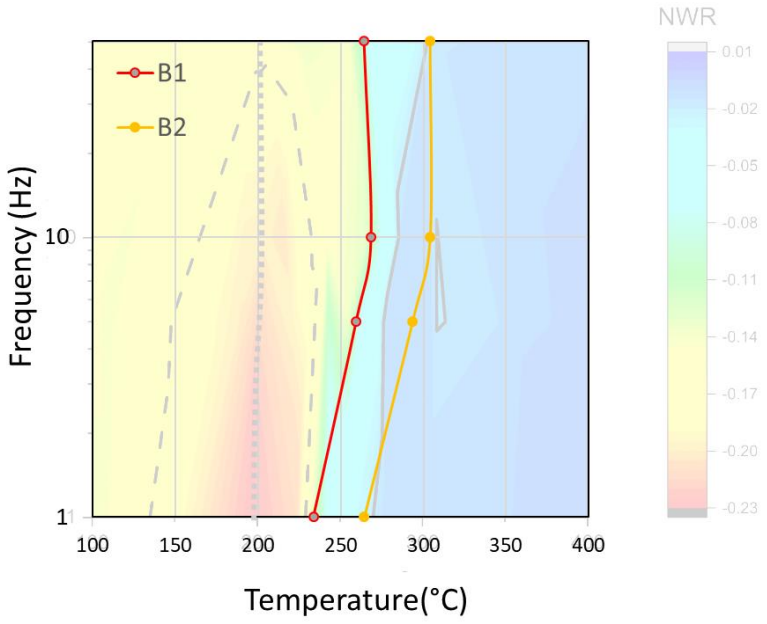

Figure 4-17 Overlapping of severe-to-mild wear transition boundaries predicted by N_{GL} model with the obtained wear map

Since N_{GL} model considers the contact surface temperature instead of T^E, the fretting-induced temperature rise (estimated by $1.65\Delta T^{TC}$ at room temperature) has been subtracted in the presented B1 and B2 to be consistent with the experimental-based wear map which is based on T^E. The location of the B1 and B2 boundary falls in the severe-to-mild wear transition zone that was experimentally obtained. More specifically, the B2 boundary is closely aligned with the mild wear boundary (NWR = -0.02 $mm^3N^{-1}mm^{-1}$ contour), confirming that the fast formation of the glaze layer at initial stage of the test is the major mechanism that governs mild wear. The vertical deviation between B2 and mild wear boundary at 5Hz and 10Hz may come from underestimation on the temperature-rise in contact during N_{GL} model implementation. The B1 boundary, on the other hand, did not exactly capture the beginning of the severe-to-mild wear transition (neither T = 200°C line nor NWR = -0.17 $mm^3N^{-1}mm^{-1}$ contour). Instead, it falls near the NWR = -0.11 mm^3N^-

$^{1}mm^{-1}$ contour where a rapid drop of NWR occurs. This result suggests that the NWR drop in the severe-to-mild transition zone occurs before complete glaze layer formation occurs. It is possible that a compacted debris bed or embryonic glaze layer is sufficient to reduce the net volume loss. In another words, the glaze layer formation marks the rapid NWR drop in severe-to-mild wear transition, although this transition can be initiated by pre-glaze layer structures. This understanding also explains asynchronous drop for $\bar{\mu}_E$ and NWR over temperature observed in Figure 4-2(a) and Figure 4-10.

4.7 Strategy of constructing and utilizing a wear mechanism map

Indeed, successful construction of an informatic and applicable wear-mechanism map is not a trivial task. The key elements and challenges that need to be considered when constructing a wear map includes:

1) **Reasonable amount of trustable experimental results with sufficiently large range and reasonably close spacing of independent variables.** A high-quality data set with clear and repeatable experimental results is critical to construct a rigorous wear map. While many of the fretting conditions and environmental conditions are continuous, it is impossible to conduct an infinite number of tests. To cover all possible wear mechanisms in the desired range of conditions and achieve acceptable resolution of wear mechanism boundaries with reasonable number of discrete data points, a sophisticated design of experimental methodology is essential and extremely important.
2) **Consistency in mechanisms and their boundary determination.** This requires a suitable choice of wear performance indicator, and a complete characterization of

the characteristic features (morphology, chemical composition, etc.) in each wear mechanism zone for identification and prediction purpose. Lack of analytical or physics-based models to describe the wear mechanism boundaries will result in a phenomenological map only, which can have some good insights but not quantifiable and thus less appealing to be used for wear prediction.

3) **Probed and clearly stated scope and limitation.** While one map is generated in one case with specific equipment, material system and contact configuration, it is always beneficial to probe possibilities of extending the wear map to other cases, or trace the shifts or reshaping in wear map when tuning variables that were kept constant in the current wear map.

The process of constructing a 310S/310S wear map demonstrated in this chapter has been a practice to fulfill the first two key elements with the best effort: For Element 1, we developed a hierarchical probing DOE that helps to quickly capture the key trends and wear mechanisms that cover a large range of temperatures and frequencies, and generated a high quality tribological database for 310S/310S that has high repeatability. In addition to the experimental effort, we also showed that the N_{GL} model has potential to further minimize the number of tests needed. For Element 2, we have standardized the N_{GL} cycle recognition using the μ_E evolution plot with sigmoid fitting and clearly defined the wear map boundaries by both NWR contours in the wear map and N_{GL} model.

For industrial applications, the wear map generated with 310S/310S can assist both in materials selection and making test plans for materials screening. For example, if one wants to know the temperature that leads to the worst and the best μ_E or NWR of 310S/310S with

other testing conditions kept the same, the test conditions should be selected in the severe-wear and mild-wear zone, respectively. At 10Hz or below, the worst wear performance is expected at about 200°C, and best wear performance is expected at temperature above 300°C. With more knowledge gained through chemical composition influence in the boundary determination of the wear map, the wear performance of a new material candidates may be evaluated using 310S as a reference. If glaze layer has been observed at the contact interface for a specific material candidate at high temperature, the temperature that leads to the severe wear (i.e. bad wear performance) and mild wear (i.e. good wear performance) of the candidate material by a calibrated N_{GL} model: test at locations on the left of B1 boundary to estimate the worst performance, and at location right to the B2 boundary to estimate the best wear performance. Conducting tests in the different wear regimes will help to identify where the boundaries between these regimes are located.

Other wear maps, including wear maps with the same material but different independent variables (displacement amplitude, normal force, etc.), and wear maps with different material couples, can be generated following the methodology described in this chapter. A comparison between those maps and how the boundaries shift will provide insights on the synergic effect between different testing conditions as well as the material's property-dependent wear mechanism change. The stability of the boundaries obtained in a wear map should also be probed by a dynamic testing set-up that cyclically switch between conditions that leads to different wear mechanisms, which is an important consideration for applications where the working condition. For example, one could explore the wear response under conditions representing the severe wear regime (i.e., low environmental temperature) after the material couple previously operated in the mild wear regime (i.e., a

stable glaze layer has been formed). Such an effort would be beneficial to correlate the wear map, which is generated by tests with fixed test parameters, to the real application of the material, where a dynamic change in working conditions (i.e., changes in temperature, frequency, displacement amplitude, loading, etc.) is often involved.

4.8 Conclusions

1. A severe-to-mild wear transition has been observed in the 310S/310S cylinder-on-flat fretting system, and glaze layer formation is the primary reason for the transition.
2. A complete strategy of efficiently generating a wear map is proposed and applied to generate a temperature-frequency wear map for the 310S/310S cylinder-on-flat fretting system. This map clearly shows the temperature and frequency dependence in the severe-to-mild wear transition. Overall, the environmental temperature plays the dominant role in wear performance determination, and the role of frequency is significant in the severe-to-mild wear transition. In the transition zone, a coupled effect between environmental temperature and frequency has been observed and associated with the local increase in temperature from a fretting-induced surface temperature rise, i.e., Coulomb heating, during wear observed when the frequency is high.
3. The critical cycle for glaze layer formation, N_{GL}, can be experimentally obtained by fitting the μ_E evolution data with a sigmoid function. The fretting-induced surface temperature rise should be considered to correctly fit the wear data to the N_{GL} model. A calibrated N_{GL} model can be adopted to estimate the boundaries in the severe-to-mild wear transition in wear map.

4. Wear maps are powerful tools to visualize wear performance and wear mechanism transitions with change of testing conditions. It has great potentials for guiding materials selection for industry applications.

CHAPTER 5. CHARACTERIZATION OF GLAZE LAYER USING COMPUTER VISION ALGORITHMS

5.1 Introduction

As presented in previous chapter and reported in many other works [21,28–30,36], it has been widely recognized that the development of a glaze layer is the key reason for the severe-to-mild wear transition for Fe-, Cr, and Ni-based alloy with increasing temperature. To this end, it is critical to understand the nature of the glaze layer to understand its role in friction and wear reduction, and make it possible to use this understanding to motivate future mechanical design of wear resistant interfaces.

Since the measured coefficient of friction and wear volume depend on the entire surface in contact, knowing the glaze layer distribution within the wear scar is important. The coverage of glaze layer within the contact area needs to be sufficient to achieve the severe-to-mild transition. In fact, it has been reported that small patches of glaze layer are present before the severe-to-mild transition finishes [54].

Studying the distribution of the glaze layer within wear scar is indeed a challenging task, because the surface height profile itself does not incorporate the chemical or mechanical property information that could be used to distinguish the glaze layer. One solution is to bring in other characterization techniques that are capable to identify the glaze layer. Success of this strategy requests both high−quality alignment and precise identification of glaze layer and its boundary.

The prior requirement can be easily fulfilled if the multiple spectrums are collected by one characterization tool, as such the signals are by nature perfectly aligned. In 1997, Jiang et al. [102] built an adapted 3-dimensional contact profiler that measures contact resistance between the sample surface and the metal stylus simultaneously during scanning of surface profile. Because the glaze layer has high concentration of oxide and thus high electrical resistance, the glaze layer region can be recognized by its high electrical resistance. By comparing the glaze layer coverage to the tribological test results at various temperatures, the authors found that the critical projected coverage of glaze layer upon finishing of severe-to-mild wear transition is less than 50%, and the glaze layer formation is preferable in the central area of the wear scar. However, the resolution of this set up (about 130μm) is too low to precisely detect boundary of glaze layer. Like most contact mode surface profilers, this method has a physical limitation on the resolution by the tip size and the density of the scanning trace mesh. In addition, it is challenging for this method to differentiate between non-glaze oxide layer (i.e., static oxide layer) formed at extreme temperatures and the glaze layer itself. Therefore, this work did not lead to meaningful conclusion for height distribution of glaze layer.

In fact, the second requirement of precisely identifying the glaze layer and its boundary is not a trivial task. In much of the literature, the glaze layer identification is purely based on a descriptive criteria such as “shiny, smooth, highly oxidized, compacted, superficial layer” as defined when the concept was first coined [24]. Because quantitative description of glaze layer is missing, glaze layer identification for most studies [25,26,28,35,75,103,104] have been purely qualitative. This limitation further leads to the difficulty of effectively defining the boundary of the glaze layer. It is not a big issue for local probing type of research that

only examine a small portion within glaze layer under high magnification observation, but it matters when it comes to large scale statistical analysis on glaze layer, for example, the distribution of glaze layer.

Herein, we aim to address the challenge of studying the distribution of glaze layer with a novel strategy that meets both alignment and resolution requirements. For alignment, instead of seeking equipment that can do-it-all, we take advantages of several individual characterization tools, each of which captures some aspect of glaze layer's characteristics, and align the resulting images from each tool by computer vision principles. With help of Vickers hardness indentation markers as fiducial points, good alignment has been achieved with sub-pixel error. This methodology can be used to integrate as many surface mapping spectrums as necessary (e.g., optical microscopy (OM), scanning electron microscopy (SEM), 3D optical profilers, nano-hardness map, etc.). For precise glaze layer identification, we proposed a novel quantitative criterion based on OM images of wear scars with a specific lighting mode. Optical microscopy is a rapid, easily accessible and cost-effective equipment for worn surface characterization. It can achieve high resolution in large range of magnification, which makes it feasible to characterize wear scars from a wide variety of contact configuration and test conditions. The proposed criteria are tested and validated by comparing to SEM images.

This chapter will start with introducing basic computer vision concepts used in this work that may be unfamiliar to the wear community. Section 5.3 will briefly review the temperature-base line test in Section 4.2, which we used to further characterize in this work. In Section 5.4, the role and specific settings of three characterization tools, namely, OM, SEM, and optical profilometer, will be described. Their resulting images are aligned for

integration of the information and glaze layer identification. After glaze layer regions are segmented, the distribution of glaze layer within wear scar as a function of environmental temperature is discussed in two perspectives: projected glaze coverage from top-view, and height variation of glaze layer from vertical perspective. The results provide evidences that the glaze layer is facilitated at relative high location within wear scar, which decreases friction and wear by reducing the real contact area during fretting/reciprocating sliding.

5.2 Background in computer vision

5.2.1 Homography transition

A homography transformation describes the geometric relation between two individual 2D images of the same planar object [105]. It is a common technique used in the field of computer vision. Considering two images that are taken by two different cameras of one planar object, a point on image 1 with coordinate (x_1, y_1) and a point on image 2 (x_2, y_2) that correspond to the same physical point of the planar object must have the following relation:

$$\begin{bmatrix} x_1 \\ y_1 \\ 1 \end{bmatrix} = H_t \begin{bmatrix} x_2 \\ y_2 \\ 1 \end{bmatrix} \tag{5-1}$$

where H_t is a 3 by 3 matrix that defines the homography transformation. Although H_t has 9 elements in total, it has only 8 degrees of freedom to enforce the constraint that the third element of the resulted vector is always 1. Given the property that a homography transformation has 8 degrees of freedom, we can compute the homography transformation between an image pair with a minimal four pairs of known (x_1, y_1) and (x_2, y_2) that

correspond to the four physical points, i.e., fiducial points, on the same plane [105]. More pairs of fiducial points are desired to reduce stocastic error when calculating the H_t matrix. In such over-constrained situation where more than four pairs of matched points are provided, an optimal solution of H_t can be calculated with least square method.

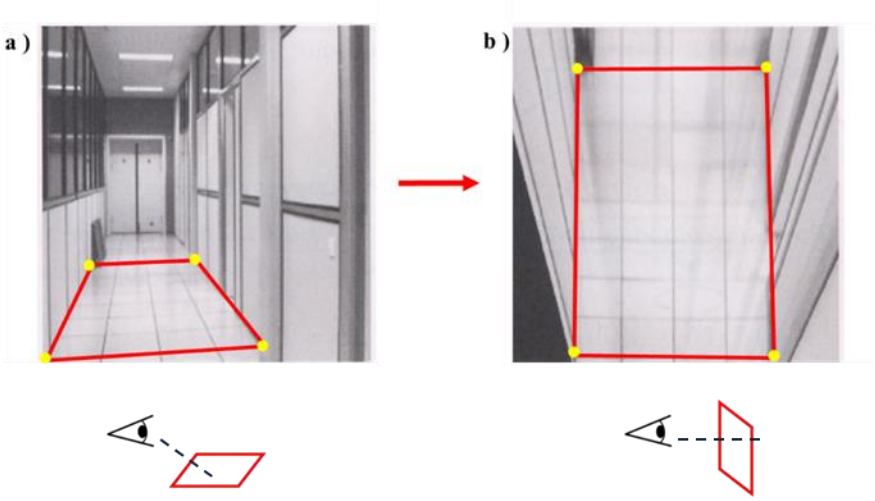

Figure 5-1 A pair of corridor floor image with different perspective from reference[105]**: a) view perspective is about parallel to the floor tile; b) view perspective is perpendicular to the floor tile. The two images are related via homography transformation, and the four highlighted corners of a floor tile set can be used to compute the homography**

Figure 5-1[105] presents an example of homography transformation. The ground plane, represented by the highlighted rectangular, distorted due to different perspective of view. A homography transformation representing the distortion can be computed using the four point-pairs marked for the same physical locations as highlighted corner points.

Once the homography matrix H_t is calculated, it can be used to find any corresponding point from one image to another, and the image 2 can be transformed to image 2' that is aligned with the reference image, image 1.

5.2.2 HSV colour space and its separation

HSV (Hue, Saturation, Value) is an alternative representation of more commonly used RGB (Red, Green Blue) color space. It describes all colors in a cylindrical geometry: Hue (H) is the angular dimensions, representing the true color in a circle (0°- red, 120°- green, 240°- blue and 360° back to red); Saturation (S) is the distance to the central vertical axis, and it represents the amount of color presented in percentage of pure color (full saturation); Value (V) is the central vertical axis that corresponds to the intensity scaling, or brightness. Both V and S are in the interval [0,1]. H is in the interval [0°, 360°][106]. An example of an image after HSV separation can be founded in Figure 5-2.

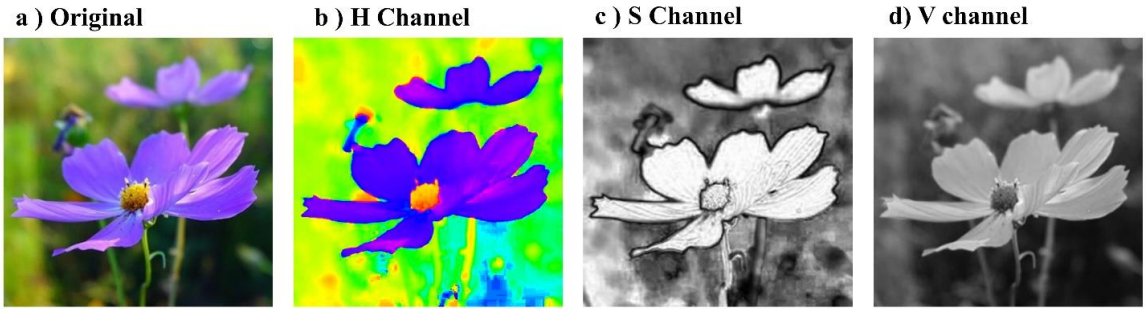

Figure 5-2 Example of conducting HSV color space separation for a photograph of flowers: a) Original image; b) H channel; c) S channel; d) V channel. H channel are colored to better illustrate the color(S=V=1).

5.3 Methodology

5.3.1 Dataset preparation

The characterization data set were collected with the temperature-baseline tests presented in Section 4.2. Specifically, Samples after 250°C, 280°C, 300°C, 400°C, 500°C, 600°C, and 700°C fretting test were used to study the differences in the glaze layer characteristics

with temperature. After the tests, loose debris were cleaned in alcohol using an ultrasonic bath. For each pair of pins and plates, a 2.5mm section was randomly selected along the total 13mm contact length of the wear scar. Fiducial markers were made with a Vickers hardness tester (Mitutoyo HM-200, Tokyo, Japan). The fiducial markers were placed in an unworn area near the selected section of wear scar on plates, and they were used as reference for the homography transformation to align images acquired from different methods. To achieve the preferred marker size (50-100μm in diagonal for current set up), 0.5-1kgf load was chosen based on hardness of the samples. Redundant markers were applied for convenience of later point matching steps. To minimize error of H_t calculation, it is ideal to spread markers over the four corners of the rectangular view of aligned image.

5.3.1.1 Optical microscope (OM) images

Optical microscope images were taken with Leica DVM6 (Wetzlar, Germany) in Z-stack mode that overlap focused images with height variance. 20% intensity of Coaxial illumination (CXI) and 10% intensity of Ring Lightning (RL) mode were used together for lightening at full aperture to highlight glaze layer and its boundaries in OM images. Schematics of the different lighting modes and their resulting OM images of the same wear scar can be found in Figure 5-3. Among the two lighting sources, CXI is the more critical one providing a strong, concentrated and vertical incident light. As shown in Figure 5-3(b), the glaze layer will stand out with strong reflection due to its flat and smooth surface morphology. At the same time, the boundary of the glaze layer patches will be clearly outlined. The RL lighting mode, on the other hand, involves a ring of lighting source and the incident light is slightly divergent. As a common lighting mode that is available in most OM equipment, RL mode by itself (Figure 5-3(a)) doesn't highlight glaze layer as good as

CXI. However, the additional RL light to the CXI mode (Figure 5-3(c)) can help to enhance the reflectiveness of the wear trace on glaze layer, and thus improve the accuracy of glaze layer detection. The circled area in Figure 5-3(b) and Figure 5-3(c) serves as a demonstration of such improvement.

All OM images used in this work were taken at the same white balance, lighting intensity and saturation so that any color and brightness difference between images are only caused by the surface characteristics of the wear scar, not the OM settings.

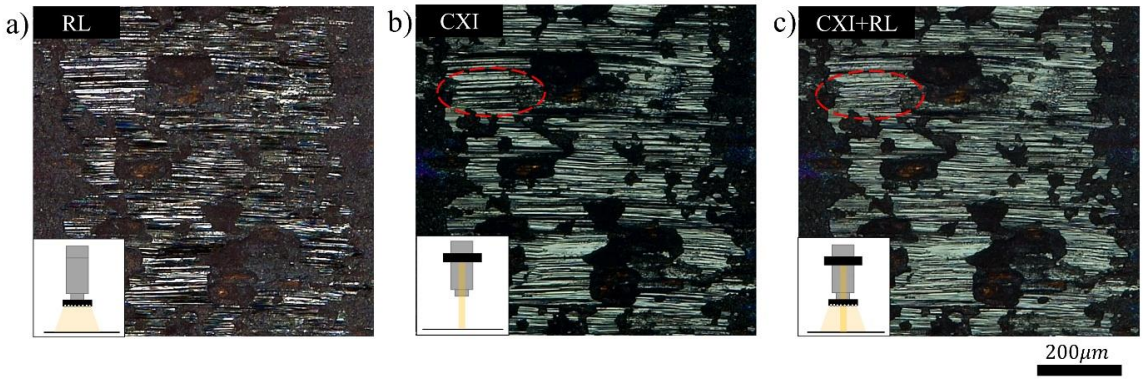

Figure 5-3 Schematic of different lighting mode and their resulting OM image at the same view of wear scar after 500°C test: a) with ring lighting (RL) mode, 60% intensity; b) with coaxial illumination (CXI) mode, 20% intensity; c) with combined CXI (20% intensity) and RL lighting mode(10% intensity). The three OM images share the same scale bar

5.3.1.2 SEM images

SEM images were acquired using the Hitachi SU-8230 (Tokyo, Japan) with cold field emission gun in either secondary electron (SE) or backscatter electron (BSE) modes using 20KeV and 20mA. The SE signal is sensitive to surface morphology, where darker regions represent smooth surfaces. In contrast the BSE signal highlights the elemental component information, where features with lighter elements appear darker in the BSE images. Since

the glaze layer is a smooth and highly oxidized layer, it is expected to appear dark in both SE and BSE images.

5.3.1.3 Height maps

The optical profilometer used in this work, Zygo Zegage 3D optical profilometer (Middlefield, CT, USA), is a non-contact surface profiler based on the principle of two-beam interferometry [107]. The output of the optical profilometer is a height map of the surface profile scanned. Since 10X lens and 1X zoom was the only option available with our instrument, stitching mode (20% overlap) was used to cover a 3486μm X 2882μm rectangular area for all specimens. This rectangular area covers a selected region of wear scar, fiducial markers, and part of the surrounding unworn surface on both sides of the wear scar in the reciprocating direction. Using the Zygo software Mx (version 7.5.0.1), the average height of unworn surface is defined as the reference (i.e., denoted as zero height) to correct the tilt of the specimen and/or the scanning platform, and the scan voids are filled by data interpolation. The lateral resolution (defined as the minimal distinguishable height difference between neighboring camera pixels) of the Zygo is 0.815μm.

5.3.2 Image alignment workflow

The general idea of image alignment is to calculate a ground truth homography transformation matrix H_t, and then apply this matrix H_t to align an image with the reference image. This process is achieved using a home-built Python script with OpenCV library. As an illustrative example, OM-height map alignment for a plate tested at 280°C is used to demonstrate the workflow. The original height map and OM image is shown in

Figure 5-4(a) and (b), respectively. The height map is colored by assigning overall maximum height in red and minimum height in blue of the scanned area.

Before starting the process, the reference image is selected. In this work, the height map is chosen as reference image and therefore, the OM image is aligned to the height map. This arrangement is made for two reasons: Firstly, it can unify magnification of all OM images. The magnification of the profilometer is fixed, while the OM images could be acquired at various magnifications to compensate for width variations in the wear scar to achieve the best resolution. Secondly, the height map is a tilt-corrected image using the software of the optical profiler. Consequently, using the height maps as alignment reference can correct all OM images to the same tilt removed perspective.

The first step of image alignment is to calculate the H_t matrix. For this purpose, more than 8 pairs of fiducial points, i.e., the center of Vickers indentation scars, were matched between the two images, Figure 5-4(a) and Figure 5-4(b). To improve labeling accuracy of this step, the pre-selected areas in the height map and OM image that contain each pair of indentation scars are magnified, and the pre-selected area of the height map is temporarily re-colored to enhance image contrast to assist in center identification of the indentation scars. Figure 5-4(c) and (d) demonstrate one pair of such magnified area of the original height map and the OM image as the dashed blocks marked in Figure 5-4(a) and (b). The center of the red crosses is the labeled fiducial point that represent the center of the same indentation scar.

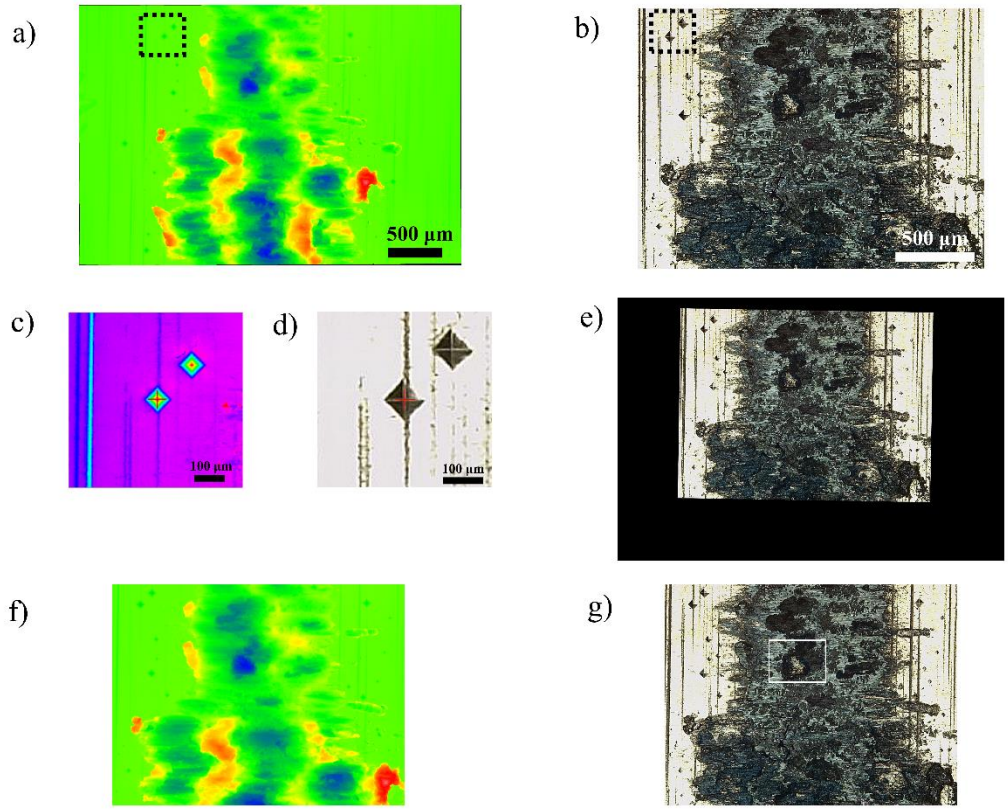

Figure 5-4 Outcome images of image alignment workflow demonstrated with images of 280C plate: (a) Original height map; (b) Original OM; (c) magnified and recolored marker area in height map; d) magnified marker area in OM; (e) aligned OM image; (f) final height map; (g) final aligned OM . (a) and (e)-(g) share the same scale bar. The region selected by white frame in (g) is used for validation of glaze layer identification criteria in Section 5.4.2

Among the eight matched points pairs, the majority (6 or more pairs) were used to calculate a tentative homography transformation matrix H_i, while the remaining pairs are used to estimate the error of this H_i matrix. If the error is less than 1 pixel, this H_i matrix is finalized as the ground truth matrix H_t; otherwise, the manual matching process is repeated until sub-pixel error is obtained.

Afterwards, the H_t matrix is applied to the OM image to align it with the height map. After alignment, the aligned OM image and the height map share a same dimension and same

pixel resolution (up to 0.73μm). In this example and many other cases where the magnification of the original OM image is higher than that of the height map, a compensated blank area will appear at the edges of the aligned OM image (e.g., Figure 5-4(e)). A subsequent edge trimming is applied to the aligned images to remove the blank areas. The final output height map and OM image pair is shown in Figure 5-4(f) and Figure 5-4(g).

5.4 Quantitative H-V criterion for glaze layer identification

5.4.1 Glaze layer identification with H-V criterion

In this work, we proposed a new and quantitative criterion, called the H-V criterion, to segment the glaze layer portion from the general wear scar area in an OM image. Using this criterion, we can identify glaze layer with the fewest sample preparation steps and a single tool, optical microscope.

An example of this glaze layer identification workflow in given in Figure 5-5. As discussed earlier, the glaze layer and its boundaries can be highlighted by CXI lighting mode with high brightness due to its smooth surface morphology. The glaze layer portion always appears a blue-green color under our optical microscope. The color characteristics were found to be independent of test temperature, which will be discussed later in the results section. Furthermore, the brightness and color information can be extracted from an image using its Value (V) and Hue (H) channels, respectively, after conducting the HSV separation. Therefore, the two characteristics of a glaze layer, color and brightness (or reflectiveness) under optical microscope observation, can be quantitatively translated to two requirements to form the H-V criterion:

H-requirement: its color should fall in a hue range from H_{min} to H_{max};

V-requirement: its brightness should be no smaller than a minimum V value, V_{min}.

A pixel i with (H_i, V_i) hue and value is labeled as glaze layer only if both H and V requirements are met, i.e.

$$\begin{cases} H_{max} \geq H_i \geq H_{min} \\ V_i \geq V_{min} \end{cases} \tag{5-2}$$

The three parameters: V_{min}, H_{min} and H_{max} are adjusted to correctly label the glaze layer that has been recognized during SEM observation for calibration. Additional discussion of turning these parameters using SEM image as a reference can be found in Section 5.4.2. In this specific example, the values of these parameters are: V_{min} = 0.35, H_{min} = 56, H_{max} = 169. The filtered result for H or V requirement is a binary mask, called the H mask or V mask. Every pixel that meets the criteria, Eq. (5-2), is labeled as '1', or white, in the binary mask image; otherwise, the pixel is '0' or black. Boolean intersection operation is then applied to the H and V mask image to find the locations where pixels meet both requirements, and those pixels are labeled as glaze layer. The binary image made up by the glaze layer pixels are called a raw glaze layer mask. In practice, wear traces on top of glaze layer that are parallel to the sliding direction can be misjudged as "non-glaze layer" using this algorithm due to its low reflectiveness. This error is reduced by adding a small portion of RL lightning to enhance the reflectiveness, and by applying opening/closing operation [108] to fill the remaining uncaptured traces on glaze layer. As the final output, the output glaze layer mask is saved.

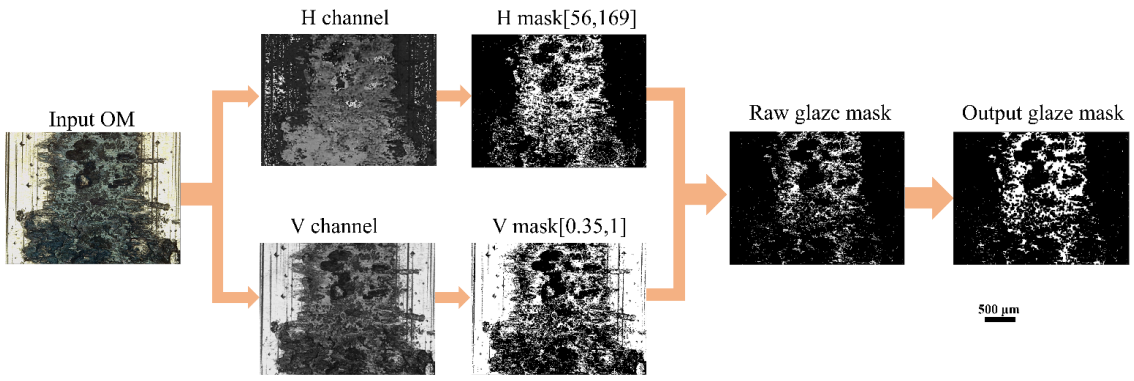

Figure 5-5 Glaze layer identification workflow for an OM image acquired from a plate that experienced fretting at 280°C. All images share the same scale bar

Since no spatial transformation was applied in this workflow, the input and output image (and all other intermediate images) are by nature of the same dimension and perfectly aligned with each other. Furthermore, if the input OM image has been pre-aligned with its pairing height map, the resulting binary mask will be aligned with the height map as well. This way the height information of wear scar is fused with the glaze layer mask, which enables statistical analysis of height distribution on the glaze layer and non-glaze layer individually.

5.4.2 Application and evaluation of H-V criterion

To verify the feasibility of proposed H-V criterion and get its optimized parameters H_{min}, H_{max}, V_{min}, SE and BSE SEM images were used to compare with the glaze layer identification obtained from the OM image. As an example, Figure 5-6 demonstrates the validation process for the plate tested at 280°C. Due to the limitation of the minimum magnification of our SEM, a small portion of the wear area was used for the validation. To have an intuitive judgment on the accuracy of glaze layer identification, the SE SEM image is overlaid with the glaze layer identified from the OM image (shadowed in red) in Figure

5-6 (g). This overlay is achieved by aligning the OM image to the SE SEM image (Figure 5-6(f)) following the workflow introduced in Section 5.3.2, and applying the H-V criterion on the aligned OM image (Figure 5-6(a)). The only difference is that there is no Vickers indentation fiducial mark within the field of observation. In this special case, local characteristics, such as small islands, sharp corners, etc., are chosen as fiducial points for alignment. The identified glaze layer portion, highlighted in red in Figure 5-6(g), shows good agreement with the glaze layer confirmed by the SEM image, and confirmed that H-V criterion worked very well in precisely identifying glaze layer and its boundary.

In this example, we also noticed a special area, identified as "shiny spot" in the view of observation. As indicated in the V-channel image of OM (Figure 5-6(b)), this area has high brightness, and the brightness of its center is even higher than that of a general glaze layer. However, the shiny spot area is judged as non-glaze layer because it fails the H requirement. This judgment made by the H-V criterion is supported by SEM observations. In the SE SEM image (Figure 5-6(f)), the shiny spot area has similar gray level to that of glaze layer, meaning its morphology is relatively flat (and thus has high V value in OM image). However, its BSE SEM image is much brighter comparing to that of glaze layer area, indicating the elements in the shiny spot are heavier, and thus contains a reduced oxygen component. This observation is further confirmed by point EDX analysis (20keV, 20mA). Three locations were examined, one in the glaze layer, one in the shiny spot, and one in the reference area outside of wear scar. The average weight percentage of major elements and their standard deviations are summarized in Table 5-1 Point EDX analysis on major element in glaze layer, shiny spot and reference area, all results are in wt%. Comparing to the glaze layer area, the oxygen detected in the shiny spot area is one magnitude smaller.

The chemical composition in shiny spot area is very close to the reference area where a static oxide layer was formed. Moreover, the color of the shiny spot in the OM image is also similar to that of the unworn area. In fact, such high brightness shiny spot has been observed at other temperature. The specific color of the shiny spot in the OM images varies at different testing temperature, either similar to the reference area or to the color of stainless steel that was tempered at slightly lower temperature. It is then hypothesized that the shiny spot area may be a thin static oxide layer formed at freshly exposed surface near the end of the test or during the cooling period right after the test finished. The flatness of this area may be caused by surface rubbing as implied by the observed wear trace along reciprocating sliding direction on top of it. Therefore, the shiny spot should be excluded from the glaze layer category.

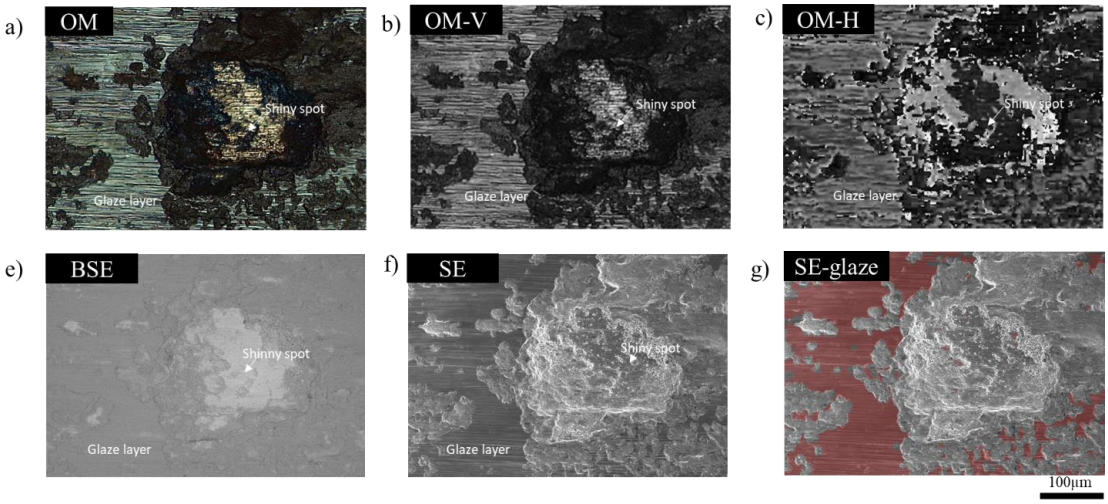

Figure 5-6 Demonstration of identifying glaze layer with OM image with reference of SEM, OM is pre-aligned to SE SEM: a) OM image; b) Value channel of OM; c) Hue channel of OM; d) BSE SEM image; f) SE SEM image; g) SE SEM overlaid with glaze layer mask(shadowed in red) identified from OM. All images share the same scale bar.

Table 5-1 Point EDX analysis on major element in glaze layer, shiny spot and reference area, all results are in wt%.

Major Elements	Glaze layer	Shinny spot	Reference
O	22.2 ± 3.0	1.4 ± 0.3	2.0 ± 1.0
Cr	20.4 ± 1.0	26.7 ± 0.2	25.5 ± 0.2
Fe	41.4 ± 1.7	52.1 ± 0.3	50.0 ± 2.1
Ni	14.6 ± 0.3	18.7 ± 0.3	18.2 ± 0.7

To summarize, the comparison of independent identifications of the glaze layer between OM and SEM images suggests that the H-V criterion works well, and neither of its two requirements, H-requirement or V requirement, is redundant.

It is worth noting that the specific number for brightness and color of an OM image can be greatly influenced by light intensity and OM camera setting, especially the white balance setting. In this study, all lighting and camera settings were fixed. Calibration will be needed to compare results taken by different optical microscopes and cameras. Figure 5-7 shows the three parameters used to analyze the OM images of samples tested at different temperatures. The reference color and brightness at each H and V value are provided along the side axes. Interestingly, the H value of the glaze layer area always ranges from about 60°-180°, which falls in the green spectrum, regardless of the testing temperature. Nevertheless, the average H value for glaze layer area is very stable (around 106°) across all testing temperatures. Similarly, V_{min} for all samples is about 0.33. The fact that the glaze layer hue always falls in a certain range of color may not be coincident. Considering the thin film interference theory, it may imply that glaze layer formed at the given testing

condition has a certain similar thickness or composition that is independent of temperature. These hypotheses need to be tested by a quantitative study on glaze layer thickness, and additional analysis on wear scars of other materials whose glaze layer have different chemical composition.

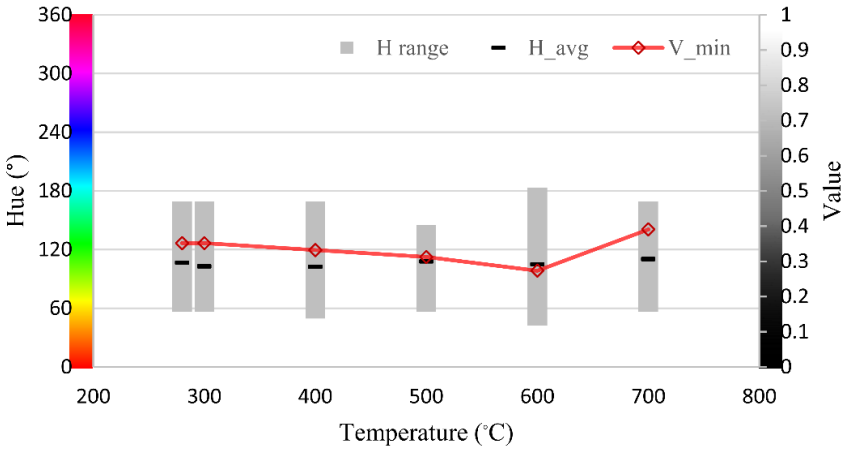

Figure 5-7 Hue range (Lower end =H_{min}, upper end = H_{max}) and V_{min} parameter used to identify glaze layer at each testing temperature, overlapped with average Hue value of glaze layer area(H_{avg})

5.5 Distribution of glaze layer and its temperature dependence

5.5.1 Height distribution of glaze layer at different temperature

Having completed the alignment of the height map, OM image and its glaze layer identification mask, every pixel in the height map is labeled as either "glaze layer" or "non-glaze layer". The height information of glaze layer and non-glaze layer can now be easily extracted and studied from a statistical prospective.

Figure 5-8 summarizes the typical height distribution of glaze layer and non-glaze layer at different stages both during the severe-to-mild wear transition and after transition in 50

bins histograms. The locations of the data subsets used in each histogram are identified by the white or black squares overlayed on corresponding OM images and height maps, respectively.

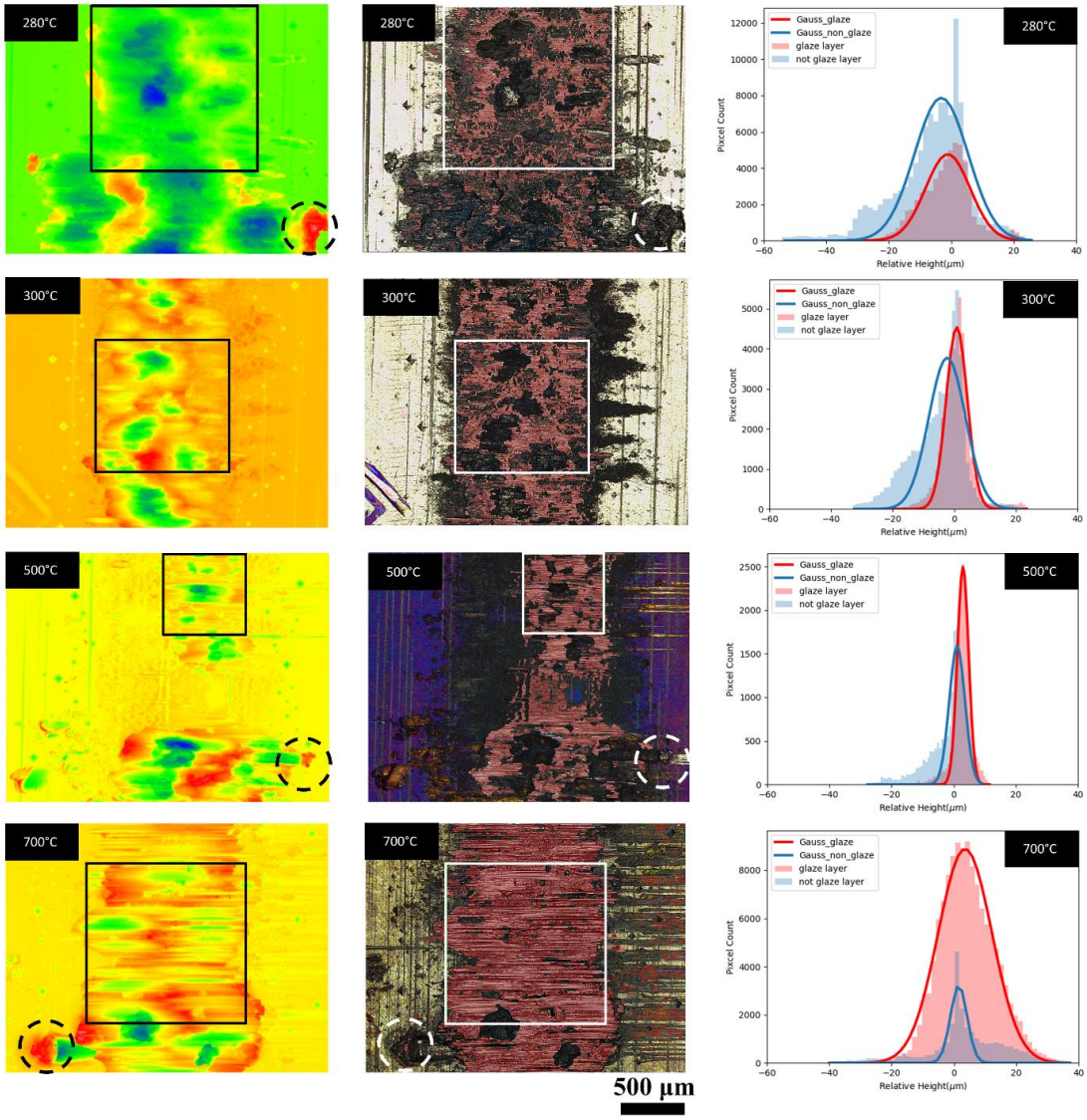

Figure 5-8 Histogram of height for glaze layer and non-glaze layer area and their fitted Gaussian distribution curve at 280°C, 300°C, 500°C and 700°C. The overlayed square in height map and OM represented the sampling location of the data subsets for each sample. Typical build-ups at the edge of wear scar are circled in dashed line. All OM images and height maps share the same scale bar.

The histograms are further quantified by conducting Gaussian distribution fitting using non-linear least squares regression

$$f(x) = A * exp(-\frac{(x-M)^2}{2\Sigma^2}) \quad (5\text{-}3)$$

Intuitively, the three fitting parameters A, M and Σ control the peak height, symmetric center, and the width of the Gaussian distribution curve. The fitted curves are shown in bold in Figure 5-8. The mean (μ) height for glaze layer and non-glaze layer for each data subsets are given in Table 5-2. For all temperatures, the average height of glaze layer is always higher than that of the non-glaze layer. From 280°C to 500°C, the height difference of the glaze layer is more significant with increasing of temperature. The increasing of area under the Gaussian fitted curve implies that the glaze layer coverage also increases with temperature rise. With temperature increasing, the Gaussian curve for both glaze and non-glaze layers gets narrower. This result indicates that the wear scar is shallower with less height variation as the result of glaze layer protection, even though the total net volume does not vary much beyond 300°C when the severe-to-mild transition is finished. At the extreme temperatures (600°C and 700°C), however, a large variation in height for the glaze layer is observed, and it may be a result of severe plastic deformation and local welding at those temperature.

To determine if the height difference between the glaze and non-glaze layers is statistically significant, a one-tailed unequal variance t-test (Welch's t-test) was conducted. The hypotheses are:

H_0 : the mean height of glaze and non-glaze layer are the same.

H_1: the mean height of glaze layer is higher than that of non-glaze layer.

The unequal variance t-test results are summarized in Table 5-2. For all temperatures, the null hypothesis is rejected by the low p values, which suggests that the height difference between the glaze and non-glaze layers within wear scar is statistically significant with 99.9% or higher confidence.

Table 5-2 Mean value and hypothesis test results for height distribution of glaze and non-glaze layer at each temperature

Sample	μ_{glaze} (μm)	μ_{non_glaze} (μm)	t value	p value
280C_plate	-1.722	-6.530	-95.3395	<0.001
300C_plate	0.797	-5.203	-140.693	<0.001
400C_plate	4.749	-3.583	-188.358	<0.001
500C_plate	3.015	-1.698	-109.091	<0.001
600C_plate	-1.753	-2.252	-6.48722	<0.001
700C_plate	4.483	3.400	-13.3717	<0.001

Considering the maximum and minimal height within each wear scar, we noticed that the overall minimal height location (i.e., valley) is always occupied by a non-glaze layer. The overall highest location, on the other hand, may still contain other features that are not associated with the glaze layer. For example, the maximum height for 280°C plate, circled in the OM and height maps in Figure 5-8, occurs at the edge of the wear scar resulting from plastic deformation. But locally the glaze layer will always cover the local high locations particularly if the sampling zone is well within the wear scar. The observation that the glaze

layer always occupies higher locations within wear scar is probably a result from its tribo-sintering formation mechanism [109–111]. Sintering depends on sufficient temperature and pressure. Wear debris located at a relatively high position has a better chance to be in contact and hence bearing load which drives the sintering process. At the same time, being at a relatively high location may also result in a reduction of the real contact area, which is beneficial for friction and wear reduction for hard bodies like metals. At temperatures above 500°C, while glaze layer formation occurs rapidly upon contact, the severe plastic deformation can lead to larger variation in relative height, which leads to the spreading of glaze layer at all height levels of wear scar.

5.5.2 Temperature dependence on the coverage of glaze layer

The projected glaze layer coverage C_p is given by [102]:

$$C_p = \frac{Area\ covered\ by\ glaze\ layer}{Total\ projected\ area\ of\ wear\ scar} \tag{5-4}$$

Since all images are aligned to the height map that has a constant magnification and identical pixel resolution, Eq. (5-4) is equivalent to

$$C_p = \frac{n_{glaze}}{n_{tot}} = \frac{n_{glaze}}{n_{glaze} + n_{non-glaze}} \tag{5-5}$$

where n_{tot} is the total number of pixels in a selected wear scar area that covers wear scar region; n_{glaze} and $n_{non-glaze}$ are the number of pixels labeled as glaze layer or non-glaze layer in the selected area. The glaze layer coverage for both pin and plate from 250°C to 700°C are shown in Figure 5-9. In general, C_p for the pin and plate at each temperature are

very similar to each other, and follow the same trend with increasing temperature. This similarity was expected for like bodies due to the identical chemical and mechanical properties. Although severe-to-mild wear transition appeared as low as 200°C for the number of cycles applied, a glaze layer was not clearly identified until the temperature reaches 250°C. The projected glaze layer coverage at 250°C for both the pin and plate is less than 5%. It is likely that the reduction in wear at 250°C is mostly attributed to the compacted debris bed that is not fully sintered to have the characteristics of a completely formed glaze layer [19,112]. Towards the temperature where severe-to-mild wear transition is observed by the material response, the projected glaze layer coverage is about 36%. This observation is consistent with others who reported <50% projected coverage is needed to achieve a complete severe-to-mild wear transition [102]. The projected coverage of the glaze layer continuously increases with further temperature rise, and reaches about 75% at the 700°C, the highest test temperature considered in this work.

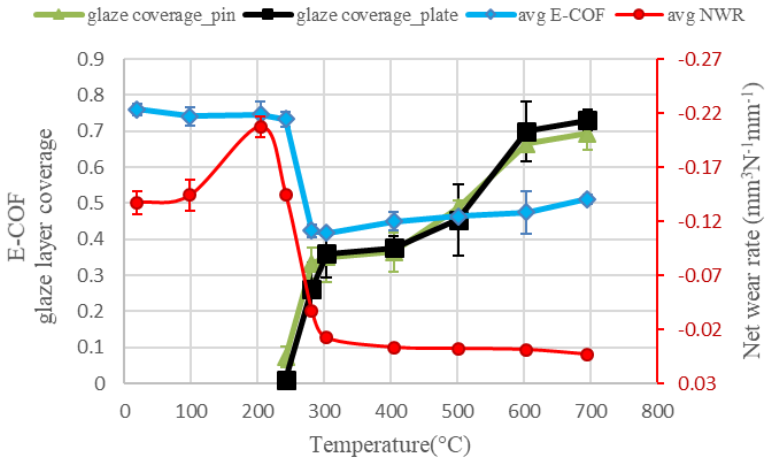

Figure 5-9 Effect of temperature on net wear rate wear, average $\bar{\mu}_E$ and glaze layer coverage on pin and plate.

Based on the rate change of C_p with respect to the temperature (denoted as $\overline{C_p}$) , the evolution of glaze layer coverage with increasing temperature for the material and test conditions considered can be divided into three stages:

Stage 1 (T≤300°C): $\overline{C_p}$ is constant. In other words, C_p increases linearly with temperature increase;

Stage 2 (300°C <T≤600°C): $\overline{C_p}$ increases with rising temperature;

Stage 3 (T>600°C): the increasing of $\overline{C_p}$ with temperature slows down comparing to Stage 2.

It is interesting to observe that the three stages of glaze layer coverage evolution with temperature is overlays well with the severe-to-mild transition of friction and wear for the material couple as shown in Figure 5-9. This observation provides strong evidence that the severe-to-mild wear transition is induced by the development of glaze layer. It worth emphasizing that the glaze layer coverage determined here is the coverage by 2D projection of the whole wear scar (projected coverage, C_p), not the coverage with respect to the real contact area (real coverage, C_r). The calculation of C_r is similar to Eq.5-4 except the denominator should be replaced by the total area that is in contact. Since the height variation within wear scar is one magnitude smaller than the width of wear scar, we ignore the curvature-induced difference between projection area and real contact area. Therefore, the equation for C_r can be approximated by:

$$C_r = \frac{n_{glaze\_c}}{n_{glaze\_c} + n_{non-glaze\_c}} \tag{5-6}$$

where n_{glaze_c} and $n_{non\_glaze\_c}$ represent the number of glaze layer and non-glaze layer pixels that are in contact, respectively. From the previous discussion we have already identified that the glaze layer is associated with the relatively high locations within the wear scar. At the same time, the tribo-sintering mechanism of the glaze layer formation also requires that the two bodies are in contact in the glaze layer region, at least at the moment of formation. Thus, it can be assumed that most glaze layers are in contact, i.e., $n_{glaze\_c} \approx n_{glaze}$. Non-glaze layer portions, in contrast, will have less possibility to be in contact due to its relatively low height. The portion of non-glaze layer area that is lower than its nearby glaze layer, especially those that are in the small valleys, may not be in contact during the fretting sliding process, which makes $n_{non-glaze\_c} < n_{non-glaze}$. As a result, C_r is expected to be higher than C_p for the same wear scar due to its smaller denominator. This explains why the minimum percent of glaze layer coverage upon severe-to-mild wear transition finishing can be less than 50% in many reported works [54,102], including in this work (36%), since all reported work are using C_p. The real coverage $C_r$is expected to be a higher value that is sufficient to alter the overall mechanical properties of the contact surfaces.

On the other hand, the rate difference of glaze layer coverage in the three stages may imply a mechanism change of glaze layer formation and/or its retention. It is believed that glaze layer is formed by a tribo-sintering of wear debris [27,36,109], and removal of wear debris from the interface will result in failure in glaze layer formation [113]. According to Figure

5-3(b), the μ_E quickly dropped at 700°C within the first 2000 cycles, which indicates that a sufficient amount of glaze layer has formed at a very early stage of the wear process at this temperature. The protection from the initially formed glaze layer can reduce the supply of fresh wear debris, which may explain the reduction of $\overline{C_p}$ beyond 600°C.

5.6 Evaluation of wear characterization tools for glaze layer identification

Having done a deep dive on tools for glaze layer characterization and gained experience on the characteristics of the glaze layer that can be captured by each tool, an overview of the benefits and disadvantages of the various tools can be given to provide a deeper thinking on what makes a good criterion for glaze layer identification.

To better compare the tools used in this and the work of others, it is necessary to set a standard for judging different criteria. Clearly, a good set of criteria should be sufficient to robustly distinguish a glaze layer from a non-glaze layer. High accuracy of glaze layer identification requires that both type I error (mis-identify glaze layer as non-glaze layer; i.e., false negative) and type II errors (mis-identify non-glaze as glaze layer; i.e., false positive) to be low. In addition to accuracy, the choice of the characterization tools can be further optimized to accommodate cost, convenience, availability and redundancy. Determination of the glaze layer identification criteria requires deep understanding of not only glaze layer, but also the characteristics of the non-glaze layer portion of the wear scar.

In the current work, the major source for type I error comes from the wear trace on top of the glaze layer, and it is well controlled by adding the ring light and applying opening/closing operation in image processing. Type II error is more challenging to handle,

since some non-glaze layer features share similar characteristics to the glaze layer. Four primary non-glaze layer features have been identified as possible sources of a type II error:

Unworn: This feature describes the reference area that is outside of the wear scar. While it does not participate in the contact and rubbing between the two bodies, it does experience static oxidation process during the test, and will be covered by a thin and uniform oxide layer. Unworn surfaces tend to have a smooth surface morphology and its height is usually set as reference (zero height plane) to normalize height in the profilometer characterization.

Build-up: This wear feature is found at or outside of wear scar edges that is usually highly oxidized and consists of the highest spots of the entire wear region. This feature may result from plastic deformation of the two bodies during reciprocating, expelled large wear particles, or spot welded wear debris at extreme temperatures. This feature usually has an irregular shape and morphology, but may appear dark in SE SEM images either due to charging effect or if it was once in contact with and flattened by the other body. Examples of build-ups are circled in the OM and height maps in Figure 5-8.

Embryonic glaze: This feature consists of condensed yet not fully sintered oxide or oxidized debris, and can be found near the glaze layer region or before the formation of the glaze layer. In an OM image with coaxial illumination lighting mode, this region has a similar hue as a glaze layer, but its morphology is usually rougher than that of a glaze layer due to incomplete sintering.

Shiny spot: This feature refers to a highly reflective region that is mostly found in valleys of the wear scar. It may be a freshly exposed surface near the end of the test and may also have a statically-formed oxide layer.

Table 5-3 summarizes the major tools and techniques that have been used or could be used to characterize the glaze layer, each of which targets one or more aspect of glaze layer's characteristics. The representation of glaze layer and the four non-glaze layer features are listed under each target characteristics. Possible type II error sources are shaded where the non-glaze layer features identified in each column has similar characteristics to the glaze layer under the same characterization technique. As indicated in this chart, there is always one or more type II error sources if only considering a single feature of glaze layer. Thus, it is essential that any criterion should depend on two or more characteristics to achieve sufficient and robust glaze layer identification. The H-V criterion proposed in this work is an effective one because it involves a single, widely available characterization tool, OM, with no redundancy. With help of Table 5-3, additional glaze layer identification criteria can be conceived by mixing and matching characterization techniques based on tool availability and fusing the characterization results with the developed image alignment pipeline.

Table 5-3 Summary of existing tools that could be used to characterize glaze layer, and the outcome of glaze layer and non-glaze layer feature under those characterization. Possible type II error source(s) for each tool column are highlighted.

Tool candidate(s)	Feature measured	Outcome				
		Glaze layer	Non-glaze layer			
			Unworn	Build-up	Embryonic glaze	Shiny spot
BSE, EDX	O wt%	high	low	low-mid	high	mid
SE, Profilometer	Surface morphology	smooth	smooth	rough or smooth	rough	smooth
OM (with CXI lighting)	Reflectiveness -V value	high	high	low-mid	low	high at low Temp
OM (with CXI lighting)	Color -H value	green-blueish tint	various	various	green-blueish tint	various
Raman, XPS	Type of oxide	various	various	various	various	various
Profilometer	Relative height	local high	zero height plane	overall high	lower than neighbor glaze layer	low
Manual label	Location	within wear scar	outside of wear scar	at the edges of wear scars	within wear scar	within wear scar, mostly in valleys

Table 5-3 also illuminates that "type of oxide" and "relative height" are not suitable choices to make glaze layer identification criterion. Although the preferred oxide type for glaze layer formation has been widely studied [14,27,29,39,47,48], those studies were mostly conducted on the pre-identified glaze layer, instead of the other way around utilizing the

oxide type information for glaze layer identification. In fact, mapping the type of oxide at a sufficient pixel resolution at large scale can be challenging, especially in cases where multiple types of oxide co-exist in both the glaze layer and non-glaze layer regions (denoted as “various” in the table). Relative height, on the other hand, consist a distribution (as illustrated in Figure 5-8) for both glaze layer and non-glaze layer, and does not have a clear cut-off value to differentiate glaze layer and non-glaze layer. Thus, the relative height is not a suitable quantitative measure for glaze layer identification either.

5.7 Conclusions

In this work, we developed strategies that enable multi-spectrum study of wear scars. This methodology is applied to study the glaze layer formed on 310S stainless steel after like-on-like, cylinder-on-flat fretting tests at different temperatures, from 20°C to 700°C. The key findings and contributions are summarized as below:

1. Computer vision concepts have been introduced to the image analysis of worn surfaces, and a systematic workflow has been established and demonstrated for aligning images captured by various characterization tools with sub-pixel error. In this way the characterization results are integrated to cover multiple characteristics of wear features.
2. We proposed a new quantitative criterion, H-V criterion, for glaze layer identification based the HSV separation of OM images taken using the CXI lighting mode. This method can quickly identify the glaze layer parts of the wear scar in a satisfactorily accurate manner using optical microscopy. The parameters used in

the H-V criterion are very stable regardless of testing temperature, which may imply a constant thickness or composition of glaze layer.

3. Using the new tools, we studied the height distribution of glaze layer and non-glaze layer at various testing temperatures and revealed that the glaze layer always occupies relatively high locations within the wear scar. The height difference between the glaze layer and non-glaze layer is statistically significant. This phenomenon may be explained by the tribo-sintering mechanism theory for glaze layer formation. This result also suggests that the glaze layer may reduce friction and wear by reducing the real contact area.
4. The projected coverage of glaze layer on both the pin and plate follow the same increasing trend with temperature rise as the two bodies are the same material. The projected coverage of glaze layer is observed upon finishing severe-to-mild transition is 36%. Three distinct stages of this trend have been discovered and they are well aligned with the severe-to-mild transition of the wear behavior of the tested material system. This observation suggests that the development of glaze layer and its expanding coverage is the key reason for the severe-to-mild wear transition. Given that the glaze layer occupies a higher position within the wear scar, the coverage of the glaze layer with respect to the real contact area is expected to be higher than the projected coverage and high enough to alter the mechanical property of the contact interface.
5. Characterization tools that have been used for glaze layer identification and characterization have been compared and evaluated, which enables the conceiving

of more customized glaze layer identification criterion based on research goals and tool availability.

CHAPTER 6. GENERAL CONCLUSIONS AND RECOMMENDATIONS

In this research, complete methodologies and principles for generating an informative wear map are proposed and exercised. Experimentally, the number of tests can be reduced with a hierarchical probing design of experiments (DOE) that biases the sampling density to improve boundary resolution between different wear mechanisms on the wear map. Alternatively, the capability of using a recently developed N_{GL} model to predict the boundaries theoretically is demonstrated. The fitting result suggests that the temperature term involved in the N_{GL} model reflects the temperature at contact location instead of the environmental temperature away from the immediate wear interface. Combining experimental work as well as the theoretical, the N_{GL} model can help obtain a useful wear map in a cost effective manner and has great potential to be expended for industry use.

Through a systematic study of the influence of environmental temperature and frequency on the wear performance of 310S/310S cylinder-on-flat fretting system, direct experimental evidence for the coupling effect between temperature and frequency has been obtained, and is clearly reflected in the constructed wear map.

The newly proposed quantitative criteria, H-V criterion provides fast, robust and accurate solution for glaze layer identification. Parameters used in H-V criterion for the current material system are very stable regardless of testing temperature, which implies a constant composition or thickness of the glaze layer.

Additional characteristics of glaze layer can be revealed by aligning images generated from multiple characterization techniques with sub-pixel accuracy. The glaze layer has been found to always occupy the relatively high location in wear scar, and such location preference is statistically significant. This phenomenon may be explained by the tribo-sintering mechanism theory for glaze layer formation. This result also suggests that the glaze layer may reduce friction and wear by reducing the real contact area, in addition to its superior hardness and ductility.

The following are some recommendations to add value and extend the current research:

1. Additional fretting tests can be conducted to improve the boundary resolution of the current wear maps. Additional tests should be focused on the locations where a rapid change in curvature and gradient of the NWR contours.
2. Additional characterizations should be conducted on the worn surfaces of the post-test samples. Specifically, XRD and XPS analysis on glaze layer and wear debris characterization are desired to identify the type of oxide that construct the glaze layer. Additional SEM/EDX characterization is needed for cross-section observation of the wear samples, and the thickness variation of glaze layer as a function of environmental temperature, frequency, and its influence to NWR needs to be addressed. The thickness information is also important to improve understanding of the H-V criterion.
3. The samples that went through temperature-frequency coupling effect should be characterized to find more evidence to support or decline current hypothesis explaining the coupling effect. More specifically, the possible influence of debris' motion by frequency needs to be addressed.

4. A better estimation of temperature rise at the contact interface is needed to be merged in the N_{GL} model.
5. The glaze layer identification workflow should be applied to additional worn samples of 310S/310S at other frequencies beside 10Hz to generate a glaze layer coverage map. Comparing the glaze layer coverage map to the current wear map can further reveal the wear rate determination by glaze layer coverage.
6. The influence of load, sliding amplitude, chemical composition and their potential coupled effect with temperature and frequency in wear response and mechanisms should be investigated. Those results can also be used to generate a higher dimensional wear map, and further calibrate the N_{GL} model for other wear couples targeting high temperature wear applications.
7. The H-V criterion should be validated using observations of the glaze layer that is formed at interface of the other body to further explore the chemical composition effect of glaze layer in its color determination.
8. To improve the image analysis of the pin, or other second body having a curved surface, additional mathematical formulations should be used to extend the current Homography transformation framework in the image alignment workflow.
9. The stability of the boundaries obtained in the current wear map should also be probed by a dynamic testing set-up that cyclically switch between conditions that leads to different wear mechanisms. Such an effort would be beneficial to correlate the wear map to the real application of the material that involves dynamic changes in working conditions.

REFERENCES

[1] J. Dobromirski, Variables of fretting process: are there 50 of them?, ASTM Spec. Tech. Publ. 1159 (1992) 60.

[2] P.H. Shipway, Fretting wear, in: ASM Handb., 2017. doi:10.4271/901786.

[3] R. Lewis, R.S. Dwyer-Joyce, Wear of diesel engine inlet valves and seat inserts, Proc. Inst. Mech. Eng. Part D J. Automob. Eng. 216 (2002) 205–216. doi:10.1243/0954407021529048.

[4] E. Summerville, K. Venkatesan, C. Subramanian, Wear processes in hot forging press tools, Mater. Des. 16 (1995) 289–294.

[5] R. Lewis, R.S. Dwyer-Joyce, Automotive engine valve recession, Professional Engineering, 2002.

[6] D.P. Nolan, Fire fighting pumping systems at industrial facilities, William Andrew, 2011.

[7] ASTM, Standard Guide for Fretting Fatigue Testing, E2789 - 10. 10 (2015) 1–10. doi:10.1520/E2789.

[8] J.F. Archard, W. Hirst, The wear of metals under unlubricated conditions, Proc. R. Soc. London. Ser. A. Math. Phys. Sci. 236 (1956) 397–410.

[9] E. Rabinowicz, R.I. Tanner, Friction and wear of materials, J. Appl. Mech. 33 (1966) 479.

[10] I. Hutchings, P. Shipway, Tribology: friction and wear of engineering materials, Butterworth-Heinemann, 2017.

[11] D.H. Buckley, Surface effects in adhesion, friction, wear, and lubrication, Elsevier, 1981.

[12] R.B. Waterhouse, The role of adhesion and delamination in the fretting wear of metallic materials, Wear. 45 (1977) 355–364.

[13] N.P. Suh, The delamination theory of wear, Wear. 25 (1973) 111–124.

[14] T.F.J.J. Quinn, Review of oxidational wear: Part I: The origins of oxidational wear, Tribol. Int. 16 (1983) 257–271. doi:10.1016/0301-679X(83)90086-5.

[15] H. Kato, A. Takimi, M. Umemoto, Tribofilms Produced by Supply of Fine Metal Particles in Vacuum, Tribol. Online. 6 (2011) 50–54. doi:10.2474/trol.6.50.

[16] K. Kato, Classification of wear mechanisms / models, in: G.W. (Gwidon W.. Stachowiak (Ed.), Wear-Materials, Mech. Pract. John Wiley Sons, Ltd, West Sussex, John Wiley & Sons, 2005: pp. 9–20.

[17] P. Blanchard, C. Colombie, V. Pellerin, S. Fayeulle, L. Vincent, Material effects in fretting wear: application to iron, titanium, and aluminum alloys, Metall. Trans. A. 22 (1991) 1535–1544.

[18] D.A. Rigney, Transfer, mixing and associated chemical and mechanical processes during the sliding of ductile materials, Wear. 245 (2000) 1–9.

[19] M. Godet, The third-body approach: A mechanical view of wear, Wear. 100 (1984)

437–452. doi:10.1016/0043-1648(84)90025-5.

[20] J. Jiang, F.H. Stott, M.M. Stack, The role of triboparticulates in dry sliding wear, Tribol. Int. 31 (1998) 245–256.

[21] D.S. Lin, F.H. Stott, G.C. Wood, The effects of elevated ambient temperatures on the friction and wear behavior of some commercial nickel base alloys, ASLE Trans. 17 (1974) 251–262. doi:10.1080/05698197408981463.

[22] F.H. Stott, G.C. Wood, The influence of oxides on the friction and wear of alloys, Tribol. Int. 11 (1978) 211–218. doi:10.1016/0301-679X(78)90178-0.

[23] F.H. Stott, J. Glascott, G.. . Wood, The sliding wear of commercial Fe–12%Cr alloys at high temperature, Wear. 101 (1985) 311–324.

[24] F.H. Stott, D.S. Lin, G.C. Wood, The structure and mechanism of formation of the ‘glaze’oxide layers produced on nickel-based alloys during wear at high temperatures, Corros. Sci. 13 (1973) 449–469.

[25] C. Rynio, H. Hattendorf, J. Klöwer, G. Eggeler, The evolution of tribolayers during high temperature sliding wear, Wear. 315 (2014) 1–10. doi:10.1016/j.wear.2014.03.007.

[26] A. Viat, G. Guillonneau, S. Fouvry, G. Kermouche, S. Sao Joao, J. Wehrs, J. Michler, J.F. Henne, Brittle to ductile transition of tribomaterial in relation to wear response at high temperatures, Wear. 392–393 (2017) 60–68. doi:10.1016/j.wear.2017.09.015.

[27] H. Kato, K. Komai, Tribofilm formation and mild wear by tribo-sintering of nanometer-sized oxide particles on rubbing steel surfaces, Wear. 262 (2007) 36–41.

[28] F.H. Stott, High-temperature sliding wear of metals, Tribol. Int. 35 (2002) 489–495. doi:10.1016/S0301-679X(02)00041-5.

[29] T. Kayaba, A. Iwabuchi, The fretting wear of 0.45% C steel and austenitic stainless steel from 20 to 650 °C in air, Wear. 74 (1981) 229–245. doi:10.1016/0043-1648(81)90165-4.

[30] S.R. Pearson, P.H. Shipway, J.O. Abere, R.A.A. Hewitt, The effect of temperature on wear and friction of a high strength steel in fretting, Wear. 303 (2013) 622–631. doi:10.1016/j.wear.2013.03.048.

[31] R. Rybiak, S. Fouvry, B. Bonnet, Fretting wear of stainless steels under variable temperature conditions: introduction of a ‘composite’wear law, Wear. 268 (2010) 413–423.

[32] I.A. Inman, P.S. Datta, Development of a simple ‘ temperature versus sliding speed ’ wear map for the sliding wear behaviour of dissimilar metallic interfaces II, Wear. 265 (2008) 1592–1605. doi:10.1016/j.wear.2008.03.009.

[33] I.A. Inman, S.R. Rose, P.K. Datta, Development of a simple ‘ temperature versus sliding speed ’ wear map for the sliding wear behaviour of dissimilar metallic interfaces, Wear. 260 (2006) 919–932. doi:10.1016/j.wear.2005.06.008.

[34] A. Viat, M.I. De Barros Bouchet, B. Vacher, T. Le Mogne, S. Fouvry, J.F. Henne,

Nanocrystalline glaze layer in ceramic-metallic interface under fretting wear, Surf. Coatings Technol. 308 (2016) 307–315. doi:10.1016/j.surfcoat.2016.07.100.

[35] X. Jin, P.H. Shipway, W. Sun, The Role of Temperature and Frequency on Fretting Wear of a Like-on-Like Stainless Steel Contact, Tribol. Lett. (2017). doi:10.1007/s11249-017-0858-0.

[36] A. Dréano, S. Fouvry, G. Guillonneau, A tribo-oxidation abrasive wear model to quantify the wear rate of a cobalt-based alloy subjected to fretting in low-to-medium temperature conditions, Tribol. Int. 125 (2018) 128–140. doi:10.1016/j.triboint.2018.04.032.

[37] S.R. Pearson, P.H. Shipway, Is the wear coefficient dependent upon slip amplitude in fretting ? Vingsbo and Söderberg revisited, Wear. 331 (2015) 93–102. doi:10.1016/j.wear.2014.11.005.

[38] D.E. Taylor, F.B. Hardisty, R.B. Waterhouse, A.Y. Nehru, The fretting wear of an austenitic stainless steel in air and in carbon dioxide at elevated temperatures, Wear. 56 (1979) 9–18. doi:10.1016/0043-1648(79)90003-6.

[39] A. Viat, A. Dréano, S. Fouvry, M.I. De Barros Bouchet, J.F. Henne, Fretting wear of pure cobalt chromium and nickel to identify the distinct roles of HS25 alloying elements in high temperature glaze layer formation, Wear. 376–377 (2017) 1043–1054. doi:10.1016/j.wear.2017.01.049.

[40] I. García, A. Ramil, J.P. Celis, A mild oxidation model valid for discontinuous contacts in sliding wear tests: Role of contact frequency, Wear. 254 (2003) 429–

440. doi:10.1016/S0043-1648(03)00262-X.

[41] J. Jiang, F.H. Stott, M.M. Stack, A mathematical model for sliding wear of metals at elevated temperatures, Wear. 181–183 (1995) 20–31. doi:10.1016/0043-1648(95)90004-7.

[42] T.F.J. Quinn, wear modelling : I, Wear. 153 (1992) 179–200.

[43] T.F.J. Quinn, Review of oxidational wear Part II: Recent developments and future trends in oxidational wear research, Tribol. Int. 16 (1983) 305–315. doi:10.1016/0301-679X(83)90039-7.

[44] J. Mølgaard, V.K. Srivastava, The activation energy of oxidation in wear, Wear. 41 (1977) 263–270. doi:10.1016/0043-1648(77)90006-0.

[45] S.R. Rose, Studies of the high temperature tribological behaviour of some superalloys, University of Northumbria at Newcastle, 2000. http://nrl.northumbria.ac.uk/id/eprint/15707.

[46] S. Soemantri, A.C. McGee, I. Finnie, Some aspects of abrasive wear at elevated temperatures, Wear. 104 (1985) 77–91.

[47] P.L. Hurricks, The fretting wear of mild steel from 200° to 500°C, Wear. 30 (1974) 189–212.

[48] P.L. Hurricks, The fretting wear of mild steel from room temperature to 200°C, Wear. 19 (1972) 207–229. doi:10.1016/0043-1648(72)90304-3.

[49] J.F. Archard, The temperature of rubbing surfaces, Wear. 2 (1959) 438–455.

[50] W.T. Clark, C. Pritchard, J.W. Midgley, Paper 12: mild wear of unlubricated hard steels in air and carbon dioxide, in: Proc. Inst. Mech. Eng. Conf. Proc., SAGE Publications Sage UK: London, E*NGL*and, 1967: pp. 97–106.

[51] R.T. Foley, M.B. Peterson, C. Zapf, Frictional characteristics of cobalt, nickel, and iron as influenced by their surface oxide films, ASLE Trans. 6 (1963) 29–39.

[52] A. Iwabuchi, The role of oxide particles in the fretting wear of mild steel, Wear. 151 (1991) 301–311. doi:10.1016/0043-1648(91)90257-U.

[53] S.Q. Wang, M.X. Wei, Y.T. Zhao, Effects of the tribo-oxide and matrix on dry sliding wear characteristics and mechanisms of a cast steel, Wear. 269 (2010) 424–434.

[54] A. Dréano, S. Fouvry, G. Guillonneau, A combined friction energy and tribo-oxidation formulation to describe the high temperature fretting wear response of a cobalt-based alloy, Wear. 426–427 (2019) 712–724. doi:10.1016/j.wear.2019.01.023.

[55] S. Fouvry, P. Kapsa, L. Vincent, Quantification of fretting damage, Wear. 200 (1996) 186–205. doi:10.1016/S0043-1648(96)07306-1.

[56] S. Fouvry, P. Duó, P. Perruchaut, A quantitative approach of Ti-6Al-4V fretting damage: Friction, wear and crack nucleation, Wear. 257 (2004) 916–929. doi:10.1016/j.wear.2004.05.011.

[57] X. Jin, P.H.H. Shipway, W. Sun, The role of frictional power dissipation (as a

function of frequency) and test temperature on contact temperature and the subsequent wear behaviour in a stainless steel contact in fretting, Wear. 330–331 (2015) 103–111. doi:10.1016/j.wear.2015.02.022.

[58] H.H. Uhlig, Mechanism of fretting corrosion, J. Appl. Mech. ASME. 21 (1954) 401–407.

[59] I.-M. Feng, H.H. Uhlig, Fretting corrosion of mild steel in air and in nitrogen, J. Appl. Mech. 21 (1954) 395–400.

[60] A.R. Warmuth, P.H. Shipway, W. Sun, Fretting wear mapping: The influence of contact geometry and frequency on debris formation and ejection for a steel-on-steel pair, Proc. R. Soc. A Math. Phys. Eng. Sci. 471 (2015). doi:10.1098/rspa.2014.0291.

[61] H. Blok, The dissipation of frictional heat, Appl. Sci. Res. Sect. A. 5 (1955) 151–181.

[62] M.P. Szolwinski, G. Harish, T.N. Farris, T. Sakagami, In-situ measurement of near-surface fretting contact temperatures in an aluminum alloy, (1999).

[63] D.G. Bansal, J.L. Streator, A method for obtaining the temperature distribution at the interface of sliding bodies, Wear. 266 (2009) 721–732. doi:10.1016/j.wear.2008.08.019.

[64] J.C. Jaeger, Moving sources of heat and the temperature of sliding contacts, in: Proc. R. Soc. New South Wales, 1942: pp. 203–224.

[65] X. Tian, F.E. Kennedy Jr, Maximum and average flash temperatures in sliding

contacts, (1994).

[66] M.F. Ashby, J. Abulawi, H.S. Kong, Temperature maps for frictional heating in dry sliding, Tribol. Trans. 34 (1991) 577–587.

[67] H.S. Carslaw, J.C. Jaeger, Conduction of heat in solids, Clarendon press, 1992.

[68] X. Jin, Investigation of the interrelated effects of temperature and frequency on fretting wear, (2017).

[69] T.H.C. Childs, The sliding wear mechanisms of metals, mainly steels, Tribol. Int. 13 (1980) 285–293. doi:10.1016/0301-679X(80)90092-4.

[70] H. Kato, T.S. Eyre, B. Ralph, Wear mechanism map of nitrided steel, Acta Met. Mater. 42 (1994) 1703–1713.

[71] L. Rapoport, The competing, Wear. 183 (1995) 280–289.

[72] S.C. Lim, M.F. Ashby, Wear-mechanism Maps, Acta Metall. 35 (1987) 1–24.

[73] S. Hernandez, J. Hardell, C. Courbon, H. Winkelmann, B. Prakash, S. Hernandez, J. Hardell, C. Courbon, H. Winkelmann, B. Prakash, High temperature friction and wear mechanism map for tool steel and boron steel tribopair, Tribol. - Mater. Surfaces Interfaces. 5831 (2014). doi:10.1179/1751584X13Y.0000000049.

[74] S.C. Lim, M.F. Ashby, J.H. Brunton, Wear-rate transitions and their relationship to wear mechanisms, Acta Metall. 35 (1987) 1343–1348. doi:10.1016/0001-6160(87)90016-2.

[75] C. Rynio, H. Hattendorf, J. Klöwer, G. Eggeler, On the physical nature of tribolayers and wear debris after sliding wear in a superalloy/steel tribosystem at 25 and 300°C, Wear. 317 (2014) 26–38. doi:10.1016/j.wear.2014.04.022.

[76] T.G. Río, A. Rico, M.A. Garrido, P. Poza, J. Rodríguez, Temperature and velocity transitions in dry sliding wear of Al – Li / SiC composites, Wear. 268 (2010) 700–707. doi:10.1016/j.wear.2009.11.006.

[77] G. Rasool, M.M. Stack, Tribo-oxidation maps for Ti against steel, Tribol. Int. 91 (2014) 258–266. doi:10.1016/j.triboint.2015.03.014.

[78] J.R. (Joseph R.. Davis, ASM International. Handbook Committee., Stainless steels, ASM International, 1994.

[79] J. Beddoes, J.G. Parr, Introduction to stainless steels, 3rd Edn, 3rd ed., Materials Park, OH (United States); ASM International, 1999.

[80] M.F. McGuire, Stainless steels for design engineers, Asm International, 2008.

[81] R.A. Lula, A.J. Lena, H.M. Johnson, Effect of Cold Work on Elevated-Temperature Properties of Types 301, 305, and 310 Stainless Steels, TRANS. ASME. 79 (1957) 921–926.

[82] T. Tanaka, K. Ito, K. Hoshino, Effect of Alloying Elements, Cold-Rolling Reduction and Deformation-Induced Martensite on Mechanical Properties of Low Carbon Type 301 Hard Stainless Steel.(Development of Low Carbon High Strength Stainless Steels-Ii), Trans. Iron Steel Inst. Japan. 23 (1982) 140.

[83] Z.Y. Yang, M.G.S. Naylor, D.A. Rigney, Sliding wear of 304 and 310 stainless steels, Wear. 105 (1985) 73–86. doi:10.1016/0043-1648(85)90007-9.

[84] R. Yin, Cyclic and isothermal exposures of 310SS to 10% CH4/H2 carburizing gas mixture at high temperatures, Mater. Sci. Eng. A. 391 (2005) 19–28.

[85] R.S. Millman, A. Sleightholme, A.A. Parry, Sliding fretting wear of mild steel fins on stainless steel flats in CO2 atmospheres, Wear. 106 (1985) 77–95. doi:10.1016/0043-1648(85)90105-X.

[86] X. Jin, W. Sun, P.H. Shipway, The role of geometry changes and debris formation associated with wear on the temperature field in fretting contacts, Tribol. Int. 102 (n.d.) 392–406. http://eprints.nottingham.ac.uk/34140/1/The role of geometry changes (accessed June 18, 2018).

[87] A. Iwabuchi, K. Hori, H. Kudo, The Effects of Temperature, Pre-Oxidation and Pre-Sliding on the Transition From Severe Wear to Mild Wear for S 45 C Carbon Steel and SUS 304 Stainless Steel, in: K.C. Ludema (Ed.), Wear Mater. Int. Conf. Wear Mater., ASME, Huston, Texas, USA, 1987: pp. 211–218.

[88] R. Chen, A. Iwabuchi, T. Shimizu, Effects of ambient pressure on fretting friction and wear behavior between SUS 304 steels, Wear. 249 (2001) 379–388. doi:10.1016/S0043-1648(01)00547-6.

[89] J.R. Frederick, a Study of the Elastic Properties of Various Solids by Means of Ultrasonic Pulse Techniques., (1948).

[90] E. Garofalo, P.R. Malenock, G. V Smith, The influence of temperature on the elastic constants of some commercial steels, Determ. Elastic Constants, Spec. Tech. Publ. Am. Soc. Test. Mater. (1952) 10.

[91] F. Garofalo, Temperature dependence of the elastic moduli of several stainless steels, in: Proc. ASTM, 1960: pp. 738–749.

[92] T. international N.C. Inc, Austenitic chromium-nickel stainless steels-engineering properties at elevated temperatures, 1963.

[93] ASTM E8, ASTM E8/E8M standard test methods for tension testing of metallic materials 1, Annu. B. ASTM Stand. 4. (2010) 1–27. doi:10.1520/E0008.

[94] K.L. Johnson, K.L. Johnson, Contact mechanics, Cambridge university press, 1987.

[95] X. Jin, W. Sun, P.H.H. Shipway, Derivation of a wear scar geometry-independent coefficient of friction from fretting loops exhibiting non-Coulomb frictional behaviour, Tribol. Int. 102 (2016) 561–568. doi:10.1016/j.triboint.2016.06.012.

[96] M. Hirsch, Temperature Dependent Fretting Damage Modeling of AISI 301 Stainless Steel, Goergia Institute of Technology, 2016. doi:10.13140/RG.2.1.3131.0883.

[97] M.R. Hirsch, R.W. Neu, A simple model for friction evolution infretting, Wear. 301 (2013) 517–523. doi:10.1016/j.wear.2013.01.036.

[98] A.Dreano, Formalisation of the tribo-oxidation mechanisms of a cobalt-based alloy subjected to fretting wear : influence of the temperature, Université de Lyon, 2019.

[99] B. Van Peteghem, S. Fouvry, J. Petit, Effect of variable normal force and frequency on fretting wear response of Ti-6Al-4V contact, Wear. 271 (2011) 1535–1542. doi:10.1016/j.wear.2011.01.060.

[100] R. Cottis, Shreir's corrosion, Elsevier Amsterdam, The Netherlands:, 2010.

[101] H. Hong, R.F. Hochman, T.F.J. Quinn, A New Approach to The Oxidational Theory of Mild Wear, Tribol. Trans. 31 (1988) 71–75. doi:10.1080/10402008808981800.

[102] J. Jiang, F.H. Stott, M.M. Stack, Characterization of wear scar surfaces using combined three-dimensional topographic analysis and contact resistance measurements, Tribol. Int. 30 (1997) 517–526. doi:10.1016/S0301-679X(96)00074-6.

[103] A. Dreano, S. Fouvry, S. Sao Joao, J. Galipaud, G. Guillonneau, S. Sao-Joao, J. Galipaud, G. Guillonneau, The formation of a cobalt-based glaze layer at high temperature: A layered structure, Wear. 440–441 (2019) 203101. doi:10.1016/j.wear.2019.203101.

[104] W.M. Rainforth, A.J. Leonard, C. Perrin, A. Bedolla-Jacuinde, Y. Wang, H. Jones, Q. Luo, High resolution observations of friction-induced oxide and its interaction with the worn surface, Tribol. Int. 35 (2002) 731–748. doi:10.1016/S0301-679X(02)00040-3.

[105] R. Hartley, A. Zisserman, Multiple view geometry in computer vision, Cambridge university press, 2003.

[106] R. Szeliski, Computer vision: algorithms and applications, Springer Science & Business Media, 2010.

[107] D.J. Whitehouse, Handbook of surface metrology, CRC Press, 1994.

[108] N. Efford, Digital Image Processing: A Practical Introduction Using JavaTM. Pearson Education, Slate. (2000).

[109] K. Adachi, K. Kato, Formation of smooth wear surfaces on alumina ceramics by embedding and tribo-sintering of fine wear particles, Wear. 245 (2000) 84–91.

[110] A. Dreano, S. Fouvry, G. Guillonneau, Understanding and formalization of the fretting-wear behavior of a cobalt-based alloy at high temperature, Wear. 452–453 (2020) 203297. doi:10.1016/j.wear.2020.203297.

[111] C.H. Hager, J. Hu, C. Muratore, A.A. Voevodin, R. Grandhi, The mechanisms of gross slip fretting wear on nickel oxide/Ti6Al4V mated surfaces, Wear. 268 (2010) 1195–1204. doi:10.1016/j.wear.2009.11.004.

[112] L. Vincent, Y. Berthier, A. Floquet, M. Godet, Fretting: Load carrying capacity of wear debris, J. Tribol. 106 (1984) 192–200. doi:10.1115/1.3260881.

[113] E.R. Leheup, R.E. Pendlebury, Unlubricated reciprocating wear of stainless steel with an interfacial air flow, Wear. 142 (1991) 351–372. doi:10.1016/0043-1648(91)90174-S.